Surface and interface structure of electrochemically grafted ultra-thin organic films on metallic and semiconducting materials

vorgelegt von
MSc Phys.
Ecatherina (Katy) Roodenko
aus Tel-Aviv

von der Fakultät II - Mathematik und Naturwissenschaften
der Technischen Universität Berlin
zur Erlangung des akademischen Grades
Doktor der Naturwissenschaften
Dr. rer. nat.

genehmigte Dissertation

Promotionsausschuss:

Vorsitzender: Prof. Dr. E. Sedlmayr
Berichter: Prof. Dr. N. Esser
Berichter: Prof. Dr. C. Thomsen

Tag der wissenschaftlichen Aussprache: 14.12.2007

Berlin 2008

D 83

Parts of this work were already published in:

Gensch M., Roodenko K., Hinrichs K., Hunger R., Güell A. G., Merson A., Schade U., Shapira Y., Dittrich Th., Rappich J., Esser N. *"Molecule-solid interfaces studied with infrared ellipsometry: ultrathin nitrobenzene films.",* J. Vac. Sci. and Technol. **B 23** 1838 (2004).

Rappich J., Merson A., Roodenko K., Dittrich Th., Gensch M., Hinrichs K., Shapira Y. *"Electronic properties of Si surfaces and side reactions during electrochemical grafting of phenyl layers.",* J. Phys. Chem. **B 110** 1332 (2006).

Roodenko K., Gensch M., Heise H. M., Schade U., Esser N., Hinrichs K. *"Influences of thick film inhomogeneities on the ellipsometric parameters.",* Infrared Phys. and Technol. **49** 39 (2006).

Güell A. G., Roodenko K., Yang F., Hinrichs K., Gensch M., Sanz F., Rappich J. *"Interface properties and passivation of p-Si(111) surfaces by electrochemical organic layer deposition.",* Mater. Sci. and Eng. B **134** 273 (2006).

Roodenko K., Rappich J., Gensch M., Esser N., Hinrichs K., Hunger R. *"Time-resolved Synchrotron XPS monitoring of irradiation-induced nitrobenzene reduction for chemical lithography.",* J. Phys. Chem. B **111** 7541 (2007).

Roodenko K., Rappich J., Gensch M., Esser N., Hinrichs K. *"Studies of electrochemically grafted thin organic layers on inorganic surfaces with infrared spectroscopic ellipsometry.",* Appl. Phys. A **90** 175 (2008).

Contents

Chapter 1

Introduction

The aim of this work was to characterize the electrochemically deposited ultra–thin organic films on metallic and semiconducting surfaces. The understanding of the thin film composition, of the orientation of molecules in the organic layers and of the film/substrate interface structure is essential for optimizing the preparation conditions. Improvement of such hybrid organic/inorganic materials is important in many engineering applications, as for instance in photovoltaic and other optoelectronic technologies.

Electrochemistry is a non-vacuum technique and it does not require elevated temperatures for the deposition of organic molecules [1]. It is typically carried out in liquid electrolytes, and allows a direct reaction between the radicals in the electrolyte and the electrode surface. Electrochemistry can be used for deposition of organic molecules in the sub-monolayer regime. The control over the electrode potential dictates the deposition rate, interface properties and the structure of the organic layer. For understanding of the electrochemical processes governing the structure and composition of hybrid organic/inorganic materials characterization of the surface and interface properties is essential.

In this work, the deposition of ultra-thin organic films was performed from benzenediazonium salt solutions. Deposition occurs when the voltage is applied on the electrode, which leads to the formation of radicals in the electrolyte through the reduction of the benzenediazonium salts. The free radicals are highly reactive and their interaction with the electrode leads to the growth of ultra thin organic layers on its surface. There is a large variety of benzenediazonium compounds with different chemical groups bounded to the benzene ring. This work presents the characterization of the nitrobenzene ($C_6H_5NO_2$), bromobenzene (C_6H_5Br), methoxybenzene ($C_6H_5OCH_3$) and 4–methoxydiphenyl amine (C_6H_5–NH–C_6H_5–OCH_3) thin films on metallic and semiconducting electrodes.

Such diversity of functional groups attached to the benzene ring offers an opportunity to tailor the surface properties. Covalent attachment of the organic molecules influences, for example, the surface electron affinity, passivates surface gap states and changes its adsorption behavior, chemical reactivity, wet-

ting, radiation absorption, adhesion, and biocompatibility [2, 3, 4]. Therefore, applications of the hybrid organic/inorganic materials are inherently diverse and stretch from photovoltaic applications [5, 6, 7] to biosensor technology [8, 9, 10].

Although the technological relevance of organically modified materials is greatly recognized, their physical and chemical properties, such as reactivity, molecular structure and their optical and electronic properties are the subjects of fundamental research. Improvement of the performance of the organic/inorganic devices demands a good understanding of the growth mechanisms and of the surface and interface structure. Therefore the characterization of electrochemically modified surfaces was undertaken in this work.

The characterization work presented in this thesis was performed using surface sensitive techniques, such as infrared spectroscopic ellipsometry (IRSE) and X-ray photoelectron spectroscopy (XPS). The measurements addressed the following important questions:

- Structure of the ultra-thin organic films
- Side reactions that take place during the deposition
- Structure of the organic/inorganic interfaces
- Interface stability to the oxidation under atmospheric conditions
- Further possibilities of surface engineering by X-ray irradiation of the thin organic layers

The choice of the IRSE method as a characterization technique was due to its high surface sensitivity to organic adsorbates, easiness of application and a possibility of measurements under ambient atmospheric conditions. The XPS technique provided complementary information on chemical composition and thickness of the organic and interface layers.

Part of this work was dedicated to development of the simulations routines based on the phenomenological optical models, which were necessary for interpretation of the IRSE spectra. This allowed us to determine optical parameters of the ultra thin organic films, their thickness and molecular orientation.

Since the uncontrolled oxidized interfaces are unwanted in device engineering, studies of interface oxidation and search for the ways to prevent it are essential. One of the aims of this work was to characterize the interface silicon oxide layer that forms between the grafted organic thin films and the silicon substrates. It was of interest to study such oxidized interfaces that form under different conditions: first, as a result of the side reactions with the surrounding aqueous solution, and second, as a result of the exposure to atmospheric conditions.

The results presented in this work rely on the cross–correlated analysis which involved mainly IRSE and XPS techniques. It allowed to perform a quantitative study of the oxide formation at the silicon/film interface. Spectra delivered by XPS technique provided information on chemical bonds in thin films and organic/inorganic interfaces. Deconvolution of the core level spectra gave an

insight onto the sub-oxide structure of the Si/SiO_x/film interfaces. Studies of the surface roughness as a result of the oxidation taking place at the organically protected and unprotected surfaces were performed using atomic force microscopy (AFM).

A special attention in this work was given to the possibility to modify the chemical structure of thin films by X-ray irradiation. This work explores the reduction of nitrobenzene on silicon surfaces (Si-$C_6H_4NO_2$) to aniline (Si-$C_6H_4NH_2$) upon X–ray irradiation. This subject is of interest since it allows a biological compatibility of the surface through the NH_2 bio–reactive functional group. The components of the reduction process are proposed upon a detailed deconvolution of the observed core levels.

This dissertation summarizes the work which addressed the above issues. Chapter 2 introduces electrochemistry as a surface modification method. The principles of the electrochemical cell are described along with the model for the grafting procedure. Creation of the radicals in the electrolyte solution and their subsequent attachment to the surface of the solid electrode are discussed. In addition, possible pathways for side reactions that may take place upon charge transfer in the aqueous electrolyte are presented.

Chapter 3 outlines the mechanisms of infrared absorption through the molecular vibrations in the investigated material. Furthermore, the ellipsometric parameters as well as the models that were used for IRSE spectral interpretations are discussed. The dispersion model for simulations of the IRSE spectra and the calculations of the radiation propagation in a stratified media are presented. In Chapter 4, experimental methods and data analysis techniques are introduced. This includes a detailed presentation of the components of the IRSE setup, and the discussion of the XPS data analysis.

In chapter 5, characterization of metallic and semiconducting surfaces modified with various benzene derivatives is presented. An emphasis is placed on methoxybenzene ($C_6H_5OCH_3$) and nitrobenzene ($C_6H_5NO_2$) modified surfaces. Simulations of the IRSE spectra are applied to evaluate the optical properties of the ultra thin organic films. Comparison with the data obtained from XPS measurements is performed for a cross referenced analysis of the thickness and the chemical composition of the surface adsorbates.

Chapter 6 introduces a detailed characterization of the SiO_x interface between the organic films and silicon surfaces. Here, oxidation of the silicon surfaces during the electrochemical grafting and its prevention are presented. A comparative analysis between the stability of the organically modified surfaces and the unmodified hydrogen passivated silicon surfaces to oxidation in atmospheric condition is performed.

Chapter 7 presents the process that converts the NO_2 nitro groups of electrochemically grafted nitrobenzene on Si surfaces into NH_2 amino groups upon X–ray irradiation. This chapter proposes a detailed mechanism for this conversion and suggests several intermediate species on the reaction pathway.

The last chapter provides a survey and conclusions of this work.

Chapter 2

Electrochemical surface modification with ultra–thin organic films

Functionalization of surfaces with organic thin films allows to control the material interfacial properties, which is important in development of device technology [11, 3]. Methods for deposition of thin organic films on metallic or semiconducting surfaces can be in general subdivided into physical [12, 13] and chemical [14,15] modifications. In case of a physical modification, physisorption of molecules on substrates takes place with a Coulomb interaction between surface and organic molecules. Chemical modification is achieved through a covalent bond of the deposited molecules with the surface (chemisorption). Surface preparation methods are diverse, stretching from ultra-high vacuum deposition [16, 17, 18, 15] to wet–chemical preparation [19, 20]. Wet–chemical preparation is of advantage for technological applications, since it can be carried out under atmospheric conditions in suitable solutions. Non–vacuum methods for surface preparation include Langmuir–Blodgett, spin–coating, electrochemical grafting and many others [11, 21].

This work focuses on characterization of ultra-thin organic films deposited electrochemically from aryldiazonium salts on inorganic electrodes. The following sections are organized as follows: first, a motivation for the organic modification from the aryldiazonium compounds will be given. Next, a detailed description of electrochemical method and its application to thin film preparation is presented. The issues related to charge transfer between the electrode and electrolyte, as well as possible side reactions connected with the grafting process, are discussed.

2.1 Aryl diazonium compounds: tailoring of the surface properties

Covalent attachment of the organic molecules to solid surfaces enables to tailor the surface properties by tuning of the electron affinity and surface dipole moment [6, 22]. Molecules used in this work allow to control surface properties by changing the functional group, X, attached at the para–position of the diazo compound from which the molecules are grafted on the surfaces, as shown schematically in Fig. 2.1. Changing the functional group X of the molecules

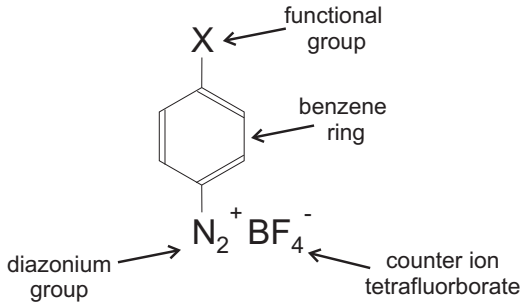

Figure 2.1: Schematic drawing of the aryl diazonium tetrafluorborate molecule with diazonium group N_2^+ and a variable group X to change between the electron acceptor and electron donor–like molecular properties. In this work, the studies were performed with X=Br, NO_2 and OCH_3.

changes their electronic properties and influences the properties of the host surface accordingly [2, 3, 4]. In this work, surfaces modified with 4–bromo– (X=Br), 4–nitro– (X=NO_2) and 4–methoxy– (X=OCH_3) benzenediazonium-tetrafluoroborate compounds (4–BrBDT, 4–NBDT, and 4–MeBDT, respectively) were studied.

Fig. 2.2 shows the energy band diagrams as proposed by Hunger et al [4] based on the observation delivered by XPS measurements. Fig. 2.2 (a) shows the schematic band diagram for a functionalized silicon surface and presents the definitions of the related surface parameters. The work function WF is defined as energy difference between the vacuum level, E_{vac} and the Fermi level, E_F. The electron affinity of the surface, χ, is defined from the bottom of the conduction band E_{cb} to the vacuum level E_{vac}. The electron affinity χ can be viewed as the modified "intrinsic electron affinity" of the Si, χ_{Si}, by a dipole contribution δ which depends on the charge distribution at the interface and within the adsorbate layer [4]:

$$\chi = \chi_{Si} + \delta \tag{2.1}$$

The step potential δ defined such that an increase of the electron affinity corresponds to $\delta > 0$.

Fig. 2.2 (b–e) show the effects of the modification of the silicon surfaces with benzene derivatives carrying different functional groups X. The functional group X influences molecular dipole moment [23]. When molecules attach to the surface, they change the surface electron affinity χ. The electron affinity depends on the molecular dipole moment and orientation of the molecules on the surface. Thus, variation of the functional group X should in general enable tailoring of the surface properties. However, processes that govern molecular

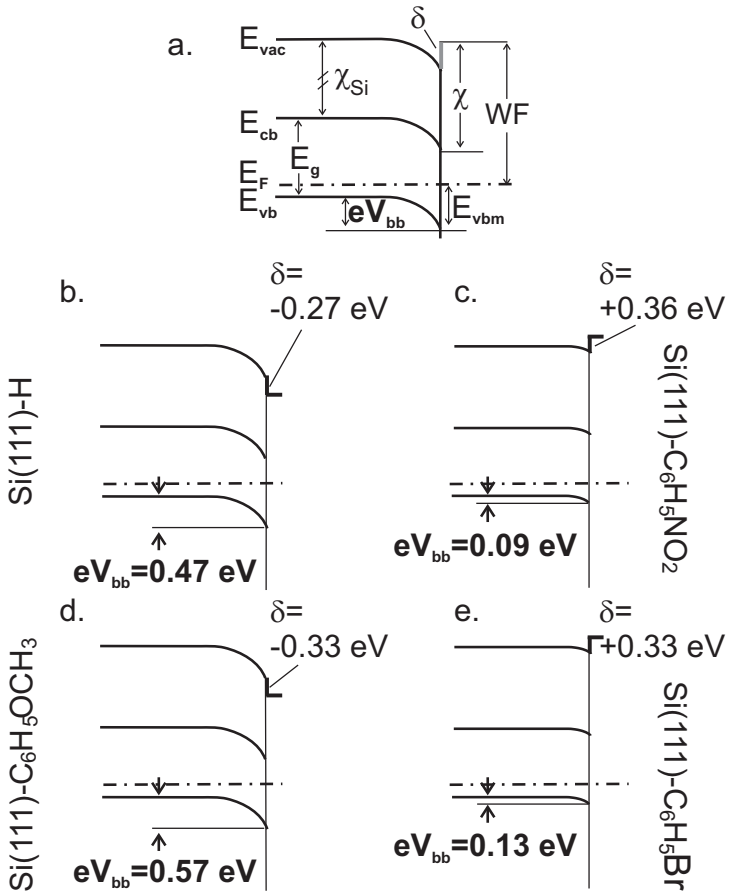

Figure 2.2: a. Energy band diagram of a functionalized silicon surface with band bending, eV_{bb}, and a surface dipole, δ, modifying the intrinsic electron affinity of silicon, χ_{Si}. b–e: Energy band diagrams of the hydrogen-terminated p–Si(111)–H (not an ideal H–termination [4])(b); nitrobenzene grafted onto p–Si(111) (c); methoxybenzene/p–Si(111) (d); bromobenzene/p–Si(111) (e). After Hunger et al [4].

orientation of the electrochemically grafted molecules on the surfaces are not

well understood. As will be shown in the following sections, one of the possible side reactions is the polymerization of the radicals in the electrolyte, which leads to formation of unordered organic films carrying polymerized units. Besides, oxidation of the organic/silicon interface may take place during the grafting in aqueous solution. In this work characterization of the electrochemically grafted films and the organic/inorganic interfaces was performed, in order to elucidate the parameters that influence those unresolved issues of the interface and thin film structure.

2.2 Electrochemical grafting

Electrochemical grafting is a method of covalent attachment of organic molecules on a surface. A typical electrochemical cell consists of electrodes and ionic conductor, or electrolyte. Application of a potential permits a charge–carrier transfer between the surface and species in solution. Deposition of organic monolayers proceed through a formation of radicals in electrolyte and their attachment to electrode through the surface reactive sites. Electrochemically grafted organic films construct the main scope of this thesis, thus a detailed discussion of this method is presented in the following subsections.

2.2.1 Electrochemical cell

A typical electrochemical cell is shown in Fig. 2.3. This arrangement is known as *three-electrode cell*, where the current is passed between the *working electrode* and the *counter* (or *auxiliary*) electrode. The potential of the *working electrode* is measured relatively to the *reference electrode*. The electrochemical grafting

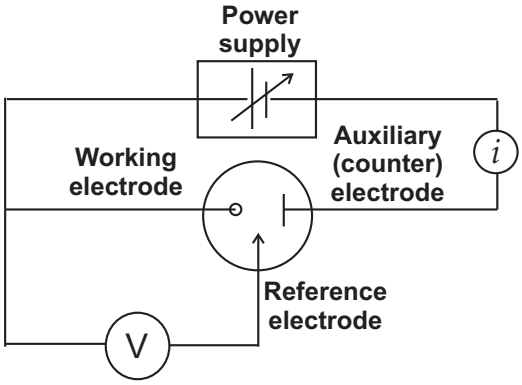

Figure 2.3: Principle of three-electrode electrochemical setup.

for instance proceeds upon application of the voltage on the working electrode. When the working electrode is driven to negative potentials, the energy of the electrons in the electrode is raised. When the Fermi level of the electrode is

above the lowest unoccupied molecular orbital (LUMO) of the species in the solution, the electron transfer from the electrode to the molecules in the solution is thermodynamically favorable (Fig. 2.4, upper panel). A flow of electrons from

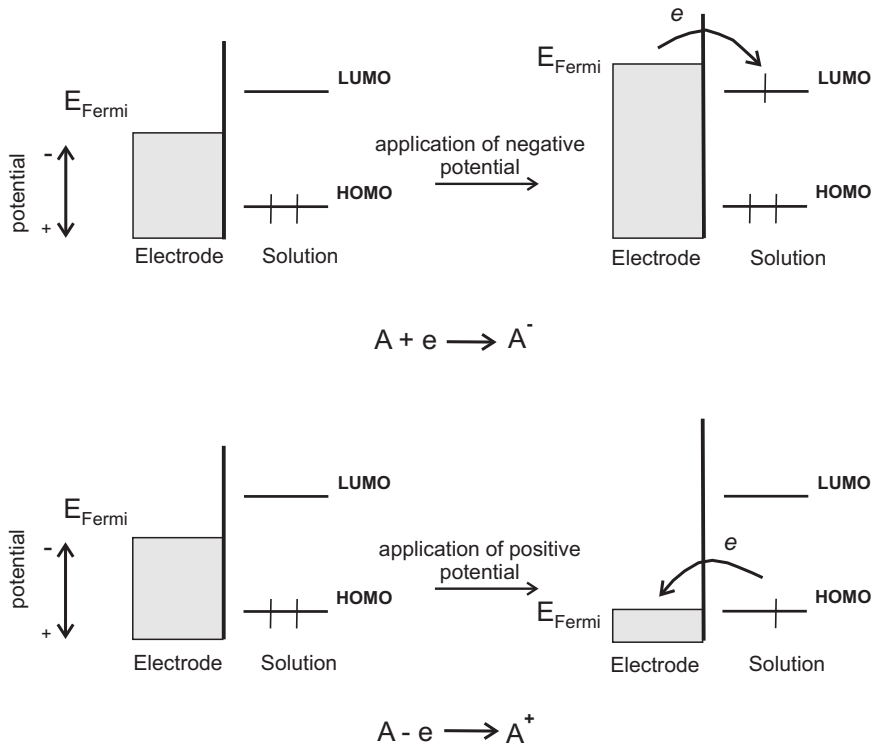

Figure 2.4: Representation of reduction (upper panel) and oxidation (lower panel) processes of species A in solution. The shown molecular orbitals of species A are the highest occupied molecular orbital (HOMO) and the lowest vacant molecular orbital (LUMO). After ref. [24].

electrode to solution is called *reduction current*. By lowering the energy of the electrons in a working electrode below the highest occupied molecular orbital (HOMO), a thermodynamically favorable energy for electron transfer from the species in the electrolyte to the electrode can be reached (Fig. 2.4, lower panel). A flow of the electron from solution to electrode is called *oxidation current*. In this work, the reported potential is referred to Au–electrode in the same solution. The calculations of the charge transfer between the electrolyte and the solid, taking into account the polarization fluctuations in solution can be found in the textbooks – see for example [1].

The main part of this work is dedicated to the studies of surfaces organically modified though electrochemical grafting from aryl diazonium salts. A model for deposition of organic layers from aryl diazonium compounds on Si surfaces was

proposed recently by Allongue et al [25]. The initial stage involves formation of the aryl radical through the reduction of the aryl diazonium ion:

$$\equiv N_2^+ - \oslash - X \ + \ e^- \longrightarrow \bullet \oslash - X \ + \ N_2 \tag{2.2}$$

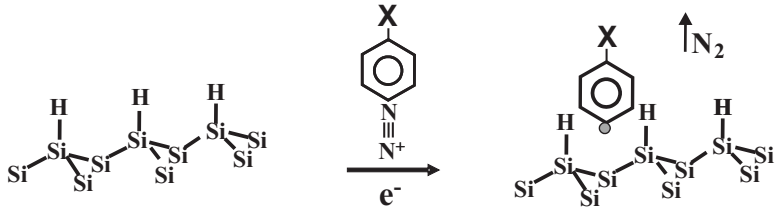

where $\oslash$ stand for benzene ring and $\bullet$ designates a radical. In the next step, hydrogen is being removed from the Si surface leaving a dangling bond behind:

$$\equiv Si - H \ + \ \bullet \oslash - X \longrightarrow \equiv Si \bullet \ + H - \oslash - X \tag{2.3}$$

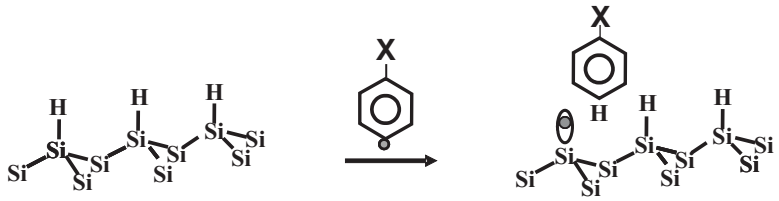

The Si dangling bond can now react with aryl radicals in the electrolyte:

$$\equiv Si \bullet \ + N_2^+ - \oslash - X \xrightarrow{e^-,\ -N_2} \equiv Si - \oslash - X \tag{2.4}$$

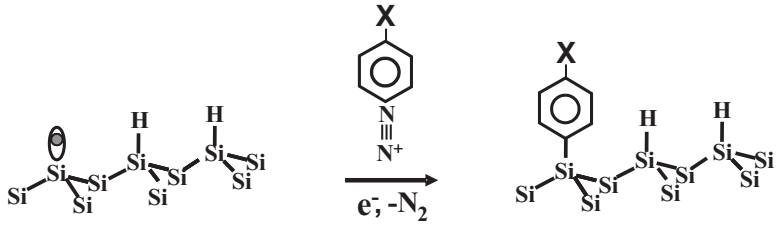

Organic monolayers from aryl diazonium salts can also be grafted on other surfaces, for example, Au or TiO_2 [26, 27, 28].

This work also presents studies on surfaces modified with Grignard reagent methylmagnesium halide (CH_3MgX, where X = Cl, Br, or I). This method for modification of silicon surfaces was explored for example by Boukherroub et al [29] for deposition of alkyl adsorbates on H:Si(111). Electrochemical deposition leads to the reaction in which CH_3MgX is split in an electrochemical process into $\bullet CH_3$ and MgX^+, and the $\bullet CH_3$ radical can be attached to the available silicon dangling bond [30]. Studies of so methylated porous silicon surfaces are presented in section 5.4.2.

2.2.2 Charge transfer from electrode into electrolyte

Electrochemical deposition can be monitored by recording a current flowing between the electrodes in electrochemical cell as a function of time. Fig. 2.5 shows the current transients during electrochemical grafting of 4–nitrobenznene (4–NB) onto hydrogenated Si(111) at different negative potentials [31]. Initially, no charge is flowing between the electrode and electrolyte. However, with the addition of the diazonium salt (at time t=0 sec in Fig. 2.5), the current increases due to the initiation of the charge transfer process. After the molecules are grafted on the surface, they block the further charge transfer from the electrode into the electrolyte, thus the current levels out at longer deposition times. Such process is called a self–limiting process. This situation is schematically depicted in Fig. 2.6, where the blocking effect of the created film is represented by a potential barrier. On the other hand, grafting of the molecules on a chemically

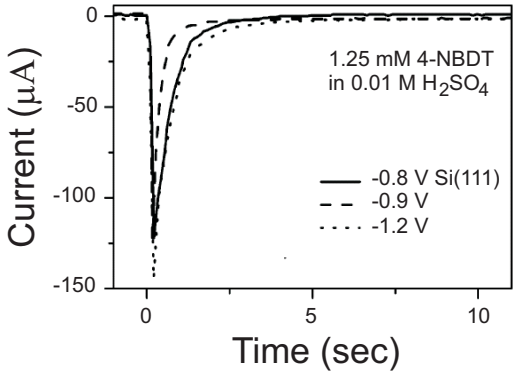

Figure 2.5: Current transients during electrochemical grafting from 4–NBDT onto hydrogenated Si(111) at different negative potentials, typical for a self–limiting process. Time scale has been set to zero when the diazonium salt was added to the solution. Adopted from ref. [31].

oxidized Si(111) surface shows a non-self-limited behavior, as shown in Fig. 2.7. Also here, the addition of the molecules into electrolyte is characterized by a steep increase of the current, as indicated by arrow in Fig. 2.7. However, in contrast to the previous example, only a slight decay in current as a function of time can be seen due to the growing film thickness and thick organic layers can be deposited on chemically oxidized Si(111) surfaces. Hartig et al [2] explained these differences on basis of the molecular orientation. Deposition of the p–nitrobenzene parallel to the amorphous SiO_2 surface allows charge-transfer via the π-bonding system, while on hydrogenated Si(111) surface, charge transfer is limited by molecules oriented perpendicularly with the molecular plane to the surface [2]. However, it is also possible that the properties of the silicon oxide layer itself are responsible for such non–limiting grafting behavior. The charge transfer from the silicon through the silicon oxide layer can be related to the

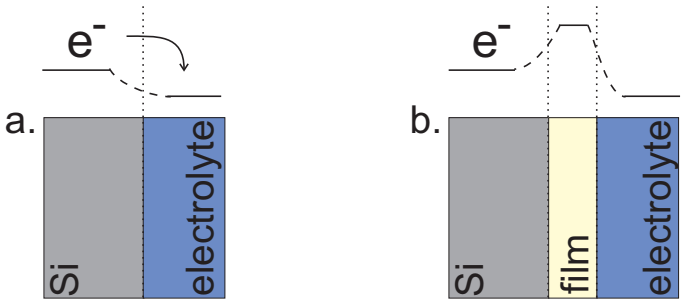

Figure 2.6: Schematic drawing of the silicon/electrolyte system and of the electron–transfer related potentials. a. Initial situation of the electron transfer under applied potential when no film was yet grown. b. Formation of the grafted film blocks the electron transfer from the electrode into electrolyte. When the film layer thickness is in the range of 20–25Å , tunneling is in principle possible [1]. Charge transfer can also be assisted by an externally applied potential.

conduction through the defects in the oxide film or incorporation of protons from electrolyte solution [32, 33]. The surface of the chemically oxidized silicon is rough [34,2,35], which also affects the charge transport from the electrode into electrolyte. It will be shown in the following sections that the results obtained by

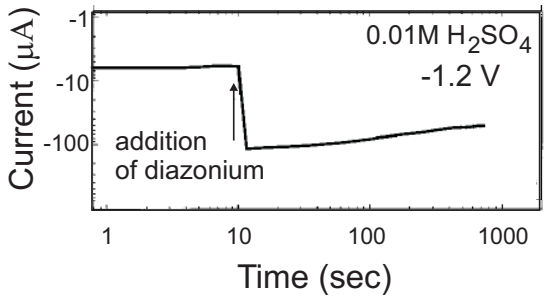

Figure 2.7: Time dependence of the current during the electrochemical grafting of p-nitrobenzene molecules at the chemically oxidized Si(111) surface, typical for a non self–limiting process. The time position of adding the diazonium salt is marked by an arrow. Adopted from ref. [2].

infrared spectroscopic ellipsometry did not indicate any preferential orientation on neither of the substrates. However, such charge-transfer behavior might be dictated by the very first layer deposited on various substrates. This situation was not detected by us, due to the high reactivity of the molecules and their polymerization during the grafting process, as will be presented further in this work.

Studies of reversibility of grafting are frequently performed using the standard method in electrochemistry of *cyclic voltammetry*. Cyclic voltammetry has become a useful technique for initial electrochemical studies of new systems and can reveal information on complicated electrode reactions. It is based on changing of the applied voltage on the electrodes, and measurements of the resulting charge transfer. Fig. 2.8 shows schematically the principle of cyclic voltammetry. As the applied potential increases, the oxidation occurs and a current due to the electron transfer from the species that are being oxidized to the electrode flows. When the potential is reversed at time t=t_0, reduction occurs and the current due to the electron transfer from the electrode to the species that are being reduced flows. The detailed theory and calculations of the charge transfer between the electrolyte and the solid, based on calculations of Marcus and Gerischer, can be found in the textbooks – see for example [1]. The earlier

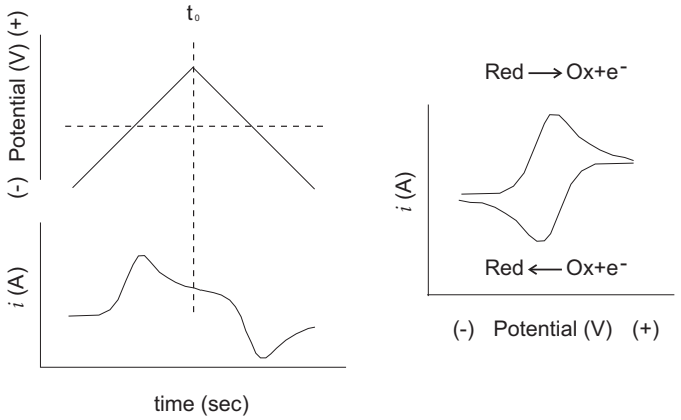

Figure 2.8: Left: cyclic potential sweep and the resulting signal as a function of time. Right: the resulting signal as a function of a potential.

studies on grafting of organic molecules from benzenediazonium compounds revealed that the functional group of the benzenediazonium has a strong influence on the grafting potential of the molecules on the electrode surface. This was shown for example in ref. [36] on metals. Deposition of thin organic films from aryl diazonium salts on TiO_2 surface and monitoring using cyclic voltammetry was performed by Merson et al [26]. The results are summarized in Fig. 2.9 for nitrobenzene (NB), methoxybenzene (MeB) and bromobenzene (BrB) deposition. All cyclic voltammograms exhibited current increase due to reduction process of the aryl diazonium salts and formation of the organic layer at the electrode. The absence of the oxidation peak during the back scan revealed an irreversible process due to the decomposition of the diazonium cation. The potential of maximum current (U_{peak}) was found to vary for each type of the grafted molecules. For NB U_{peak} occurred at -0.87 V, for BrB at -0.95 V and for MeB at -1.04 V. The U_{peak} position was found to be correlated with the dipole moment values of the studied molecules. In addition, a double-peak structure

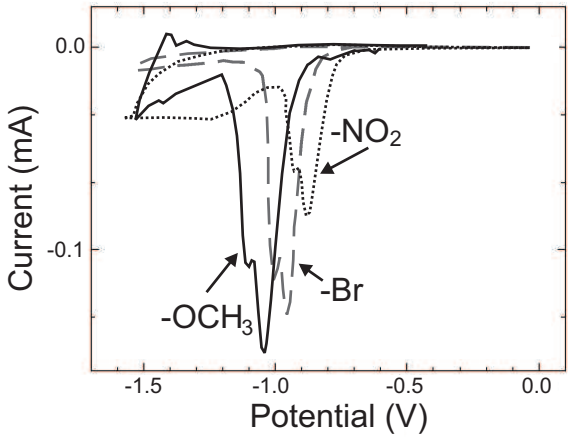

Figure 2.9: Cyclic voltammetry of TiO_2 in a 5 mM solution of nitrobenzene compound (-NO_2),bromobenzene compound (-Br) and methoxybenzene compound (-OCH_3) in 0.01 M H_2SO_4.The results are taken from ref. [26]

was observed on each voltammogram. The double peak was explained by the presence of two different sites (namely -Ti-O- and -Ti-OH) at the TiO_2 surface from which electrons can be transfered into the benzene compound. The presence of -Ti-OH surface groups is caused by protonation in acid electrolyte.

2.2.3 Side reactions during the electrochemical grafting processes

In addition to the desired process of molecular grafting, side reactions can take place in the electrochemical cell. Eq. 2.5 shows the reaction for hydrogen evolution, upon which the charge transfer from an electrode reduces protons in acidic solution, forming atomic hydrogen.

$$H^+ + e^- \rightarrow \bullet H \tag{2.5}$$

Additional side reactions involve reactions of the radicals with water. For electron acceptors, such as nitrobenzene ($R = NO_2$), possible reaction is shown in eq. 2.6:

$$R - \oslash \bullet^{\delta+} + {}^{\delta-}OH_2^{\delta+} \rightarrow R - \oslash - OH + \bullet H \tag{2.6}$$

While for electron donors, such as methoxybenzene ($R' = OCH_3$), the reaction may lead to creation of the OH radicals in the electrolyte:

$$R' - \oslash \bullet^{\delta-} + {}^{\delta+}H_2O^{\delta-} \rightarrow R' - \oslash - H + \bullet OH \tag{2.7}$$

The reactions described in Eqs. 2.5, 2.6, 2.7 lead to creation of $\bullet H$ atoms or $\bullet OH$ radicals that can participate in a creation of (and a reaction with) the

dangling bonds at Si surfaces:

$$\bullet H + H - Si \rightarrow H_2 + \bullet Si \tag{2.8}$$

$$\bullet OH + H - Si \rightarrow H_2O + \bullet Si \tag{2.9}$$

The $\bullet OH$ radicals can also react with Si dangling bonds which can lead to the back-bond oxidation at the Si surface:

$$Si - OH + Si - OH \rightarrow Si - O - Si + H_2O \tag{2.10}$$

Additional side-reactions in the electrolyte involves polymerization of organic radicals:

$$R - \oslash \bullet + \bullet \oslash - R \rightarrow R - \oslash - \oslash \ - R \tag{2.11}$$

As can be seen from the above equations, the side reactions require electron transfer from the electrode into electrolyte and will influence the current that flows between the working and the counter electrode upon application of voltage. This makes it difficult to estimate the reaction rates from the measured current and additional characterization techniques are necessary for measurements of the amount of grafted molecules.

2.3 Preparation of silicon surfaces

Two types of organically modified silicon substrates were used in this work: Si(111) and porous silicon. The main break-through in preparation of ideally hydrogen-terminated Si surfaces by chemical etching was performed by Chabal and co-workers. They discovered that the pH of a fluoride solution has an influence on flattening of the treated surfaces [37, 38]. The pH change can be achieved through the buffering of HF solutions by addition of NH_4F and/or NH_4OH [38]. This work prompted many studies and it was soon established that pure 40% NH_4F solution (pH=7–8) leads to the formation of hydrogen terminated (111) surface terraces with up to some hundreds of nm width [39, 37, 38].

Fig. 2.10 shows schematically the model for HF etching as proposed by Trucks et al [40]. Initially, removal of the hydroxide groups from the silicon surface and termination of the Si dangling bond with fluorine is illustrated (Fig. 2.10(a)). The ionic nature of the Si–F polarizes the silicon back bond as shown in Fig. 2.10(f). This polarization allows the insertion of HF into a Si–Si bond. Steps (b)–(e) in Fig. 2.10 represent the etching sequence terminating with the removal of the surface silicon atom as SiF_4 unit. From the other hand, porous silicon, as it name suggests, consists of the pores that can be created by etching of silicon atoms from atomically flat silicon surfaces as discussed in every detail elsewhere [41, 42, 43, 44, 45]. The importance of porous silicon (PSi) was recognized since the discovery of Canham in 1990 that nanocrystalline porous silicon can emit visible light through photoluminescence at room temperature [46]. However, while the construction of working devices based on PSi

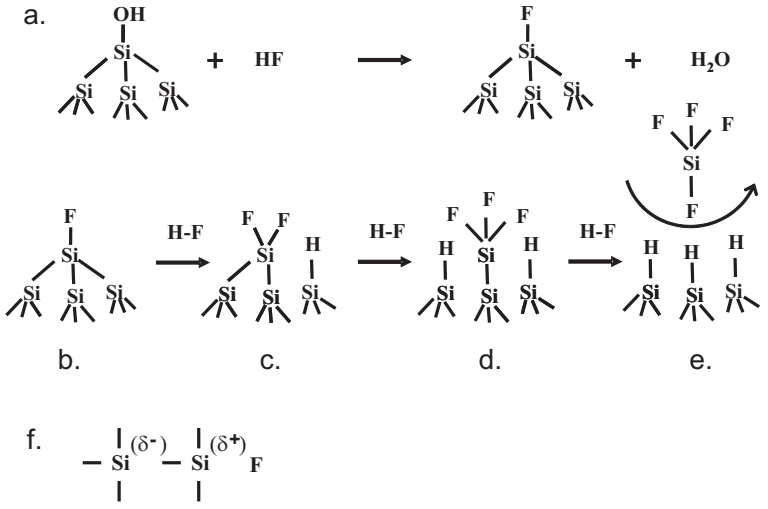

Figure 2.10: HF etching process as proposed by Trucks et al [40]. See text for the description of the process.

was reported [47,48,41], stable and strong photoluminiscence is hard to achieve. One of the promising approaches to overcome this problem can be the grafting of special molecules on to the PSi surfaces [20].

The primer interest in characterization of electrochemically modified PSi in this work was its larger surface area, and thus a higher amount of the grafted molecules per investigated spot as compared to the organically modified Si(111) and Au surfaces. In turn, this should enable a higher signal–to–noise ratio for weaker absorption bands, among them the Si–C or Si–O–C bonds that are expected to be formed in electrochemical grafting. Additionally, we expected to observe in the obtained IRSE spectra the effects due to the orientation of the grafted molecules on the walls (or the pores) of PSi.

In this work, porous silicon was formed by an anodic treatment in 50% HF:ethanol (1:1) for several minutes. The IRSE spectra obtained from freshly prepared as well as organically modified porous silicon are presented in section 5.4.

2.4 Summary

In this chapter, electrochemical methods for organic modification of solid surfaces were presented. These methods do not require ultra–high vacuum systems and can be performed under room temperature conditions. By deposition of suitable molecules, surface properties (for example, surface band-bending [4]) can be controlled. However, electrochemical grafting is a complex process which involves side–reactions such as surface oxidation and polymerization of reactive radicals. In the next chapters characterization of the electrochemically modi-

fied surfaces is presented using dedicated surface sensitive analytic techniques, such as Infrared Spectroscopic Ellipsometry (IRSE) and X-ray Photoelectron Spectroscopy (XPS). These methods enable identification of surface adsorbates, reveal the properties of organic/inorganic interfaces and the structure of thin films. Based on these methods, the results of studies on influences of the preparation conditions on the structure of the organically modified surfaces are presented in this work. Stability of the modified surfaces to ambient conditions and their chemical reactivity upon X–ray irradiation will be discussed.

Chapter 3

Optical modeling

Surface analytical methods based on Fourier-Transform Infrared (FTIR) spectroscopy constitute an important part of this work. FTIR spectroscopy is a widely used method for investigations of vibrational absorption properties of liquids, gases and solids. FTIR–based transmission and reflection techniques play a significant role in studies of molecular ordering and orientation on various surfaces: from studies of carbon monoxide chemisorption on metals [49] and preparation of flat hydrogen-terminated Si(111) surfaces [50] to studies of ultra-thin organic films properties [20].

This chapter is dedicated to the discussion of the interpretation of the FTIR spectra based on optical models. The opening section introduces a model for absorption of the infrared radiation by excitations of the molecular vibrations. Next, we introduce the models that were used throughout this work for the IR data evaluation. These include the classical Lorentz dispersion model and a model for propagation of the electromagnetic radiation in stratified media. Finally, example demonstrating the application of these models for evaluation of the measured spectra is given.

3.1 Fundamental transitions and overtones

In IR spectroscopy, the vibrational excitation is achieved by sample irradiation with a broad-band radiation source. The molecule is excited to a higher vibrational state directly by absorption of IR radiation. Atoms bound in a molecule can have only quantized energies. A simple way to describe molecular vibrations is to consider a diatomic molecule. The vibration of two nuclei in a diatomic molecule can be reduced to the motion of a single particle with reduced mass μ, whose displacement q from it's equilibrium position is equal to the change of the internuclear distance. With m_1 and m_2 being masses of two nuclei, the reduced mass reads $\frac{1}{\mu} = \frac{1}{m_1} + \frac{1}{m_2}$. Assumption of a simple parabolic potential function is shown by a dashed curve in Fig. 3.1. In this case, the system represents a

harmonic oscillator, with the potential approximated by:

$$V = \frac{1}{2}Kq^2 \tag{3.1}$$

where K is the force constant. The Schrödinger wave equation becomes:

$$\frac{d^2\Psi}{dq^2} + \frac{8\pi^2\mu}{h^2}(E - \frac{1}{2}Kq^2)\Psi = 0 \tag{3.2}$$

The eigenvalues of this equation are:

$$E = h\nu(m + \frac{1}{2}) = hc\widetilde{\nu}(m + \frac{1}{2}) \tag{3.3}$$

where $\widetilde{\nu} = 1/\lambda$ is the wavenumber with dimension cm^{-1}, notation commonly used in vibrational spectroscopy, h is the Planck constant and m is the vibrational quantum number with integer values 0,1,2... The vibration frequency is then given by:

$$\nu = \frac{1}{2\pi}\sqrt{\frac{K}{\mu}} \tag{3.4}$$

or

$$\widetilde{\nu} = \frac{1}{2\pi c}\sqrt{\frac{K}{\mu}} \tag{3.5}$$

The actual potential however can be approximated more precisely by adding a cubic term (solid line in Fig. 3.1):

$$V = \frac{1}{2}Kq^2 - Gq^3 \qquad (K >> G) \tag{3.6}$$

Which leads to the following eigenvalues:

$$E_m = hcw_e(m + \frac{1}{2}) - hcx_ew_e(m + \frac{1}{2})^2 + ... \tag{3.7}$$

where w_e is the wavenumber corrected for anharmonicty, and x_ew_e indicate the magnitude of anharmonicity. Eq. 3.7 shows that the energy levels of anharmonic oscillator are not equidistant, and the separation decreases slowly as ν increases. The anharmonicity is responsible for appearence of *overtones* and combination vibrations. From Eq. 3.7, one obtains:

$$(E_m - E_0)/hc = mw_e - x_ew_e(m^2 + m) + ... \tag{3.8}$$

Thus resulting in the following relations for the fundamental and the overtone vibrations:

Fundamental: $\widetilde{\nu_1} = w_e - 2x_ew_e$

First overtone: $\widetilde{\nu_2} = 2w_e - 6x_ew_e$

Second overtone: $\widetilde{\nu_3} = 3w_e - 12x_e w_e$

Where the values of w_e and $x_e w_e$ can be determined by observation of the overtones in the IR and Raman spectra. The coupling between several funda-

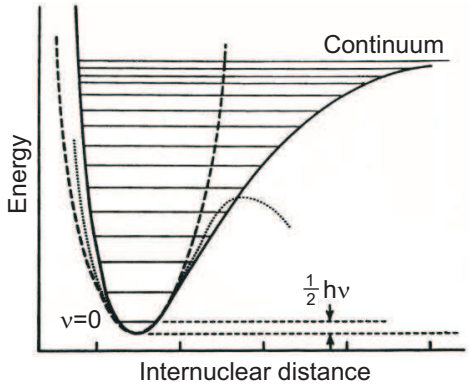

Figure 3.1: Morse potential energy curves [51] and vibrational energy levels for a diatomic molecule. Dashed line: parabolic potential, dotted line: cubic potential, solid line: actual potential including the anharmonicity correction. Adopted from ref. [52].

mental modes gives rise to the *combination* absorption bands. Both combination and overtone bands are typically much weaker than the fundamental bands. Fig. 3.2 shows transmission IR spectrum obtained from a low density polyethylene (LDPE), which demonstrates the absorption peaks due to fundamental modes of vibration marked between 650 and 1650 cm^{-1}, and the absorption peaks arising due to the combinations of those bands, as marked between 1650 and 2650 cm^{-1} [53]. Some of the combination bands include contributions from the Raman–active modes in the spectral range between 1000 and 1800 cm^{-1}, as assigned in detail by Nielsen and Holland [53].

It is important to mention *selection rule* for detection of the molecular vibrations using IR techniques. The vibration is IR–active if the transition dipole moment μ is changed during the vibration:

$$\frac{\partial \mu}{\partial q} \neq 0 \tag{3.9}$$

Where q is the normal coordinate. Thus, for example, vibrations of homopolar diatomic molecules such as N_2 or O_2 are not IR-active.

3.2 Lorentz dispersion model

In this work, the calculations of the optical properties of organic thin films were based on a macroscopic approach, employing harmonic oscillator model in

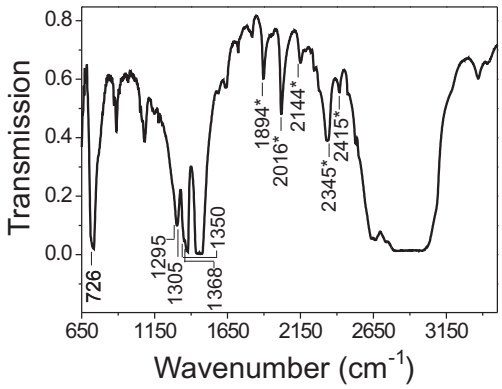

Figure 3.2: Transmission spectrum of low density polyethylene (LDPE) demonstrating the absorption peaks due to fundamental modes of vibration marked between 650 and 1650 cm^{-1}, and due to the combinations of those bands, as marked between 1650 and 2650 cm^{-1} (starred). The assignment is based on ref. [53].

Lorentz formulation. The dielectric function is defined in terms of the electric field $\mathbf{E}$ and the polarization $\mathbf{P}$ through the Maxwell equations (SI units) [54]:

$$\mathbf{D} = \epsilon_0 \mathbf{E} + \mathbf{P} = \epsilon_0 \epsilon \mathbf{E} \tag{3.10}$$

where $\mathbf{D}$ is the dielectric displacement, ϵ_0 is the free space permittivity, ϵ is the dielectric function, $\mathbf{E}$ is the electric field vector.

Molecular vibrations can be described as simple harmonic oscillators. The equation of motion of a charged harmonic oscillator with mass m and charge Q in response to the driving oscillating electric field $\mathbf{E}$ is given by [55]:

$$m\frac{d^2\mathbf{r}}{dt^2} = Q\mathbf{E} - m\omega_0^2\vec{r} - m\Gamma\frac{d\mathbf{r}}{dt} \tag{3.11}$$

where $\mathbf{r}$ is the electron displacement, w_0^2 is the resonant frequency and Γ is the damping constant. In this equation, the term $Q\mathbf{E}(\omega)$ arises from the driving force generated by the electric field, $m\omega_0^2\mathbf{r}$ is the restoring force, and the last term is due to the damping force. This equation describes the molecular vibrations [56,57] as well as the lattice absorption through optical phonons [55]. The solutions for displacement from equilibrium $\mathbf{r}$ can be expressed as:

$$\mathbf{r} = \mathbf{r}_0 \exp(i(\mathbf{k}\cdot\mathbf{r}) - wt) \tag{3.12}$$

Substitution of Eq. 3.12 into Eq. 3.11 results in:

$$\mathbf{r}_0 = \frac{Q\mathbf{E}}{\omega_{0,j}^2 - \omega^2 + i\omega\Gamma_j} \tag{3.13}$$

The charged harmonic oscillators produce a macroscopic polarization **P**:

$$\mathbf{P} = NQ\mathbf{r} \tag{3.14}$$

where N is the density of the harmonic oscillators. Substitution of 3.14 and 3.13 into 3.10 leads to the following expression:

$$\epsilon = 1 + \frac{NQ^2}{\omega_{0,j}^2 - \omega^2 + i\omega\Gamma_j} \tag{3.15}$$

For $\omega \gg \omega_0$, $\epsilon \to 1$, while for $\omega \ll \omega_0$, $\epsilon \to 1 + \frac{NQ^2}{\omega_0}$. In IR spectral range, the radiation field appears to be static to the electrons and thus high–energy contributions due to electronic transitions can be considered constant in the IR spectral range. This contribution is generally referred to as high frequency dielectric constant and denoted as ϵ_∞. When Eq. 3.15 is generalized to include a collection of single harmonic oscillators and ϵ_∞ is included to the dielectric function, one obtains:

$$\epsilon(\omega) = \epsilon_\infty + \sum_j \left(\frac{F_j}{\omega_{0,j}^2 - \omega^2 + i\omega\Gamma_j}\right) \tag{3.16}$$

where the summation is performed on the jth oscillator with an oscillator strength $F = 4\pi NQ/m$, damping constant Γ and the resonant frequency ω_0.

3.2.1 Extension of Lorentz dispersion model for amorphous solids

One of the objectives of this work is a quantitative analysis of IRSE spectra obtained from thin films/SiO_x/Si interfaces. Formation of SiO_x/Si interfaces under uncontrolled conditions (anodic oxidation in electrolyte, oxidation under atmospheric conditions) is governed by growth of amorphous SiO_2. Fig. 3.3 shows SiO_2/Si(001) interfacial structure as proposed by Tu and Tersoff [58] based on Monte–Carlo simulations. A change from a crystalline to amorphous solid introduces a distribution in bond strength and thus in oscillator frequencies. Such change can be described phenomenologically through the modification of the Lorentz dispersion model [59, 60] taking into account the distribution of the oscillator frequency around the resonance frequency $\omega_{0,j}$:

$$\epsilon(\omega) = \epsilon_\infty + \sum_j \left(\frac{1}{\sqrt{2\pi}\sigma} \int_{-\infty}^{\infty} \exp\left(-\frac{(x-\omega_{0,j})^2}{2{\sigma_j}^2}\right) \frac{F_j}{x^2 - \omega^2 + i\omega\Gamma_j} dx\right) \tag{3.17}$$

where σ_j is the gaussian half width at half maximum for the jth oscillator distribution around resonance frequency $\omega_{0,j}$.

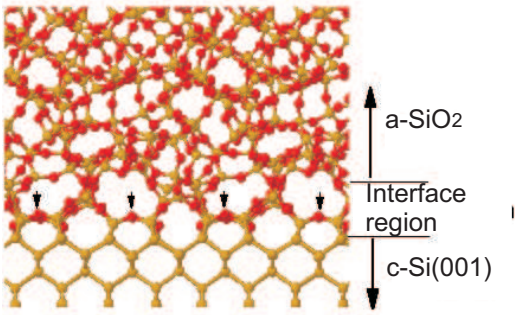

Figure 3.3: SiO_2/Si interfacial structure as proposed by Tu and Tersoff [58] based on Monte–Carlo simulations. The Si and O atoms are represented by gold and red spheres, respectively. Each arrow points to a row of oxygen atoms that form the bridges at the interface.

3.3 Propagation of polarized light in stratified media

Teitler and Henvis [61] introduced a 4×4 matrix method for studies of reflection, refraction, and transmission of light by stratified anisotropic media. The general exposition of the method was introduced by Berreman [62]. A summary of the method can be found in textbooks [63]. In this section, a brief description of the method relevant to the simulations performed in this work will be given. In the following, we assume the plane parallel electromagnetic wave whose variation with position $\mathbf{r}$ and time t is described by $\exp[i(\mathbf{k}\cdot\mathbf{r} - wt)]$ with the wave vector $\mathbf{k}$ and angular frequency w. The Maxwell equation that include the partial derivative with respect to time then reduce to:

$$\nabla \times \mathbf{E} = -\frac{iw}{c}\mathbf{B} \tag{3.18}$$

and

$$\nabla \times \mathbf{H} = -\frac{iw}{c}\mathbf{D} \tag{3.19}$$

where $\mathbf{E}$, $\mathbf{D}$, $\mathbf{H}$, $\mathbf{B}$ denote the electromagnetic field vectors. In cartesian coordinates the two Maxwell equations can be combined in the following matrix form:

$$\begin{bmatrix} 0 & 0 & 0 & 0 & -\frac{\partial}{\partial z} & \frac{\partial}{\partial y} \\ 0 & 0 & 0 & \frac{\partial}{\partial z} & 0 & -\frac{\partial}{\partial x} \\ 0 & 0 & 0 & -\frac{\partial}{\partial y} & \frac{\partial}{\partial x} & 0 \\ 0 & \frac{\partial}{\partial z} & -\frac{\partial}{\partial y} & 0 & 0 & 0 \\ -\frac{\partial}{\partial z} & 0 & \frac{\partial}{\partial x} & 0 & 0 & 0 \\ \frac{\partial}{\partial y} & -\frac{\partial}{\partial x} & 0 & 0 & 0 & 0 \end{bmatrix} \begin{bmatrix} E_x \\ E_y \\ E_z \\ H_x \\ H_y \\ H_z \end{bmatrix} e^{iwt} = \frac{iw}{c} \begin{bmatrix} D_x \\ D_y \\ D_z \\ B_x \\ B_y \\ B_z \end{bmatrix} e^{iwt} \tag{3.20}$$

Or shortly,

$$\mathbf{OG} = \frac{iw}{c}\mathbf{C} \tag{3.21}$$

where $\mathbf{O}$ is a 6x6 symmetric matrix operator, which can be partitioned into four 3x3 submatrices:

$$\mathbf{O} = \begin{bmatrix} \mathbf{0} & \nabla \\ -\nabla & \mathbf{0} \end{bmatrix} \tag{3.22}$$

With $\mathbf{0}$ denoting the 3x3 zero matrix and ∇ is as shown by the right upper corner of the 6x6 matrix in Eq. 3.20. In the absence of nonlinear optical effects and spatial dispersion, the relation between $\mathbf{G}$ and $\mathbf{C}$ can be described as:

$$\mathbf{C} = \mathbf{MG} \tag{3.23}$$

where the 6x6 matrix $\mathbf{M}$ carries the information on the anisotropic optical properties of the medium where the electromagnetic fields propagate. The optical matrix M can be written in the following form:

$$\mathbf{M} = \begin{bmatrix} \epsilon & \rho \\ \rho' & \mu \end{bmatrix} \tag{3.24}$$

where the sub–matrices ϵ and μ are the dielectric and magnetic tensors respectively. ρ and ρ' denote the optical rotation tensors. Substitution of Eq. 3.23 into Eq. 3.21 yields:

$$\mathbf{OG} = \frac{iw}{c}\mathbf{MG} \tag{3.25}$$

The particular problem of the reflection and transmission of the monochromatic plane wave incident from the isotropic ambient medium (z<0) onto an anisotropic planar structure (z>0) stratified along z–axis is shown schematically in Fig. 3.4. The symmetry of the problem suggests that there is no variation along the y direction of any field component so that $\partial/\partial y$=0. If the wave vector k_x is the x component of the incident wave, the variation of the fields in x–direction goes as $e^{-ik_x x}$. Subsequently $\partial/\partial x$=-ik_x. This significantly simplifies Eq. 3.22 and the problem reduces to the 4x4 matrix form:

$$\frac{\partial}{\partial z}\begin{bmatrix} E_x \\ H_y \\ E_y \\ -H_x \end{bmatrix} = \frac{iw}{c}\begin{bmatrix} \Delta_{11} & \Delta_{12} & \Delta_{13} & \Delta_{14} \\ \Delta_{21} & \Delta_{22} & \Delta_{23} & \Delta_{24} \\ \Delta_{31} & \Delta_{32} & \Delta_{33} & \Delta_{34} \\ \Delta_{41} & \Delta_{42} & \Delta_{43} & \Delta_{44} \end{bmatrix}\begin{bmatrix} E_x \\ H_y \\ E_y \\ -H_x \end{bmatrix} \tag{3.26}$$

Which can be represented in the following form:

$$\frac{\partial}{\partial z}\mathbf{\Psi} = -\frac{iw}{c}\mathbf{\Delta\Psi} \tag{3.27}$$

The matrix elements Δ_{ij} in Eq. 3.26 are given for example in a textbook by Azzam and Bashara [63]. In the special case when M is constant and independent of z over some continuous interval of z, Eq. 3.27 can be integrated:

$$\mathbf{\Psi}(z+h) = \mathbf{L}(h)\mathbf{\Psi}(z) \tag{3.28}$$

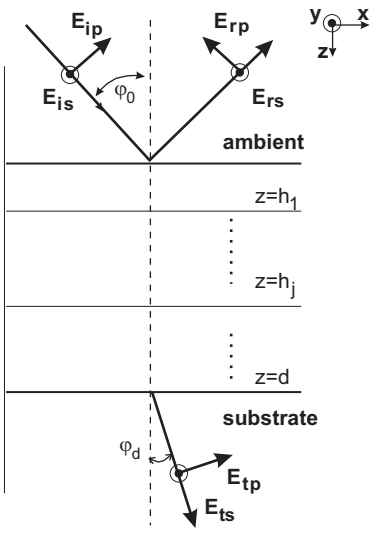

Figure 3.4: Schematic drawing of stack of homogeneous anisotropic layers with plane parallel interfaces.

where $\mathbf{L}$ is the partial transfer matrix of the layer:

$$\mathbf{L} = e^{\frac{iw}{c}h\mathbf{\Delta}} = [\mathbf{I} - \frac{iw}{c}h\mathbf{\Delta} - \frac{1}{2!}(\frac{wh}{c})^2\mathbf{\Delta}^2 - \frac{1}{3!}(\frac{wh}{c})^3\mathbf{\Delta}^3 + ...] \tag{3.29}$$

where $\mathbf{I}$ is the 4x4 identity matrix. In case of a system consisting of multiple layers the connection of electric and magnetic fields between the two surfaces at $z = 0$ and $z = d$ is obtained by a recursive application of the partial transfer matrix in layer j:

$$\mathbf{L}' = \prod_j \mathbf{L} \tag{3.30}$$

The total transfer matrix $\mathbf{L}'$ connect the surfaces at $z = 0$ and at $z = d$ through the following equation:

$$\mathbf{\Psi}(d) = \mathbf{L}'\mathbf{\Psi}(0) \tag{3.31}$$

When measurements are performed on bare substrates or on substrates with one film on top, like in the case of this work, the equations of Fresnel and Drude are sufficient to relate the ratio of reflection coefficients $\mathrm{r}_p/\mathrm{r}_s$ to the optical properties (complex indices of refraction and film thickness) of the surface. For application of Fresnel equation, the following conditions should be met: (1) the lateral dimensions of the film must be many times its thickness so that the multiply reflected and transmitted partial waves can be summed to infinity and (2) the source bandwidth, beam diameter, collimation degree and film thickness must be all such that the multiply reflected and transmitted waves combine coherently [63]. In addition, parallel surface planes of the substrates and the

film are assumed. The above conditions are fulfilled by the samples investigated in this work, thus the Fresnel theory as applied in the simulations of this work is shortly presented in the following.

Electromagnetic radiation which strikes a boundary between a medium of a given refractive index n_0 and a second medium with refractive index n_1 undergoes reflection and refraction at the boundary between the two media (Fig. 3.5). The fraction of the intensity of incident light that is reflected from the interface

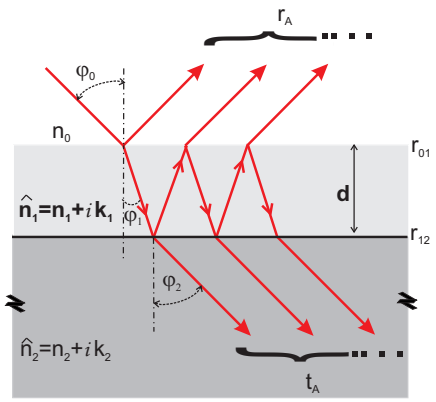

Figure 3.5: Schematic drawing of radiation propagation in a system of ambient (refractive index n_0), thin film and a substrate.

is given by the reflectance R_s and R_p, for perpendicularly and parallely polarized radiation with respect to the plane of incidence. The reflectance is given through:

$$R_{s,p} = r_{s,p} r^*_{s,p} = |r_{s,p}|^2 \tag{3.32}$$

with r^* the complex conjugate of the reflection coefficient r, for s- and p- polarizations, respectively, where the Fresnel coefficients r_s and r_p are given by:

$$r_s = \frac{n_m \cos\varphi_m - n_{m+1} \cos\varphi_{m+1}}{n_m \cos\varphi_m + n_{m+1} \cos\varphi_{m+1}} \tag{3.33}$$

$$r_p = \frac{n_{m+1} \cos\varphi_m - n_m \cos\varphi_{m+1}}{n_{m+1} \cos\varphi_m + n_m \cos\varphi_{m+1}} \tag{3.34}$$

where n is the complex refractive index, and m and $m+1$ designate two adjacent media. Within the layer, refracted radiation is reflected back and forth as outlined in Fig. 3.5. The amplitude of the wave is reduced by each reflection and additionally by the absorption on its passage through the layer. The coherent superimposition of all these contributions upon reflection is described by Airys equation:

$$r_A^{s,p} = \frac{r_{01}^{s,p} + r_{12}^{s,p} \exp(i\delta_A)}{1 + r_{01}^{s,p} r_{12}^{s,p} \exp(i\delta_A)} \tag{3.35}$$

with the phase δ_A given by:

$$\delta_A = 4\pi d\omega n_1 \cos\varphi_1 \tag{3.36}$$

with ω the optical frequency, d the film thickness and n_1 is the complex refractive index of the thin film (Fig. 3.5).

The models discussed above were employed for simulations of the spectra measured with the infrared spectroscopic ellipsometry. The principles of the ellipsometry are summarized in Fig. 3.6. Upon reflection from the sample surface, a linearly polarized radiation becomes in general elliptically polarized. The measured ellipsometric parameter $\tan\psi$ is defined as the ratio between the reflection coefficients parallel and perpendicular polarized with respect to the plane of incidence, while Δ is the measure of the phase shift between them. In other words, they can be described through the following relation:

$$\frac{r_A^p}{r_A^s} = \tan\psi \ \exp(i\Delta) \tag{3.37}$$

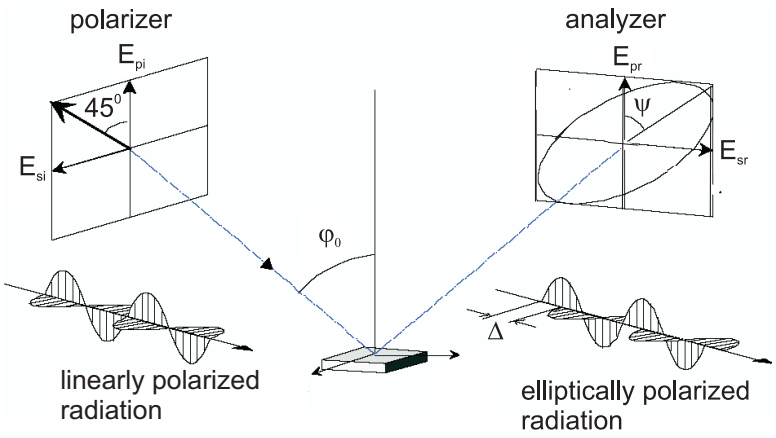

Figure 3.6: Schematic drawing of the ellipsometric principle. Due to the different complex reflection coefficients parallel and perpendicular to the plane of incidence (r_p and r_s), the light changes its polarization state after reflection at the sample surface. In general, the linearly polarized light becomes elliptically polarized and the ellipsometric parameters $\tan\psi$ and Δ are defined through: $\frac{r_p}{r_s} = \tan\psi \ \exp(i\Delta)$

Chapter 4 describes the setup which was used in this work for infrared spectroscopic ellipsometry (IRSE) measurements. There, a more detailed introduction of the ellipsometric parameters will be given. Analysis of limitations and possibilities of this technique for studies of ultra-thin organic films is presented in Appendix A.

3.4 Application of the optical models for simulations of IR ellipsometric spectra: an example of hydrogen–passivated Si(111) surface

The aim of this section is to demonstrate the application of the models described in sections 3.2 and 3.3 for simulations of the measured ellipsometric spectra. As an example, simulations of the IRSE spectra obtained from hydrogen passivated Si(111) surfaces are performed. This case was chosen due to the well defined orientation of hydrogen atoms on Si(111) surfaces. Specific molecular orientation of the molecules on solid surfaces influences the direction of the transition dipole moment arising due to the molecular vibrations. This in turn can be observed by inspection of the characteristic line shapes in the IRSE spectra. Such characteristic line shapes can be well demonstrated in case of hydrogen passivated Si(111) surfaces.

Fig. 3.7 shows schematically the transition dipole moments arising as a result of the Si–H stretching and bending vibrations. The transition dipole moment due to the δ(Si–H) bending vibrations is oriented parallel to the Si(111) surface. Thus, it interacts with the s–polarized component of the incident radiation. Consequently, δ(Si–H) absorption band would appear as a peak-up feature in IRSE tan ψ spectra (with tan ψ=$|\frac{r_p}{r_s}|$ as defined by Eq. 3.37). The transition dipole moment due to the ν(Si–H) stretching vibrations is oriented perpendicular to the Si(111) surface, thus interacting with the p–polarized component of the incident radiation. This gives rise to the absorption band appearing as a peak–down feature in tan ψ ellipsometric spectra. Fig. 3.8 shows the measured IRSE spectra obtained from hydrogen passivated Si(111) surface along with the simulated results employing the models discussed in sections 3.2 and 3.3. The spectra were measured using MCT and bolometer detectors in order to enable investigations in the extended spectral range (see section 4.1.4 for details). The tan ψ spectrum resulted in two well-distinguished peaks: the peak with its maximum at 2082 cm^{-1} originated from the stretching Si–H vibrations and the peak

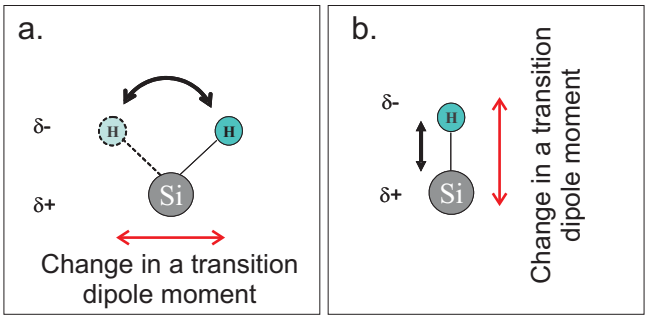

Figure 3.7: Schematic drawing of the transition dipole arising due to (a) δ(Si–H) bending and (b) ν(Si–H) stretching vibrations.

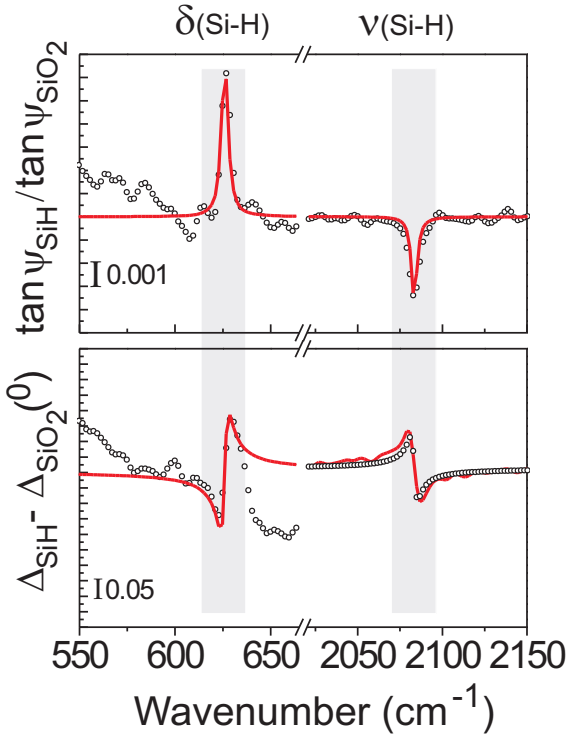

Figure 3.8: Ellipsometric spectra obtained from hydrogen passivated Si(111) surface, referenced to the spectra of oxidized Si surface. δ is bending and ν is stretching vibrations. Black circles: measured data; red line: simulated spectra. The Lorentz oscillator parameters used in the fit are described in Table 3.1.

at 626 cm^{-1} was due to the Si-H bending vibrations. This example illustrates the influence of the orientation of the transition dipole moment on the observed line shapes in IRSE spectra and the success of the Lorentz oscillator model to reproduce the measured results (the simulations are shown by a red curve in Fig. 3.8). Table 3.1 summarizes the Si–H Lorentz oscillator values. It shows that for the Si–H stretching vibration, the position of the oscillator frequency ω_0 was at 2077 cm^{-1}. However, the outcome of the simulations as shown in red in Fig. 3.8 fits well the measured spectrum with the peak positioned at 2082 cm^{-1}. This is the result of the optical effect for Lorentz oscillators with a relatively high oscillator strength F. Such optical effect is frequently referred to as Berreman effect [66].

The results of the simulations shown in Table 3.1 show that for the stretching vibrations, the x and y components of the oscillator strength F were zero, while for the bending vibrations there was no z-component (F_z=0). The issue

Vibrational mode	Frequency ω_0 (cm^{-1})	F (cm^{-2})	Γ (cm^{-1})
stretching ν(Si–H)	2077	$F_z = 32000$ F_x=F_y=0	4
bending δ(Si–H)	626	$F_z = 0$ F_x=F_y=520000	4

Table 3.1: Lorentz oscillator parameters for stretching and bending Si–H vibrational modes simulated for spectrum obtained from the hydrogen passivated Si(111) surface as shown in Fig. 3.8. In the simulations the value for the high frequency refractive index $n_\infty = 1.1$ was taken from the refs. [64, 38]. The Si-H layer thickness was taken as the length of the Si-H bond of 1.5 Å [65].

of the simulations for determination of the orientation of molecules in thin films will be addressed again later in this work in the discussion of the spectra obtained from the electrochemically deposited thin organic layers on metallic and semiconducting surfaces in chapter 5.

Chapter 4

Experimental methods

The chemical structure of the surface organic adsorbates can be readily found using different types of Fourier Transform Infrared (FTIR)–based spectroscopies. IR spectroscopy is attractive as a means of studying surface species because it can be easily adopted to versatile experimental environments as it can be operated under atmospheric conditions. IR spectroscopy can operate both in reflection and in transmission modes. While transmission mode requires at least partially transparent sample for the IR radiation to reach the detector, reflection modes can be utilized also for studies of highly reflecting metallic and semiconducting surfaces. Reflectance methods include Attenuated Total Reflection (ATR), Multiple Internal Reflection (MIR), Diffuse Reflectance Infra-red Fourier Transform (DRIFT), Infrared Spectroscopic Ellipsometry (IRSE), and Reflection–Absorption IR Spectroscopy (RAIRS, or equally IRRAS for Infrared Reflection Absorption Spectroscopy), to name a few [67]. Raman spectroscopy is usually related to as a complementary technique to infrared absorption spectroscopy. The mechanism of spectral formation is however different as Raman spectroscopy is based on inelastic scattering of photons following their interaction with vibrating molecules of the sample [68, 55]. The molecular vibration becomes Raman active if there is a modulation of the molecular polarizability. However, Raman intensities are usually low, although different approaches, such as resonant Raman [69] and surface enhanced Raman scattering (SERS) [70] can be combined for enhancement of the Raman signal.

From the above mentioned techniques, this work focuses on implementation of IRSE, which has an advantage of high surface sensitivity and does not require a vacuum for its operation. As was outlined in Fig. 3.6, IRSE enables measurements of the ratio ($\tan\psi$) between the complex reflection coefficients parallel (r_p) and perpendicular (r_s) to the plane of incidence, and the phase shift (Δ) between them – see section 3.3 for their definition.

As a complementary spectroscopic method for studies of ultra thin organic films, X-ray Photoelectron Spectroscopy (XPS) [71, 72, 73, 74] was employed. Application of the IR spectroscopy in conjunction with XPS enabled us to determine the structure of ultra-thin films and organic/inorganic interfaces.

The following sections present the description of the above techniques as employed in this work.

4.1 Infrared Spectroscopic Ellipsometry (IRSE)

Infrared spectroscopic ellipsometry is a powerful optical technique for investigations of the optical properties of thin films [75]. Its application ranges from studies of inorganic materials and films, such as SiO_2 [76, 77] or SiC [78], to studies of optical properties of ultra thin organic films [75]. Observation of the absorption bands due to molecular vibrations and phonons allows identification of the molecular composition and structure of the investigated material. High sensitivity of this method to ultra thin layers is especially valuable in the technologically relevant field of organic functionalization of surfaces for development of hybrid organic/inorganic devices.

4.1.1 IRSE setup

The definition of the measured ellipsometric parameters was given earlier in section 3.3 (see Fig. 3.6). A photograph of the infrared photometric spectrometer that was employed in this research is shown in Fig. 4.1. The setup consists of the FTIR spectrometer, polarizer P_1, analyzer P_2 and a detector. Radiation from the FTIR spectrometer is linearly polarized at the polarizer P_1. After reflection from the sample surface the radiation in general becomes elliptically polarized. The polarization state of the reflected radiation is analyzed through the analyzer. Placing a retarder in an optical path of the reflected beam enables determination of the complete set of the Stokes parameters and thus an access to additional information on the degree of polarization [79]. In general, IRSE can provide versatile information regarding molecular composition and structure of the investigated material. However, an access to this information is not straightforward and depends on the energy detection range of the detectors. Another important factor is the intensity of the radiation source which becomes more important when poorly reflecting materials are investigated. The next sections give a brief description of infrared sources and detectors that were employed in this research.

4.1.2 Measurements of the ellipsometric parameters

In photometric ellipsometry employed in our studies, the ellipsometric parameters are determined from intensity measurements at four azimuthal angles of the polarizer (0^0, 90^0, 45^0, and 135^0) at a fixed analyzer position (45^0):

$$\cos 2\psi = \frac{I(0^0) - I(90^0)}{I(0^0) + I(90^0)} \tag{4.1}$$

$$\sin 2\psi \cos \Delta = \frac{I(45^0) - I(135^0)}{I(45^0) + I(135^0)} \tag{4.2}$$

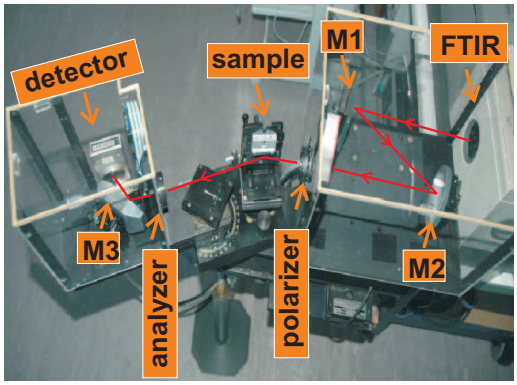

Figure 4.1: IRSE laboratory setup. Radiation from the FTIR spectrometer is linearly polarized at the polarizer. After reflection from the sample surface the radiation in general becomes elliptically polarized. The polarization state of the reflected radiation is analyzed through the analyzer. M1, M2 and M3 are the mirrors that are used for radiation direction and focusing. Radiation propagation path from FTIR to detector is shown schematically by red line.

For isotropic samples with an abrupt interface, derivation of the complex dielectric function $\widehat{\epsilon} = \epsilon_1 + i\epsilon_2$ from the ellipsometric parameters $\tan\psi$ and Δ can be performed using the following equation [56]:

$$\epsilon_1 = n^2 - k^2 = \sin^2\varphi_0(1 + \frac{\tan^2\varphi_0(\cos^2 2\psi - \sin^2 2\psi \sin^2\Delta)}{(1 + \sin 2\psi\cos\Delta)^2}) \tag{4.3}$$

$$\epsilon_2 = 2nk = \frac{-(\sin\varphi_0 \tan\varphi_0)^2 \sin 4\psi \sin\Delta}{(1 + \sin 2\psi\cos\Delta)^2} \tag{4.4}$$

where n and k are the real and imaginary parts of the complex refractive index, $\widehat{n} = n + ik$ and $\widehat{\epsilon} = \widehat{n}^2$. In practice, experimental measurements lead to so–called pseudo–optical constants $< \widehat{n} >$, which represent the optical properties of a sample as whole, i.e. an effective value which includes the film properties and the properties of the interfacial region between the isotropic bulk and the film. For a description of layered anisotropic systems, a 4x4 matrix formalism is typically used – see section 3.3 and refs. [63, 80].

Introduction of the additional element in the optical path of the reflected beam, a so–called retarder, results in an additional phase shift and improves the accuracy of determination of Δ in spectral regions where it is close to 0^0 and 180^0 [79]. Furthermore, introduction of a retarder allows determination of the degree of phase polarization - a parameter that serves as a measure of the correlation between the reflected waves. In case that the correlation is lost completely polarization degree is zero, while for homogeneous sample and ideal interfaces it is unity.

A parameter of the total degree of polarization of the radiation serves as an indicator of the depolarization effects that can take place in the sample [81]:

$$P = \sqrt{< \cos 2\psi >^2 + < \sin 2\psi >^2 \, (< \cos \Delta >^2 + < \sin \Delta >^2)} \qquad (4.5)$$

where the values in the brackets $< \cos 2\psi >$, $< \sin 2\psi >$, $< \cos \Delta >$ and $< \sin \Delta >$ stand for the mean quantities measured in the experiment. It is conventional to define a degree of phase polarization P_{ph} as a sum of the average terms of $< \cos \Delta >^2$ and $< \sin \Delta >^2$:

$$P_{ph} = \sqrt{< \cos \Delta >^2 + < \sin \Delta >^2} \qquad (4.6)$$

P_{ph} might not sum up to unity when depolarization in a sample takes place. Depolarization in a sample might occur due to scattering, lateral inhomogeneities in the refractive index of a sample, non-parallel or rough sample boundaries [81,82].

4.1.3 Broadband sources of IR radiation

Globars are the conventional broadband infrared radiation sources for FTIR spectroscopic application. In Brucker FTIR spectrometers used in this work globars present a silicon carbide rod of 5 to 10 mm width and 20 to 50 mm length, which emit electromagnetic radiation when electrically heated in the range of 1500 – 2000 K. In order to achieve a good signal-to-noise (SNR) ratio for ultra-thin organic films, we typically focused the radiation into a spot of about 6 mm^2 on the sample plane. Higher lateral resolution in the IR spectral range could be achieved at the advanced synchrotron radiation source with a superior SNR as compared to the globar source, when using a similar irradiated spot on the sample plane. Advantage of the synchrotron source over the conventional globar lies in its *brilliance* - it emits more photons per unit area into a unit solid angle [83]. Fig. 4.2 shows the comparison between the brilliance of black–body radiation at 1200K and the calculated BESSY II brilliance.

Using the above brilliance advantage of the synchrotron source, it is possible to study sample inhomogeneities and molecular distribution on the sample surface of organically modified samples. For instance, Fig. 4.3 (a) shows our results from the mapping of a 430 μm thick inhomogeneous low-density polyethylene (LDPE) sample performed at the IRIS infrared beamline at BESSY II, with a 6 mm distance between the scanned spots [82]. There are clear differences between the spectra obtained at different lateral locations, due to the sample inhomogenieties [82]. Fig. 4.3 (b) shows an enlarged section of the above spectra, where a fringe pattern is clearly visible when scanned with synchrotron radiation (spectra shown in black). This pattern arises from back-and-forth reflection of radiation from the sample interfaces. However, the interferences are absent from the spectra obtained with the globar source (shown in Fig. 4.3 (b) as a smooth grey line), for which the irradiated spot was around 50 mm^2. This is because the phase correlation is completely eliminated when the radiation wave fronts are transmitted through the inhomogeneous sample (where the thickness

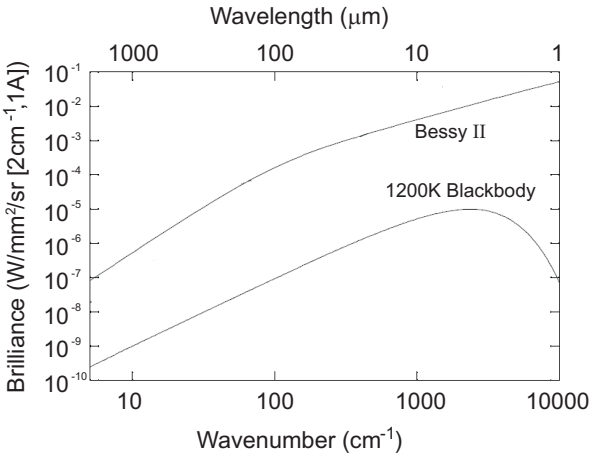

Figure 4.2: Comparison between globar and BESSY II brilliance. The brilliance was calculated using the far-field approach taking into account the intrinsic beam size in the center of the bending magnet as well as the source size due to projection and diffraction. The brilliance is quoted per 1 Ampere ring current, resolution of 2 cm^{-1}. Adopted from [83].

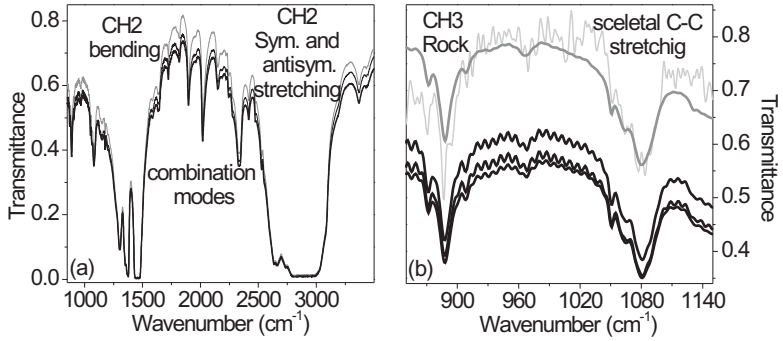

Figure 4.3: Transmittance spectra obtained for three different LDPE sample locations using the synchrotron radiation source (black). (b): enlarged section of (a). Dark gray line: a spectrum taken with the globar radiation source. Light gray line: a spectrum taken with the globar source with an additional 1 mm^2 aperture placed in front of the LDPE sample. The spectra taken with globar radiation are offset by 0.2 for clarity [82]. Peak assignment was done on the basis of ref. [84].

and structural inhomogeneities cause each wave front at different sample positions to experience different optical paths). The other globar spectrum, shown in Fig. 4.3 (b), was taken with an additional aperture of about 1 mm^2 in front of the sample, limiting the globar radiation to the same area in the sample plane as when using the synchrotron radiation. However, the signal-to-noise ratio in this case was insufficient to observe a spectral fringe pattern.

This example illustrates the importance of brilliant synchrotron sources in investigations of inhomogeneous samples. In this research, it was employed to study grafted organic thin films in order to access a high–spatial resolution data [27].

4.1.4 Detectors of IR radiation

Detectors can be characterized by their responsivity, detectivity and noise equivalent power. The responsivity of an infrared detector R(T, f) represents the output signal voltage (or current) in response to input radiation from a black body at absolute temperature T, with the operating electrical frequency f [85, 86]:

$$R(T, f) = \frac{v_S}{\Phi_{s,bb}} \tag{4.7}$$

where v_S is the rms signal voltage at the output of a detector, $\Phi_{s,bb}$ is rms radiant flux from a black body. Detectivity D* is defined as the rms signal–to–noise in a 1 Hz bandwidth per unit incident radiant power per square root detector area. The units of D* are $\sqrt{Hz}/watt$. In terms of measurement parameters, D* is given by [85, 86]:

$$D^* = \frac{\sqrt{A_D \Delta f}}{\Phi_{s,bb}} \frac{v_S}{v_N} \tag{4.8}$$

where A_D is the detector area in cm^2, Δf is the electrical bandwidth in Hz, v_S/v_N is the rms signal–to–noise voltage ratio (the noise measured in the bandwidth Δf) and $\Phi_{s,bb}$ is rms radiant flux. The Noise Equivalent Power (NEP) is the rms incident radiant power which gives rise to an rms signal voltage (or current) equal to the rms noise voltage (or current). The NEP is related to D* by:

$$\text{NEP} = \frac{\sqrt{A_D \Delta f}}{D^*} \tag{4.9}$$

The units of NEP are *watts*.

In this work, thermal and photon detectors for the detection of infrared power were used. Photon detectors exhibit a selective wavelength dependence of the response per unit incident radiation power. On the other hand, thermal detectors are wavelength independent. Idealized representations of these two types of response are schematically illustrated in Fig. 4.4. Most of the spectra in this work were obtained using photon MCT (mercury–cadmium–telluride, HgCdTe) detectors due to their higher detectivity as compared to the thermal detectors in the mid–IR spectral range. However, the performance of liquid nitrogen cooled photon detectors fails below that of the liquid–He cooled thermal

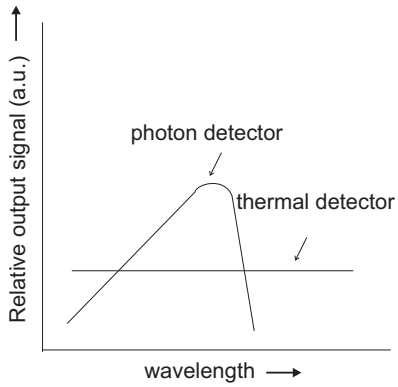

Figure 4.4: Schematic representation of spectral response of photon and thermal detectors for unit radiant power per unit wavelength interval [85].

detectors in the spectral range above 10 μm (see Fig. 4.5). In this work, an attempt was performed to extend the performance of the conventional bolometer detector, which is used for far–infrared applications, to the range between 1000 cm^{-1} to 500 cm^{-1} for detection of the molecular vibrations in this spectral range. The bolometer is a thermal infrared detector which employs an electrical resistance thermometer to measure the temperature of the radiation absorber. Typical composite bolometer consists of the *radiation absorber* with a size appropriate to intercept the signal to be measured, a large absorptivity over the frequency range of interest, and a low heat capacity. The *supporting substrate* has a low heat capacity and large thermal conductivity, so that it remains isothermal during bolometer operation. The *thermometer* is thermally attached to the radiation absorber and/or the supporting substrate. It has low heat capacity, low electrical noise, and an adequate temperature dependence of its electrical resistance. The *thermal link*, which connects the thermally active portions of the bolometer to the heat sink has low heat capacity and an appropriate thermal conductance for the required application. The *heat sink* has a stable temperature appropriate for the application. The mechanical support for the thermally active portion of the bolometer has low heat capacity, low thermal conductance, and must be stiff enough that the mechanical resonant frequencies are higher than the operating frequency of the bolometer. The photograph of the bolometer employed in this work is shown in Fig. 4.6. In this work, a *composite* bolometer type was used. A suitably blackened diamond absorber thermally bonded to the bolometer. The absorbing layer thickness is generally selected to minimize fringing effects. A parabolic Winston cone was gold-plated to prevent tarnish and to improve thermal properties. Infrared cut-on filter consisting of white polyethylene overlay on one face with diamond scatter particles was used to prevent thermal heating of the bolometer and to allow operation up to 1000 cm^{-1}. Fig. 4.7 shows intensity recorded at the bolometer when three

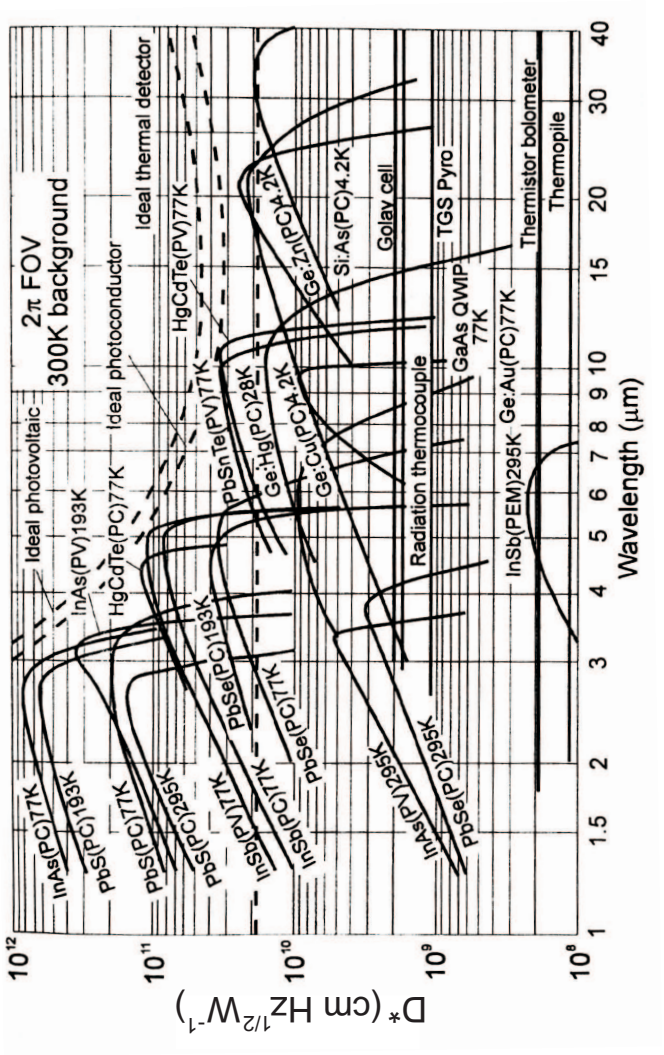

Figure 4.5: Comparison of the D* of various commercially available infrared detectors when operated at the indicated temperature. Reproduced from ref. [87].

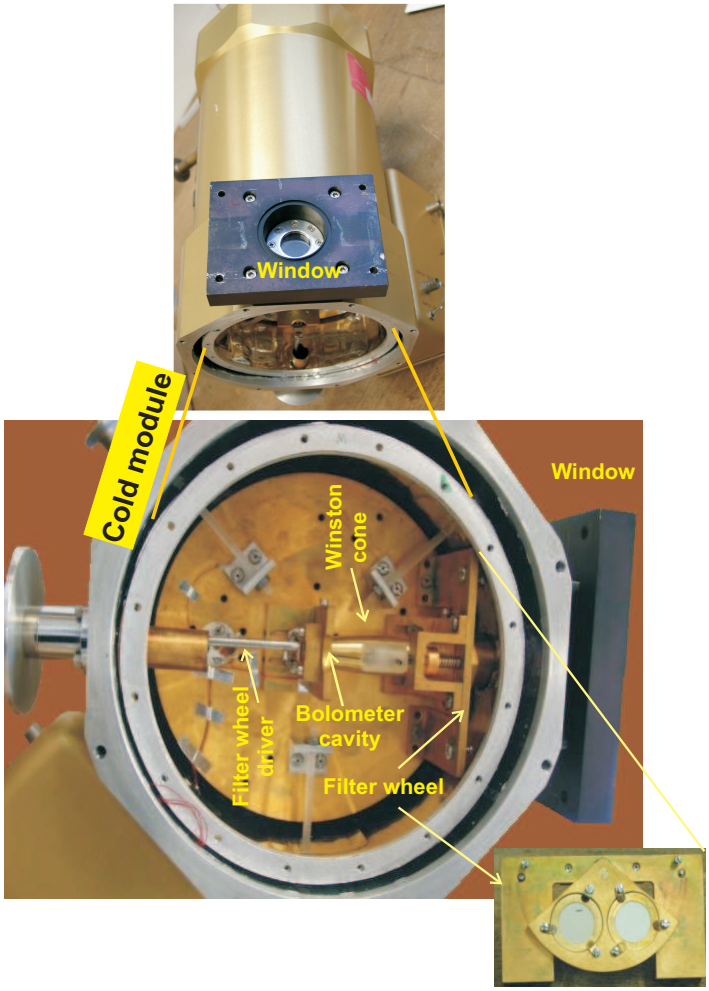

Figure 4.6: Photograph of a bolometer that was used in this work.

different outer vacuum windows were used. The main source of the bolometer

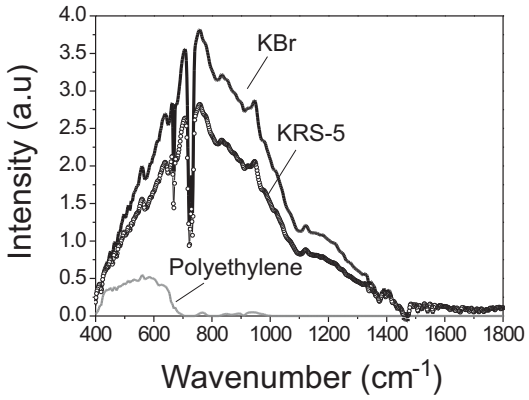

Figure 4.7: Intensity detected by a bolometer through different outer vacuum windows, consisting of wedged polyethylene overcoated on the inner face with diamond layer, KRS-5 and KBr windows, as marked on the figure. The spectra were recorded at the ellipsometer after a passage through two non-crossed wire-grid polarizers and mirror optics.

noise is the thermal fluctuation noise. Other noise sources are the shot noise, the $1/f$ noise related to the electric contacts, low frequency noise due to changes in the temperature of the heat sink and the noise related to the first stages of amplification [88].

Another thermal detector that was used in this work was a thermal DTGS (deuterated triglycine sulfate) detector, whose operation is based on the pyroelectric effect. In this effect, absorption of infrared radiation raises the temperature of the absorber, which changes the surface charge [86, 54]. With the appropriate external circuit, this change in surface charge leads to a signal voltage. The detector works under room temperature conditions. This detector in principle also works in the desired spectral range between 1000 cm^{-1} and 500 cm^{-1}. The comparison of the bolometer performance in this work to that of the DTGS detector is shown in Fig. 4.8 (a)). Although the extension of the bolometer performance toward 500 cm^{-1} – 1000 cm^{-1} can be considered to be successful (see results in sections 5.4.1 and 6.1) and it had a lower noise level when compared with DTGS (Fig. 4.8 (a)) there were some disadvantages and unresolved problems. The main disadvantage was the expensive liquid–He cooling. One of the problems was an interference effect that we believe resulted from the bolometer detection area (probably in an absorber which was designed for far-infrared applications), or from the interferences in the Winston cone. These interferences accompanied all of our measurements (Fig. 4.8 (b)). In order to get rid of them, it was necessary to reference all of the results to the spectra

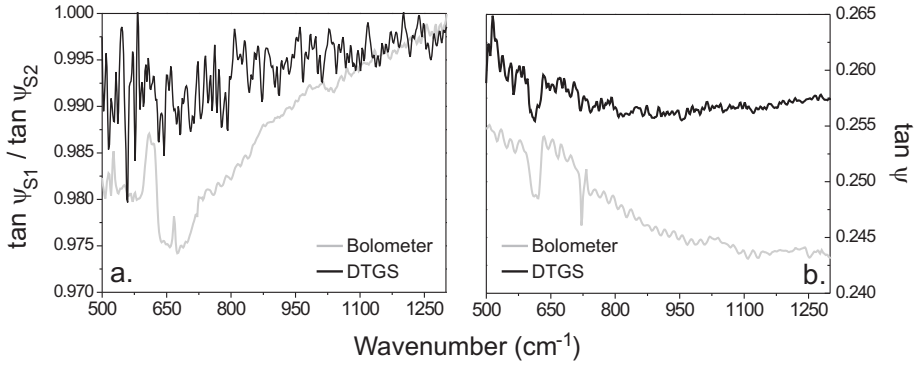

Figure 4.8: Comparison of performance between two thermal detectors: DTGS and liquid He-cooled bolometer. a. The ratio between tan ψ spectrum obtained from HF-treated Si(001) surface and tan ψ spectrum from NH_4F–treated Si(001) surface. b. Non-referenced tan ψ spectra from NH_4F–treated Si(001) surface. Interference pattern accompanies bolometer measurements, arising from the bolometer detection area. Spectra were obtained at 7.5 KHz scanning frequency with 3.5 mm Jaquinot aperture in all cases.

obtained from bare substrates. This task required a careful alignment of the whole setup, in order to assure that the radiation exactly retraces its passage for both samples. Such effect is not surprising since the bolometer detection area was designed for longer wavelength in far-IR region.

The limit of the thermal detectors performance is set by their main noise source, which is the "thermal noise". This noise sets the ultimate limit to the minimum signal detected by a perfect thermal detector. From thermodynamical considerations, the fluctuations in arrival and emission rates of photon on a thermal detector lead to a root mean square fluctuation in radiant power $\Delta\Phi$ [85, 86]:

$$\text{NEP} = \Delta\Phi = \sqrt{(16 A_d k_B \sigma \epsilon T_d^5 \Delta f)} \tag{4.10}$$

where ϵ is the emissivity, σ is the Stefan-Boltzmann constant (σ=5.67x10^{-12} Jcm^{-2}K^{-4}), k_B is Boltzmann constant (k_B=1.38x10^{-23}JK^{-1}) and A_d is the receiving area. In ideal case, all incident power will be absorbed by a detector with ϵ=1. At this limit, the minimum detectable power is NEP=$\Delta\Phi$=5x10^{-12}W, assuming T=300K, A_d=1 mm^2 and Δf=1 Hz. For operation under cryogenic conditions, or for operation in outer space with the cosmic background radiation at 3 K, the limiting sensitivity becomes NEP(3K)=5.5x10^{-16}W.

4.2 X-ray photoelectron spectroscopy

X-ray photoelectron spectroscopy (XPS) is a surface analysis technique which allows to study core–level structure of the atoms comprising the sample surface and thus to investigate the surface chemical composition. X-ray excitation causes ionization of atoms, as schematically shown in Fig. 4.9. The kinetic energy E_{kin} of an emitted photoelectron is given by:

$$E_{kin} = h\nu - E_B - W_F \tag{4.11}$$

where $h\nu$ is the photon energy, E_B is the binding energy relative to the Fermi level, and W_F is the work function (Fig. 4.9) The typical depth sensitivity of

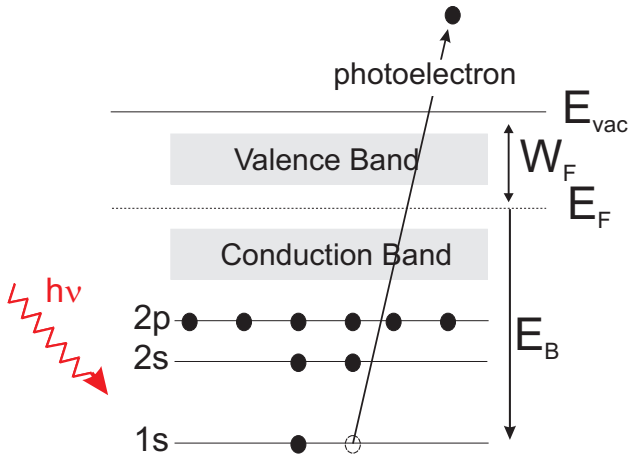

Figure 4.9: Schematic presentation of a photoemission process. E_{vac} is a vacuum level, W_F is a work function, E_F is a Fermi potential and E_B is the binding energy.

XPS as a function of the electron energy is given by *inelastic mean free path* (IMFP), as shown in Fig. 4.10. IMFP is the distance that electrons travel in material before being inelastically scattered. In a range between 50 eV to 100 eV the escape depth is lower than 1 nm, thus information obtained in this spectral range is very surface–sensitive. XPS analysis allows studies of core-level and valence structure of surface atoms. An important information on structure of bonded atoms can be revealed from observation of *chemical shifts* of the respective core-levels. For instance, XPS has been extensively used in order to establish interface structure and suboxide distribution of technologically important SiO_2/Si surfaces – see for example refs. [90, 91]. Different oxidation states of the Si atoms bonded to 0, 1, 2, 3 or 4 oxygen atoms give rise to the chemical shifts, where the respective photoemission core-level peaks appear at higher binding energy as the oxidation state of the Si atoms grows. XPS became a popular and useful technique in investigations of structure of modified

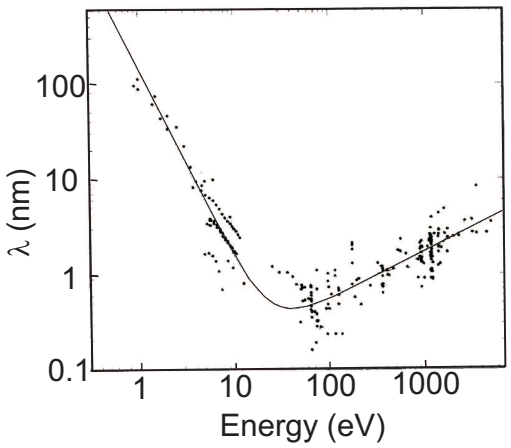

Figure 4.10: The mean free path of the electrons in solid as a function of their kinetic energy. The doted data represent measurements from different elements. Adopted from ref. [89].

surfaces with organic monolayers [92,4]. It allows to study chemical structure of the organic monolayers, to analyze the interface between the substrate and the layer and to estimate the layer thickness. In addition to the core-level peaks, *satellite* peaks due to final state effects can be also observed in the XPS spectra.

Fig. 4.11 shows schematically possible processes upon removal of the electron from the core level. The *shake–up* satellite occurs upon relaxation of the valence electrons in response to the loss of the core electron. The energy required for this transition is then absent from the kinetic energy of the photoelectron, thus this two-electron process leads to the discrete structure on the low kinetic energy side of the spectrum (or, equally, at a higher binding energy). In our work, we dealt with the spectra from aromatic systems, which show shake-up satellites with intensities of up to 10% of the primary peak. In aromatic systems the satellite structure is due to $\pi \rightarrow \pi^*$, excitations, involving the highest occupied molecular orbitals and lowest unoccupied molecular orbital (HOMO-LUMO) transitions [93,92]. These satellites therefore can serve as an indication of system aromaticity. The *shake-off* satellites, on the other hand, result in emission of the valence electron into the unbound continuum state. This process leaves an ion with vacancies in both the core level and a valence level. In this case, the energy separation from the main peak is much bigger than for the shake-up satellites, and the satellites tend to fall within the region of the broad inelastic tail of the XPS spectrum. Additional possibility is an emission of an *Auger* electron. Following the creation of the core hole by X–rays ionization, the atom relaxes by filling the hole via a transition from an outer level. As a result of the transition, an excess energy becomes available as a kinetic energy for ejection of an electron from the atom. The experiments described in this work were performed at

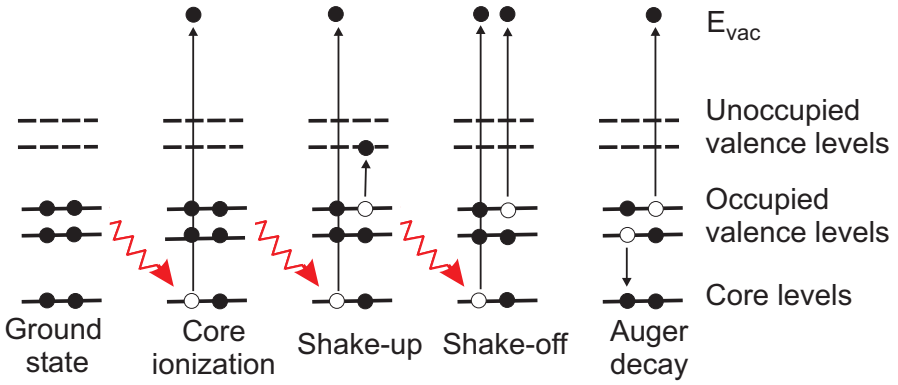

Figure 4.11: Processes occurring upon X-ray irradiation.

the BESSY-II synchrotron facility, at the undulator beamline U49/2-PGM2 using the SoLiAS experimental station [94]. Synchrotron radiation source offers superior resolution compared to conventional instruments, which allowed us to perform a careful spectral deconvolution. It is also possible to tune the energy for surface-specific measurements. Spectra were acquired in normal emission using a Phoibos 150 MCD9 analyzer from SPECS GmbH. The photoelectron spectra were referenced to the Fermi energy. In the next sections we briefly discuss the methods for analysis of the XPS spectra.

4.2.1 Deconvolution of XPS spectra

The fitting of the core-levels was performed using Voigt profile, which is a convolution of the Gaussian and Lorentzian lineshapes. The Voigt profile takes into account the experimental resolution, thermal (phonon) broadening and the core-hole lifetime. Typically, Shirley [95] or Tougaard [96] background subtraction methods are used to remove the background due to inelastic electron scattering. In Shirley background subtraction type, the background at any point is assumed to arise from the scattering of electrons of higher kinetic energy. The background is thus proportional to the integrated area above the high E_{kin} side of the peak. The Tougaard background [96] is based on similar considerations but takes into account the differential inelastic electron scattering cross-section and scales it with the number of electrons emitted. In our case, both of the above methods gave similar results, thus we used either of these backgrounds for fitting the measured spectra.

4.2.2 Evaluation of the XPS spectra

Solid state photoemission can be described as a three–step process, upon which the electron is first optically excited by the energy $h\nu$ of the incident radiation; then the electron travels through the solid and eventually the electron escapes

into the vacuum with the kinetic energy E_{kin} [97]. The detected core–level intensity (number of the photoelectrons per second) from an orbital of the constituent atoms is dependent on the atomic density n (number of the atoms per cm^3), the flux f of the X–ray photons impinging on the sample (in photons cm^{-2} s^{-1}), the photoelectric cross–section σ for the particular transition (in cm^2 per atom), the angular efficiency factor ϕ for the instrumental arrangement (the angle between photon path and the emitted photoelectron that is detected), the efficiency photoelectron process y, the area A from which the electrons are detected, the efficiency of detection T and the mean free path λ [98]:

$$I = nf\sigma\phi yAT\lambda \tag{4.12}$$

The set–up dependent constants f,ϕ, A, T and the efficiency photoelectron process y we denote as S (S=$f\phi yAT$).

For a layered system of interest (for example, SiO_2/Si or organic/Si), the intensity from the investigated atomic line is obtained by integrating over the exponential escape probability:

$$I_l = Sn_l\sigma_l \int_0^d \exp(-z/\lambda_l)dz = n_l\sigma_l\lambda_l[1 - \exp(-d/\lambda_l)] \tag{4.13}$$

where I_l is the integrated peak intensity due to the layer-characteristic emission, σ_l is the atomic photoionization cross section, λ_l is the escape depth from the layer, and n_l is the density of atoms in the layer.

The emission from the substrate is given by a similar expression where the escape probability is multiplied by the attenuation factor $\exp(-d/\lambda_l)$ of the overlayer:

$$I_{sub} = Sn_{sub}\sigma_{sub}\exp(-d/\lambda_l)\int_0^\infty \exp(-z/\lambda_{sub})dz = n_{sub}\sigma_{sub}\lambda_{sub}\exp(-d/\lambda_l) \tag{4.14}$$

with σ_{sub}, λ_{sub} and n_{sub} the atomic photoionization cross section, the escape depth, and density of atoms in a substrate, respectively. The ratio of the equations above results in:

$$\frac{I_l}{I_{sub}} = \frac{c_l}{c_{sub}}[\exp(d/\lambda_l) - 1] \tag{4.15}$$

with $c_l = n_l\sigma_l\lambda_l$ and $c_{sub} = n_{sub}\sigma_{sub}\lambda_{sub}$. Using Eq. 4.15, one can determine the thickness of the overlayer.

In this work, we performed also studies of interface island-structure, for which the modification of the above equations was necessary. The model is outlined in Fig. 4.12, where a sample consists of a substrate, of island-structured interfacial layer and of the organic overlayer. For our samples, this structure may represent a Si substrate, partly oxidize SiO_x interfacial layer and the grafted thin organic film, as will be discussed later in this work. For many organic materials, literature cites quite diverse IMFP values or no data at all can be available. For organic thin films in this work IMFP values from ref. [99] were used. However,

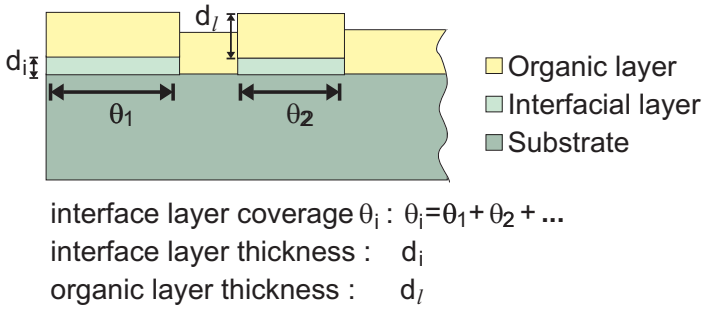

Figure 4.12: Layer model with island interfacial layer. Coverage and thicknesses of the interfacial and organic layers are defined in the figure.

if one is interested in the ratio $\frac{I_i}{I_{sub}}$ with I_i being the integrated intensity from the interface layer, the contribution from the upper layer will be canceled out under assumption that the organic layer with the same thickness d_l covers the substrate and the interfacial layer. Keeping this in mind, we designate the contribution from the organic layer as α_l, which is a constant. The core–level intensity I_i from the interfacial layer can be obtained similarly to Eq. 4.13:

$$I_i = S\theta_i\alpha_l n_i\sigma_i \int_0^{d_i} \exp(-z/\lambda_i)dz = \theta_i\alpha_l n_i\sigma_i\lambda_i[1-\exp(-d/\lambda_i)] \tag{4.16}$$

with the interface layer coverage θ_i and thickness d_i. For the substrate, the core–level intensity can be separated into two parts: one that comes from areas not covered with the interface layer (I^a_{sub}) and the other that comes from below the interface–layer, (I^b_{sub}). (I^a_{sub}) can be expressed as:

$$I^a_{sub} = S(1-\theta_i)\alpha_l n_{sub}\sigma_{sub} \int_0^{\infty} \exp(-z/\lambda_{sub})dz = (1-\theta_i)\alpha_l n_{sub}\sigma_{sub}\lambda_{sub} \tag{4.17}$$

whereas for the (I^b_{sub}) the escape probability is multiplied by the attenuation factor coming from the interfacial overlayer:

$$I^b_{sub} = S\theta_i\alpha_l n_{sub}\sigma_{sub}\exp(-d_/\lambda_i) \int_0^{\infty} \exp(-z/\lambda_{sub})dz = \theta_i\alpha_l c_{sub}\exp(-d_i/\lambda_i) \tag{4.18}$$

where c_{sub} was defined earlier in this section. Combining the equations above, we get:

$$\frac{I_i}{I_{sub}} = \frac{I_i}{I^a_{sub}+I^b_{sub}} = \frac{c_i}{c_{sub}} \frac{\theta_i(1-\exp(\frac{-d_i}{\lambda_i}))}{\theta_i(\exp(\frac{-d_i}{\lambda_i})-1)+1} \tag{4.19}$$

with $c_i = n_i\sigma_i\lambda_i$. Eq. 4.19 can be solved for coverage θ_i and thickness d_i where the value of $\frac{I_i}{I_{sub}}$ is estimated from two measurements at two different photon energies.

Using the evaluated interface coverage θ_i and thickness d_i as an input, the evaluation of the thickness of the organic overlayer was performed in this work with the dedicated XPS Multiquant program [100]. Additional input data which is required by the program is the integrated intensities of the measured XPS lines. The program allows several geometry models where we used the one as outlined in Fig. 4.12.

Chapter 5

Optical properties of organic thin films

In this chapter the studies of electrochemically grafted thin organic layers on TiO_2, Si(111), Au and porous silicon surfaces are described. As was shown in section 2.2.1, grafting of the thin films from the aryl diazonium salts starts from the split of the benzenediazonium into the benzene radical carrying the specific functional group and the N_2. The released benzene radicals are then grafted into the electrode. IR spectra of the aryl diazonium salts, which is presented in this chapter, provided information on the structure of this initial compound. In addition, these spectra exhibit the absorption bands that one should expect in the spectra from the grafted ultra thin organic films.

After the grafting, identification of the molecular adsorbates and the orientation of the molecules in thin films was performed based on the observation of the respective absorption peaks in the IRSE spectra and their simulations in the optical models. This chapter shows that no preferential orientation was observed for the organic molecules grafted from the benzenediazonium salts on Si(111), Au, TiO_2 and porous silicon substrates. However, IRSE spectra obtained from methylated porous silicon revealed that methyl (CH_3) groups orient with their molecular axis perpendicular to the walls of the porous silicon.

Application of the optical models described in chapter 3 allowed to determine the Lorentz oscillator parameters for nitrobenzene thin films. For this purpose, analysis of several test samples with different nitrobenzene layer thicknesses was performed. Since the thickness and the optical parameters of materials are interdependent, cross–referenced studies with XPS and VIS–ellipsometry were carried out for the determination of the thickness and high–frequency refractive index. A good agreement was obtained between the measured spectra from the nitrobenzene–modified Au and Si(111) substrates and the simulated results which used the Lorentz oscillator parameters as determined from the test samples with different nitrobenzene thicknesses.

The temperature–induced desorption of nitrobenzene molecules from Au sur-

face is investigated using the IRSE technique. Observation of the diminishing of the NO_2-related absorption peaks amplitudes established that the desorption occurs around 170^0C.

The oxidation of the interface between silicon and organic thin films was also observed. This will be discussed in chapter 6.

This chapter is structured as follows: first, we show the IR spectra of the aryl diazonium compounds prior to the electrochemical grafting. Then, a detailed studies of the Au, Si(111) and TiO_2 surfaces modified with nitrobenzene molecules are presented. This is followed by the discussion of the methoxybenzene properties grafted on various substrates. Finally, studies on methylated porous silicon are introduced. A discussion of the molecular attachment on silicon surfaces through the Si–C or Si–O–C bonds concludes this chapter.

5.1 IR properties of tetrafluorborate aryldiazonium compounds

IR spectroscopy of the 4–methoxybenzenediazonium tetrafluorborate (4–MeBDT) and 4–nitrobenzenediazonium tetrafluorborate(4–NBDT) salts was performed for investigations of the absorption band structure of the compounds from which the molecules were grafted on various surfaces. In addition, these measurements allow to notice absorption peaks due to possible contaminations that may be present on the surface, for example, resulting from the BF_4^- anion or N_2 (diazonium) cation.

Fig. 5.1 shows transmittance spectra obtained from the 4–NBDT and 4–MeBDT pressed into a KBr tablet. Mixing a KBr powder with the solid of interest and preparing a tablet under high pressures is a well-known technique for transmission measurements in IR spectral range. KBr is transparent between 4000 cm^{-1} to 400 cm^{-1}, thus the vibrational absorption of the material of interest is not effected by its presence. However, care should be taken when using this technique due to a possibility of ion exchange between the KBr and the material which is to be analyzed. Spectra obtained from 4–NBDT and 4–MeBDT (Fig. 5.1) showed a broad peak between 900 and $1200cm^{-1}$, related to the BF_4^- vibrations [106, 107]. Characteristic bands that are common to 4–NBDT and nitrobenzene and to 4–MeBDT and methoxybenzene molecules, respectively, are listed in table 5.1. However, the presence of the diazonium group shifts strongly the frequencies that would be expected for nitrobenzene (NB) and methoxybenzene (MeB). Thus the assignment in Table 5.1 was given only for absorption bands for which the direct comparison to the NB and MeB literature–listed frequency values was possible. Other characteristic absorption peaks were due to diazonium ν(N≡N) and $\nu(\text{Aryl-N})_{diazo}$ vibrations around 2200-2300 cm^{-1} (marked with * in Fig. 5.1) and 1300-1350 cm^{-1} (marked with ** in Fig. 5.1), respectively. Table 5.1 lists the measured absorption frequencies which are in agreement with those found in literature [103, 104, 105].

It is interesting to note the relative shift observed in frequencies between

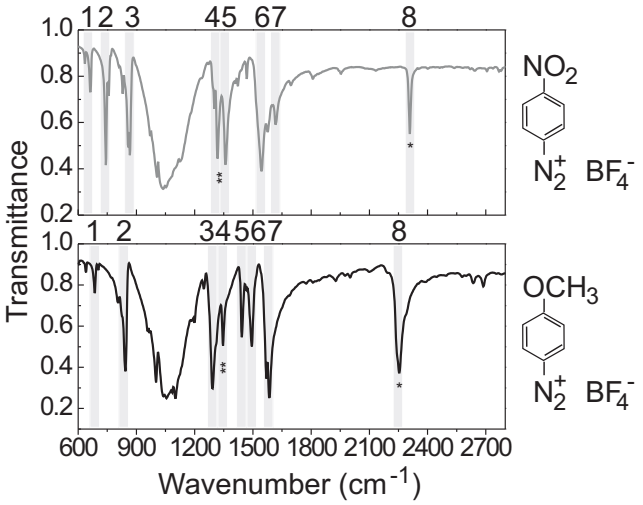

Figure 5.1: Transmittance spectra of 4–NBDT (gray) and 4–MeBDT (black) in KBr tablet. The diazonium–related absorption bands are marked by stars and are discussed in the text. The prominent bands 1–8 for each of the above compounds are listed in Table 5.1.

Band No. Fig. 5.1	4-NBDT cm^{-1}	Assignment [101]	4-MeBDT cm^{-1}	Assignment [102]
1	664	-	684	-
2	742	-	842	-
3	866	-	1292	(1292) δ(C–H)
4	1316**	ν(Aryl-N)$_{diazo}$	1346**	ν(Aryl-N)$_{diazo}$
5	1360	(1347) $\nu_{ss}(NO_2)$	1442	(1442) $\delta_s(CH_3)$
6	1545	(1523) $\nu_{as}(NO_2)$	1494	(1497) ν(C-C)
7	1618	-	1585	(1588) ν(C-C)
8	2306*	ν(N≡N)	2254*	ν(N≡N)

Table 5.1: The observed frequencies for 4-NBDT and 4-MeBDT in KBr pellet and the assignments of the major bands as labeled in Fig. 5.1. No assignment was performed in the spectral range between 900 and 1300 cm^{-1} due to the overlap with the strong bands associated with the BF_4^- absorption. Only the bands for which there is a clear comparison with nitrobenzene and metoxybenzene spectra in refs. [101] and [102] were assigned. The frequencies in the parentheses refer to the values determined from the literature. The starred frequencies refer to the diazonium–related absorption bands which were assigned in accordance to refs. [103, 104, 105]

the ν(N≡N) and $\nu(\text{Aryl-N})_{diazo}$ in OCH_3 and NO_2 p-substituted aryldiazonium compounds. Accordingly to refs. [108, 104, 105], bond order (the number of bonds between a pair of atoms) changes upon attachment of the organic group at the para-position of the benzenediazonium, as is schematically shown in Fig. 5.2. In general, it was found that electron donor substituents reduce the diazonium frequency, whereas acceptor substituents increase it (relatively to X=H in Fig. 5.2) [108, 104]. For electron acceptor sustituents (i. e. X=OCH_3), structure II in Fig. 5.2 becomes more dominant. There is a decrease of the N≡N bond order which shifts the absorption peak frequency due to the diazonium to lower wavenumbers [104, 105, 109]. In the following sections, investigations of

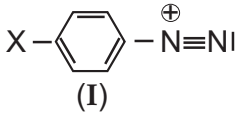

(I)

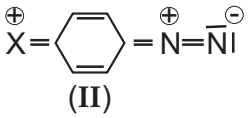

(II)

Figure 5.2: Structure of aryldiazonium upon substitution of different X groups [108, 104]. (I):Ground state; (II):Increasing the contribution of polarized structure upon substitution of electron-donating group.

electrochemically grafted organic films on various substrates will be discussed. However, no contaminations from the diazonium or BF_4^- anions from the benzenediazonium salts were detected with infrared ellipsometry. The absence of the BF_4^- contaminations was also confirmed by XPS, where no indicative fluorine F1s emission was found [4].

However, contaminations due to the wet-chemical etching could be sometimes observed on the organically modified surfaces. The wet-chemical etching of chemically prepared oxides on Si(111) surfaces is the final step to prepare flat and well H-passivated Si(111) surfaces with terrace-like structures and mono-atomic steps [39, 50, 110]. The final etching step in 40% NH_4F produces atomically flat surfaces [39]. However, sometimes the residual NH_4^+ ions were still present on the surfaces. Accordingly to the work of Yota and Burrows [111], these contaminations are the traces of the ammonium silicon fluoride ($(NH_4)_2SiF_6$) which is formed during the etching in the buffereded hydrofluoric acid [111]. Since such contaminants are soluble in water, rinsing of the samples in general removes their traces from the surface. Nonetheless, some of our IR spectra contained the absoprtion bands due to the NH_4^+ contaminations, as can be seen in (Fig. 5.3). During our IRSE spectral interpretation extra care was thus taken in the discussion of the absorption bands in this spectral range.

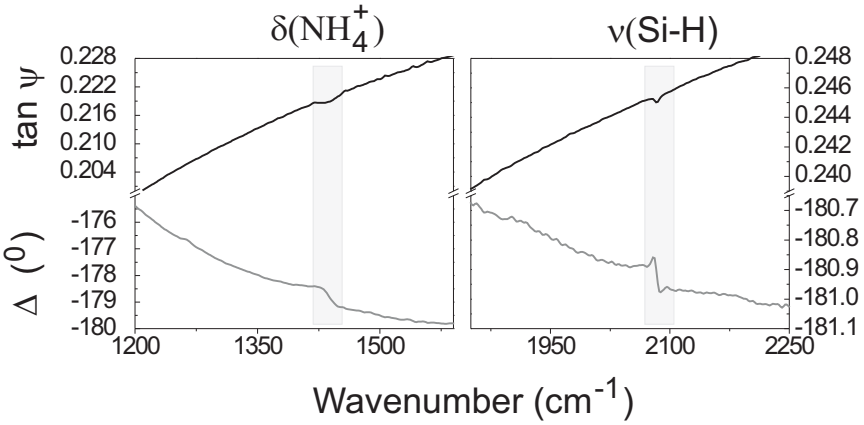

Figure 5.3: IRSE $\tan\psi$ (black) and Δ (gray) spectra obtained from n-type Si(111) surface, prepared by a standard procedure [112]. On the left-side panel, a typical absorption peak due to NH_4^+ contaminations is observed, while on the right-hand side, a Si-H absorption feature reveals that the H-termination was successful.

5.2 Nitrobenzene on Au, Si(111) and TiO_2 surfaces

In this section, the characterization work on nitrobenzene molecules electrochemically grafted on Si(111), Au and TiO_2 surfaces is introduced. The simulations in optical models for interpretation of IRSE results and for determination of the Lorentz oscillator parameters are discussed. The experiments on the stability of the nitrobenzene films to high temperature conditions are presented, where the temperature–induced desorption was monitored by IRSE. Eventually, we present our studies on the chemical composition of the electrochemically grafted NB films using XPS technique.

5.2.1 IRSE characterization of nitrobenzene films

For all surfaces which were modified with nitrobenzene thin films, IRSE spectra exhibited absorption bands due to symmetric and anti–symmetric stretching vibrations of the NO_2 group, as can be seen in Fig. 5.4 (a). Fig. 5.4 (b) shows the comparative plot between the spectra obtained from different surfaces in the extended spectral range. This plot shows the relative amplitudes of the observed vibrational bands on TiO_2, Au and Si(111) surfaces. Fig. 5.4 (c) shows SEM images of the TiO_2 surface before and after the modification with the nitrobenzene layers and it will be discussed later in this section.

The assignment of the absorption bands that were observed in Fig. 5.4 was based on the data provided in refs. [101,113,114] and is summarized in Table 5.2.

Liquid NB [101, 114]	NB on TiO_2 this work	NB on p-Si(111) this work	NB on Au this work	Assignment [101, 113, 114]
1021	1014	-	-	δ(C-H)
1108	1110	-	-	ν(C–N)+ring breathing
1174	1180	-	-	C-H bend
1347	1351	1353	1354	$\nu_{ss}(NO_2)$
1523	1525	1531	1527	$\nu_{as}(NO_2)$
1606	1598	1600	1598	$\nu(C–C)_{ring}$

Table 5.2: Observed frequencies for nitrobezene in (cm^{-1}) and assignments. The NB frequencies on TiO_2, Au and p-Si(111) were obtained in this work as shown in the spectra in Fig. 5.4 (a,b). ν_{ss} symmetric stretching vibration; ν_{as} asymmetric stretching vibration; δ bending vibration.

For a detailed spectral analysis and conclusions on molecular orientation, simulations in optical models are necessary. Fig. 5.5 shows the calculated line shapes for different possible orientations of the nitrobenzene on Si and Au surfaces.

For metallic surfaces, the line shapes follow the surface selection rules [115]. These rules allow only absorption of incident IR radiation by vibrational modes whose transition dipole moment components are perpendicular to the surface plane. Fig. 5.6 shows the orientation of the transition dipole moment for the symmetric ($\nu_{ss}(NO_2)$) and antisymmetric ($\nu_{as}(NO_2)$) stretching vibrations of the NO_2 group of nitrobenzene. Orientation of the molecules with the molecular plane parallel to the Au surface would result in absence of the absorption bands due to both the symmetric and antisymmetric vibrations of the NO_2 group (Fig. 5.5). If the molecular plane would be perpendicular to the Au surface (molecules would be upright–standing), the $\nu_{ss}(NO_2)$ mode would give a transition dipole moment perpendicular to the Au surface while the $\nu_{as}(NO_2)$ would result in a transition dipole moment oriented parallel to the Au surface. In this case, only absorption bands due to $\nu_{ss}(NO_2)$ should appear in our spectra. However, the results of the measurements presented in Fig. 5.4 (a) show a situation with the line shapes corresponding to a random orientation as shown through the simulations of the spectra in Fig. 5.5.

Another important result coming out of calculations presented in Fig. 5.5(b) is the relative band amplitude of the absorption bands of the molecules grafted on Au and Si substrates. For upright–standing molecules, Fig. 5.5 shows that the absorption band due to the symmetric NO_2 vibrations on Au is twice the amplitude of this band on Si substrate. This is due to the image–charge effect of the transition dipole moment on metallic surfaces. It is also interesting to compare the above-discussed spectra from NB/Si and NB/Au surfaces to the NB/TiO_2 case. From a comparative plot shown in Fig. 5.4 (b), it is evident that nitrobenzene films on TiO_2 surface have stronger absorption features, resulting

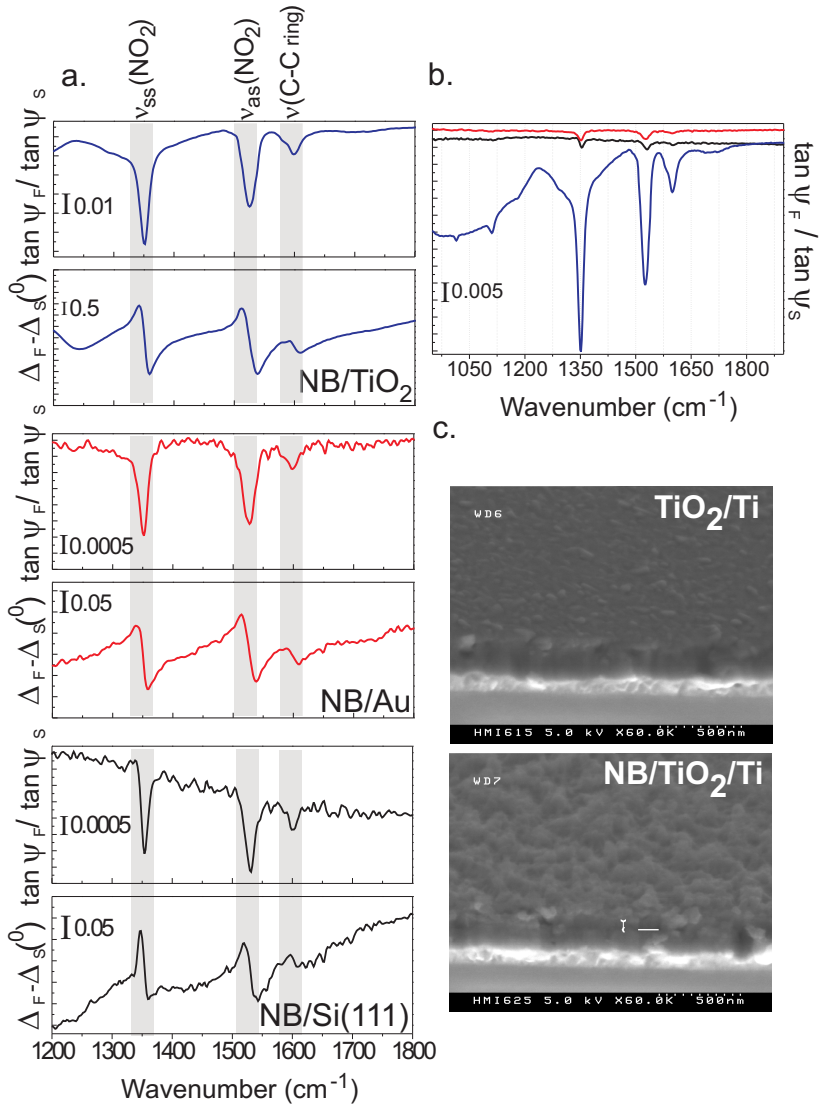

Figure 5.4: a. Referenced IRSE spectra of tanψ_F of the nitrobenzene film to tanψ_S of various bare substrates in the range between 1200 cm^{-1} and 1800 cm^{-1}. b. Referenced tan ψ spectra plotted on the same scale in the extended spectral range. tan ψ spectrum for NB on Si (111) was shifted by 0.002 for clarity. Black: NB on p-Si(111); red: NB on Au; blue: NB on TiO_2. c. SEM micrographs of a non-modified TiO_2 on Ti-coated glass substrate (upper SEM panel) and surface modified with NB molecules (lower SEM panel). The white lines serve as guide to the eye and indicate the NB layer. The SEM images were taken at a tilt angle of 30^0.

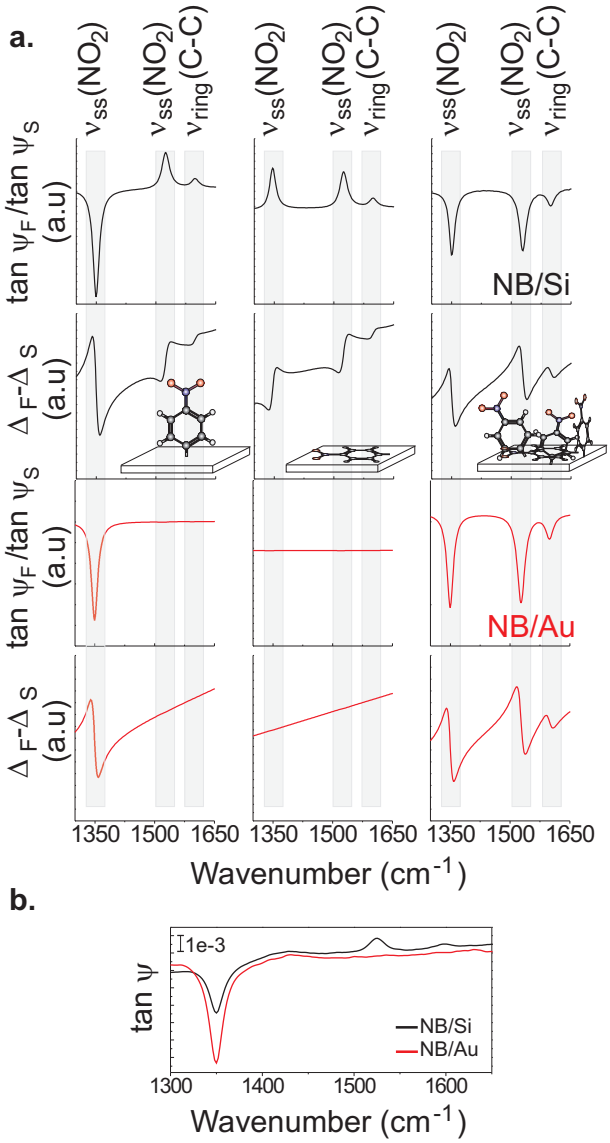

Figure 5.5: a. Calculated ellipsometric line shapes for Au (red) and Si(black) NB–modified surfaces, referenced to bare substrates (arbitrary scaled). Molecular orientation of NB molecules is shown schematically on the insets, where the left column refers to upright–standing molecules, central to the molecular plane parallel to the surface and the right column shows the molecules randomly oriented on a substrate. b. tan ψ spectrum comparing the amplitudes for a 10 nm calculated film with high-frequency refractive index of 1.46. The data from measured substrates was employed in all calculations.

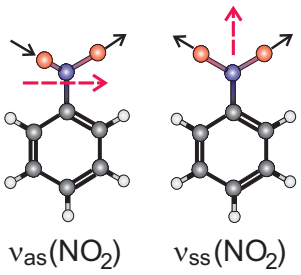

Figure 5.6: Molecular transition dipole moment (symbolized by red arrows) for symmetric ($\nu_{ss}(NO_2)$) and antisymmetric ($\nu_{as}(NO_2)$) stretching vibrations of the NO_2 group of nitrobenzene.

from a higher thickness of the layer. This finding is supported by SEM images of organically modified TiO_2 surface (Fig. 5.4 (c)), where a thickness of about 70 -100 nm of NB is observed. VIS– ellipsometry indicated the thickness of 100 nm and a high-frequency effective refractive index of 1.3. The relatively low value of the effective refractive index is a result of a less dense layer. Here, high thickness of the films suggests occurrence of polymerization upon electrochemical grafting. In general, polymerization can occur through the radical position at the aryl ring, as shown in Fig. 5.7 (a). The other possibility proposed by Laforgue et al [116] is the involvement of diazonium group in a polymerization or even in an attachment to a surface (Fig. 5.7 (b)). However, we did not detect any absorption due to a diazonium group in our IRSE spectra for none of the studied molecules. Thus the most likely scenario is the polymerization through the process shown in Fig. 5.7 (a).

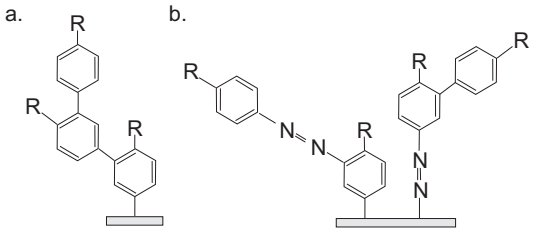

Figure 5.7: Polymerization of benzene derivatives upon electrochemical grafting after [116]. a. Polymerization through radical end at the aryl ring; b. Possible involvement of diazonium in formation of electrochemically grafted thin films

5.2.2 Determination of optical constants

The aim of this section is the determination of the Lorentz oscillator parameters for nitrobenzene thin films in the infrared spectral range. This was done through

cross–reference of the IRSE data from NB films with several thicknesses on Si and Au substrates. We verified our calculations using complementary methods, such as Vis–ellipsometry and XPS.

In order to calculate NB optical properties in the IR spectral range, films with several thicknesses were prepared. As was already mentioned earlier (see section 2.2.1) grafting of nitrobenzene films from aryl diazonium compounds on H-passivated Si(111) surface is a self-limiting process. Thus for preparation of a thick nitrobenzene film, the electrode potential was driven to -4 V. This enabled an electron transfer through the already formed NB blocking layer by means of tunneling. We denote this sample "S1" for further discussion. The other films were taken out of the electrolyte after grafting within 110 sec and 550 sec, respectively. We denote the sample prepared withing 550 sec of grafting "S2" and the 110 sec "S3".

Samples S1 and S3 were measured by VIS–ellipsometry, resulting in high-frequency refractive index of 1.46. The thickness of S1 was 125 nm while that of S2 was 14 nm. Sample S3 was measured with soft X–rays using X-rays standing waves which monitors a characteristic atomic X-ray fluorescence signal [117] at the plane-grating monochromator (PGM) beamline for undulator radiation [118, 119] at the Physikalisch-Technische Bundesanstalt (PTB) at BESSY II. Evaluation of carbon fluorescence emission resulted in 3 nm thickness of the NB film in the S3 sample [120].

Using the above data, IRSE spectra from the three samples were fitted using Lorentz–oscillator formalism in isotropic layer model. The results are shown in Fig. 5.8. Oscillator parameters are summarized in Table 5.3.

Assignment	Frequency ω_0 (cm^{-1})	F (cm^{-2})	Γ (cm^{-1})
sym. NO_2 stretch	1346	21207	19
asym. NO_2 stretch	1524	22748	23
Ring stretch	1598	5404	23

Table 5.3: Parameters of NB on Si(111) surface as fitted using Lorentz-Oscillator model. The simulated results are shown in Fig. 5.8

We observed a good agreement between the Lorentz oscillator constants of the NO_2 group–related absorption bands from 2–[4–(N–Dodecanoyl amino) phenyl]–5–(4–nitrophenyl)–1,3,4–oxadiazole Langmuir–Blodgett (LB) films on gold as obtained in Ref. [121] and the Lorentz oscillator constants for the NB films in this work as shown in Table 5.3. The approach that was used in ref. [121] for the determination of NB optical constants through the scaling of the optical constants from the LB films with the known thickness and a determined high–frequency dielectric constants has some disadvantages. Namely, the chemical environment of the nitrobenzene unit in the above LB film may have an influence on the absorption band shapes in IRSE spectra, resulting in overestimated or underestimated Lorentz oscillator parameters. The current approach as described above bases uniquely on studies of NB films, where we combined the data from different experimental methods and cross–referenced the results

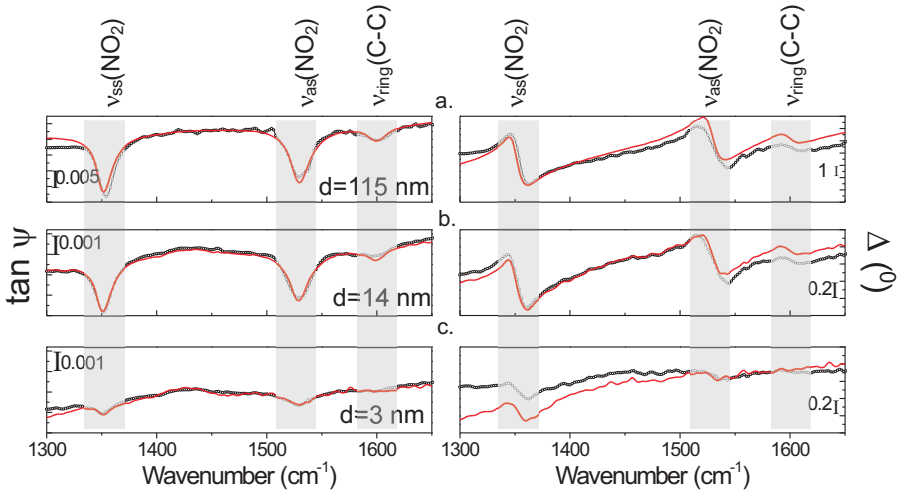

Figure 5.8: Measured (black) and calculated (red) spectra for three different nitrobenzene films on Si(111) substrates with d=115 nm(a); d=14 nm (b); and d=3 nm (c) thicknesses. Left: ellipsometric parameter tan ψ, right: the corresponding Δ spectra. Calculations were performed using high–frequency refractive index n_∞=1.46 and thickness as denoted in the plots. Lorentz oscillator parameters are given in Table 5.3

from NB films with different thicknesses. Using the oscillator parameters listed in Table 5.3, a good agreement was achieved between the measured and the calculated lineshapes for NB on metallic Au surface, as shown in Fig. 5.9. The results obtained from the simulations of NB films on Au and Si substrate point out that the molecules have an isotropic distribution on these substrates. This supports our earlier driven conclusion from comparison of the lineshapes as obtained from TiO_2, Si(111) and Au surfaces that the nitrobenzene does not have any preferential orientation in the grafted films.

5.2.3 Thickness determination and studies of the chemical composition of nitrobenzene films using combined XPS and IRSE analysis

To investigate the chemical composition of the nitrobenzene films on Si(111) and to cross-reference their thickness values, X-ray photoelectron spectroscopy (XPS) was employed as a complementary method to IRSE. The deconvolution of the core level spectra will be performed and discussed in detail in chapter 7. Here, we shortly present the relevant core–level information for determination of composition and thickness of the grafted NB films on Si(111) surface.

Fig. 5.10 (a) shows the Si2p, N1s, O1s and C1s core level spectra obtained

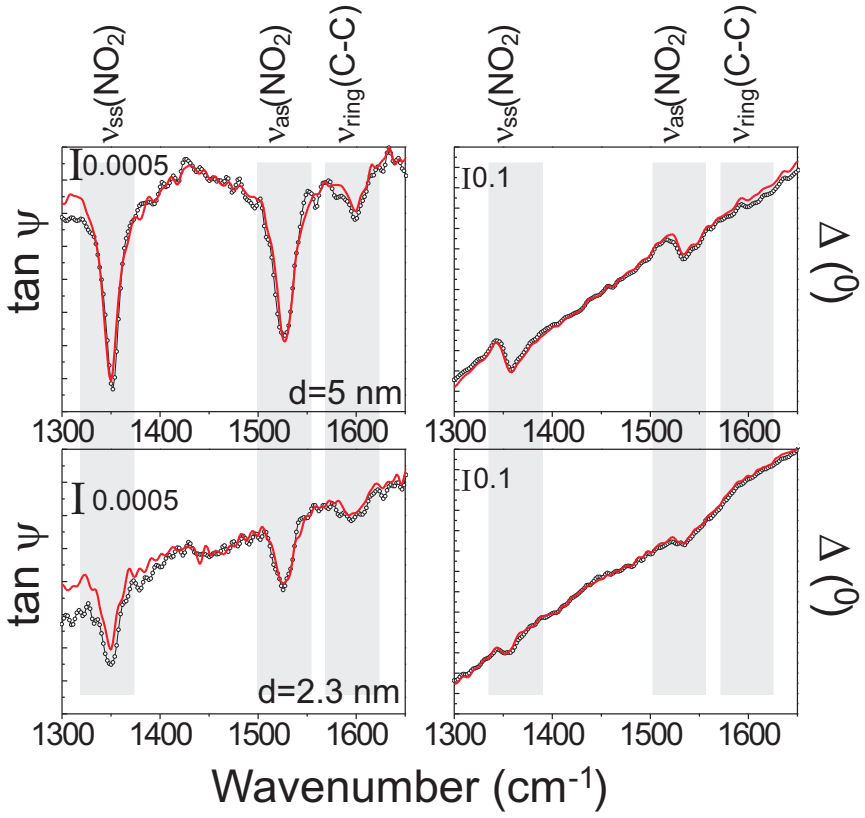

Figure 5.9: Measured (black) and calculated (red) spectra for two different nitrobenzene films on Au substrates. Left: tan ψ, right: the corresponding Δ spectra. The calculation was performed using high-frequency refractive index n_∞=1.46 and thickness as denoted in the plots. Lorentz oscillator parameters are given in Table 5.3

at 650 eV incident energy. The ratio of the integrated intensities should be indicative of the relative atomic composition of the film. Integrating the core–level spectra from Fig. 5.10, we obtain the C1s integrated intensity of 5310, the N1s integrated intensity of 1280 and the O1s of 3870. The nitrobenzene chemical formula $C_6H_5NO_2$ presumes the relative atomic composition of 6(C):1(N):2(O), while the above integrated intensities suggest the film composition of 4(C):1(N):3(O). However, it is readily observable that the N1s spectrum consists of two different peaks, positioned at 406 eV and 400 eV. While the peak at 406 eV results from the nitrogen atom bonded to oxygen in NO_2 groups, the peak at 400 eV results from nitrogen bonded to hydrogen in amino (NH_2) groups. Such amino-type contribution result mainly from the amino compounds that serve as the precursors for the aryl diazonium salts from which the nitrobenzene was electrochemically grafted onto the surface [122]. Ignoring this peak and integrating only the signal from lower binding energies, the integrated intensity of N1s was 875. This is in good agreement with the expected C:N (6:1) ratio.

For O1s core-level spectrum, the situation is much more complicated. It will be shown in chapter 7 that the O1s signal includes contributions from interfacial oxygen in SiO_x centered at 531.4 eV. Ignoring this peak, the integration over the rest of the O1s peak results however in integrated intensity of 3400, thus the ratio of the corrected integrated intensities for C:N:O is 6:1:4. This relation still does not correspond to the molecular formula of nitrobenzene. However, according to Refs. [123,124,125], also the water–related O1s signal is centered at 533 eV, similarly to the signal from the oxygen in NO_2 groups. This explains the high oxygen ratio relatively to the nitrogen and the carbon–related contributions as obtained from integrated intensities of the respective core–level peaks. Due to the spectral overlap, it was not possible to distinguish between the O1s signal coming from the remnant water in the electrolyte and from the nitrobenzene film.

Comparison between the XPS and IRSE spectra presented in Fig. 5.10 reveals a SiO_x–related peak in the Si2p core level of the XPS spectra, while no band in the IRSE spectra corresponding to the SiO_x absorption in the range between 1000 to 1200 cm^{-1} was observed. The reason might be that (a) the two different pieces of the sample that were analyzed by XPS and IRSE were differently oxidized; (b) the above discussed water residuals from the electrochemical grafting were triggered by X–ray irradiation to oxidize the silicon interface; (c) oxygen atoms which are released upon the reduction of the nitrobenzene to aniline upon X–ray irradiation contributed to oxidation of the silicon surface (see chapter 7 for the detail discussion of this reduction process) and (d) different sensitivity of the IRSE and XPS to the amount of the surface silicon oxides. The detailed discussion of the amount of the SiO_x as calculated from the combined XPS and IRSE measurements will be presented in section 6.3.

The measurements shown in Fig. 5.10 were used for the determination of the nitrobenzene thickness. Simulations of the IRSE spectra are shown in red in Fig. 5.10(b), in which the Lorentz oscillator parameters determined in the previous section were used (see Table 5.3). The simulation resulted in 5 nm

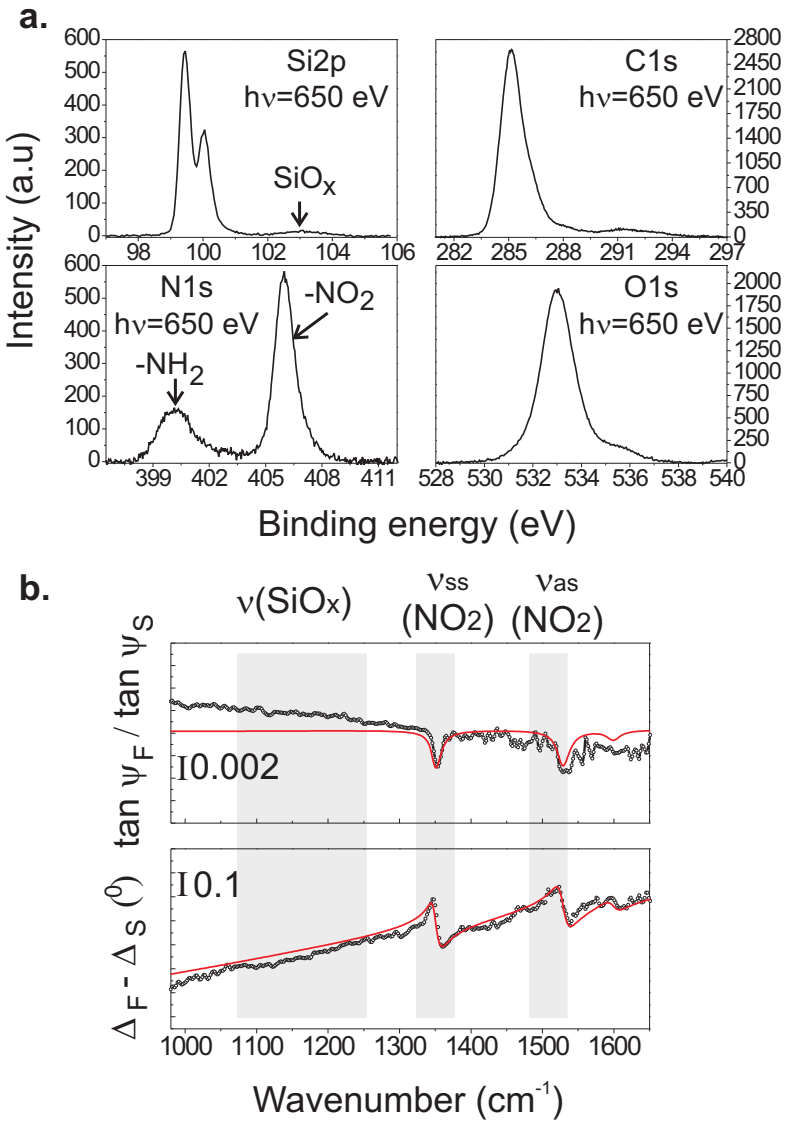

Figure 5.10: a. Si2p, C1s, N1s and O1s core level spectra obtained from the nitrobenzene–terminated Si(111) sample, at hν=650 eV photon energy. Deconvolution of all of the above core level spectra is be presented in detail in chapter 7. b. IRSE spectra obtained from the other part of the same sample, where the measured spectra are shown in black and the simulated in red. Simulations were performed using n_∞=1.46, thickness d=5 nm and Lorentz oscillator parameters as shown in Table 5.3.

nitrobenzene layer thickness. For estimation of nitrobenzene film thickness using the XPS spectra, Eq. 4.14 from section 4.2.2 was used. The Si2p integrated intensity from the nitrobenzene–coated Si(111) surface was 445 at 650 eV, while for bare Si(111), the integrated intensity was 9400. The calculations were performed using Eq. 4.14, which expresses the attenuation of the Si2p core level signal by the nitrobenzene layer. The data for inelastic mean free path is unfortunately currently absent from databases. Data for several organic materials was published by Tanuma, Powell and Penn in ref. [99]. The data diverges from 1.86 nm for Guanine to 2.4 nm for polymethylmethacrylate (PMMA) at 650 eV. We take the λ_l value to be 2.27 nm, typical for polyethylene and polysterene. Thus, the thickness of the nitrobenzene is estimated to be around 7 nm. The simulations of IRSE data from the same sample results in 5 nm thickness. The discrepancy is the result of (a) ignoring the interface SiO_x layer and (b) the uncertainty in the IMFP values. However, calculations based on the XMQ analysis (see section 4.2.2) take into account the interfacial SiO_x layer. Such calculations result in the NB thickness of 5 nm, in a good agreement with IRSE results. The detailed discussion of the determination of the nitrobenzene layer thickness in a model which takes into account the SiO_x interfacial layer thickness and coverage will be presented in chapter 6.

5.2.4 IRSE studies of temperature–induced desorption

The temperature stability studies of nitrobenzene organic layers on Si(111) surfaces were reported in [126], where temperature–induced desorption was monitored with mass spectrometer. The desorption was reported to start above 190^0C, with the desorption of NO and of C_2HNO_2 above 200^0C.

In this work we performed IRSE temperature–dependent measurements of NB on Au surfaces under UHV conditions. Fig. 5.11 shows the results of the measurements, where plot (a) shows high–resolution spectra (1 cm^{-1}), plot (b) shows evolution of spectra obtained with resolution of 4 cm^{-1} and plot (c) shows the integrated intensities of absorption peaks due to NO_2 symmetric stretching vibration (1), NO_2 asymmetric stretching vibration (2) and of the ring C–C stretching vibration (3) as a function of the temperature.

The cryogenic temperatures were employed in order to find out whether the cooling can influence the ordering of the molecules on the surface. However, as can be seen in high–resolution spectra in Fig. 5.11 (a), no differences were found between the absorption peaks in the spectra of NB/Au at -160^0C and the absorption peaks in the spectra obtained after the heating of the sample up to 60^0C. The desorption starts around 170^0C, with the diminishing of the amplitudes of the $\nu(NO_2)$ vibrations. However, the absorption peak due to ν(C-C)$_{ring}$ stays nearly constant through the treatment. Above 250^0C, only the intensity due to the symmetric $\nu(NO_2)$ vibration is still possible to evaluate, while the other absorption peaks diminish in amplitude and overlap with the atmospheric water absorption bands. The diminishing of the amplitudes of the absorption bands due to $\nu(NO_2)$ vibrations is in agreement with the desorption of the NO units as reported in ref. [126]. However, the ν(C-C)$_{ring}$ has almost

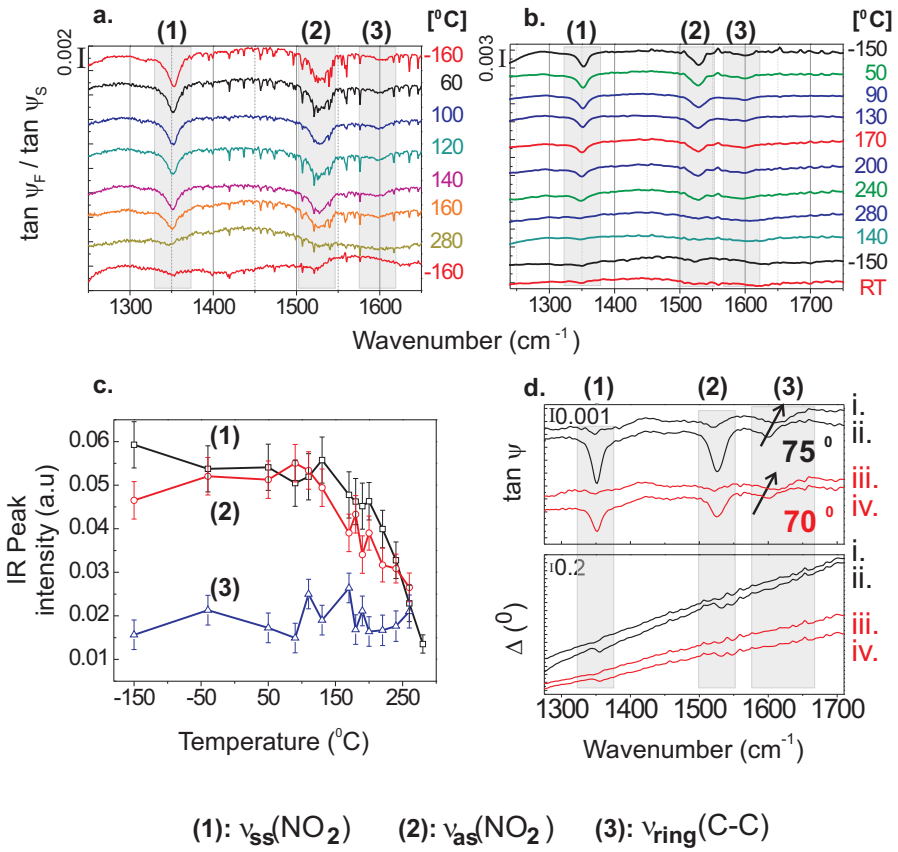

Figure 5.11: Temperature–dependent IRSE spectra obtained from NB/Au surface. a. Spectra obtained with the resolution of 1 cm^{-1}; b. Spectra with resolution of 4 cm^{-1}; c. Integrated intensity of $\nu_{ss}(NO_2)$ (1), $\nu_{as}(NO_2)$ (2) and $\nu(C\text{-}C)_{ring}$ (3) absorption peaks. d. Zoomed–in IRSE spectra before the temperature–dependent desorption experiment (ii,iv) and after it (i,iii), obtained at incident angles of 75^0 (black) and 70^0 (red). The arrows emphasize the shift of the $\nu(C–C)_{ring}$ absorption peak to higher frequencies upon sample heating.

constant amplitude throughout the experiment.

Fig. 5.11 (d) shows IRSE spectra obtained from the surface directly after electrochemical preparation (ii,iv) and after temperature–dependent desorption (i,iii), at 75^0 and 70^0 angle of incidence. In this figure, a shift of about 20 cm^{-1} from 1600 cm^{-1} toward higher frequencies is observed for $\nu(C–C)_{ring}$ after thermal treatment of the sample. Also the absorption bands due to the residual NO_2 bonds can be still observed. These results indicate that the substantial changes occur in the environment of the phenyl ring of the nitrobenzene, but that the residual organic material stays on the surface. On the unheated surface, the initial amplitudes of the bands due to the νNO_2 stretching vibrations are about three to four times higher in comparison to the band due to the $\nu(C–C)_{ring}$ stretching vibrations which appears at 1600 cm^{-1}. However, after the thermal desorption, the bands due to the $\nu(NO_2)$ and the $\nu(C–C)_{ring}$ exhibit comparable amplitudes. The shift of the band initially positioned at 1600 cm^{-1} to higher frequency by 20 cm^{-1} can be due to the absorption by a $\nu(C{=}C)$ vibrational mode in alkenes [127]. This is then in agreement with earlier work [126] where the detection with mass spectrometry indicated the decomposition of nitrobenzene into C_2H_2, C_2HNO_2 and NO_2 fragments at temperatures above 200^0C.

5.3 Methoxybenzene on Au, Si(111) and TiO_2 surfaces

Spectra obtained after the grafting of MeB (methoxybenzene) films on TiO_2/Ti, Au and Si(111) surfaces are shown in Fig. 5.12. The bands marked in Fig 5.12 can be attributed to the vibrational modes of MeB molecules [102, 128] and are identified in the spectra for each of the three substrates. The band around 1178 cm^{-1} arises from rocking vibrations of CH_3 groups [102]. The band around 1250 cm^{-1} is attributed to C-OCH_3 stretching vibrations. Bands at 1515 cm^{-1} and 1610 cm^{-1} probably arise due to the ring C–C stretching vibrations [102, 128]. Another characteristic vibration for MeB around 1030 cm^{-1} is attributed to O-CH_3 stretching vibrations [102, 128]. This band appears in spectra obtained from TiO_2/Ti and Au surfaces, but is not distinguishable on a spectrum obtained from the MeB/Si(111) surface. On Si surfaces, the range between 1050 cm^{-1} and 1250 cm^{-1} is the range of the absorption bands due to the stretching vibrations of silicon oxides [129] and the MeB vibrational modes may be overlapping with those from the SiO_x contributions from the substrate. The absorption signal around 1440 cm^{-1}, which appears as peak-up feature in the spectrum obtained from the Si surface is most likely due to residual NH_4^+ ions on the surface, as was pointed out in section 5.1 [111, 130]. This band was present on the hydrogen passivated Si surface which was used for referencing the spectrum and is the result of the pretreatment of Si. Additionally, the MeB – related band intensities from Au and Si surfaces were of similar magnitudes, while the MeB – related bands obtained from the TiO_2/Ti surface were of much

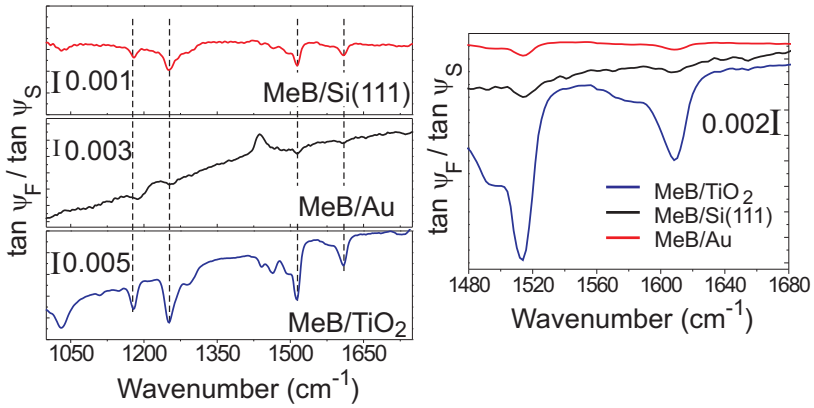

Figure 5.12: Left: tan ψ spectra obtained from MeB on TiO_2, Au and Si(111) surfaces; right: comparative figure for absorption band intensities of MeB on the different surfaces in a spectral range between 1480 cm^{-1} and 1680 cm^{-1}.

stronger intensities.

Measurements performed by VIS-ellipsometry indicated a thickness of 55 nm and a refractive index of 1.33 for MeB on TiO_2/Ti, while thicknesses of 4 nm and 3 nm, and a refractive index of 1.46 were obtained for Au and Si surfaces, respectively. The differences in refractive indices in thinner and thicker films could be due to a different molecular structure and density in these films. Similar to the nitrobenzene film on a TiO_2/Ti surface in the previous section, a higher grafted thickness on the TiO_2/Ti surface could be due to a non self-limiting process that was observed earlier for grafting of NB onto oxidized Si surface [2]. This difference in thicknesses is the main reason for different band amplitudes that were observed for various substrates in the IR spectra in Fig. 5.12. For discussion of the orientation of methoxybenzene on Au surface, we apply surface–selection rules in a similar way as it was done in section 5.2 for nitrobenzene. Bands due to stretching vibrations of C-OCH_3 and O-CH_3 were observed at 1250 cm^{-1} and 1030 cm^{-1}. For a thin film on a metallic substrate this is only possible if the corresponding transition dipole moments have a component in the direction of the surface normal. Assuming that the molecules have planar geometry and that the transition dipole moments of C-OCH_3 and O-CH_3 are lying in the molecular plane [102], the orientation of the molecular planes can not be parallel to the substrate surface. However, a non-planar geometry, as reported by Tan et al [131] for MeB on Pt surfaces could also be the reason for our observations. Therefore a clear assertion for the molecular orientation is not possible for this case.

A good agreement was found between the spectra of MeB on the Pt surface as obtained by Tan et al [131] and the spectra of MeB on TiO_2, Au and

Si(111) surfaces. Nonetheless, we observed certain differences in the band position of some of the vibrational bands: for instance, Tan et al [131] reported the phenyl-related stretching vibrations at 1603 cm^{-1}, 1587 cm^{-1}, 1500 cm^{-1} and 1441 cm^{-1} for MeB multilayers on Pt. For electrochemically grafted MeB on Au and on TiO_2, we observed these bands at 1608 cm^{-1}, 1575 cm^{-1}, 1513 cm^{-1} and 1463 cm^{-1}, respectively. These differences probably arise from different deposition methods that were employed in both cases. While Tan et al [131] used vacuum deposition, where the MeB molecules were dosed on the surface from the gas-phase, in this work the molecules were deposited electrochemically. The electrochemical deposition requires creation of radicals which changes the electronic [23] and the vibrational [132, 133] properties of molecules. Also the multilayer growth mechanism may differ from that under vacuum condition preparations, and may proceed through the polymerization of radicals [25]. All these differences may result in a shift of the absorption band positions of electrochemically grafted films relative to the frequencies observed in spectra of liquid-phase MeB [102] or films deposited from the gas–phase.

Fig. 5.13 shows a comparison between IRSE spectra of the silicon surface terminated with the MeB derivative, namely 4–methoxy–diphenyl–amine (4–MDA) and the IRSE spectra obtained from the MeB terminated surfaces. The methoxybenzene group is a composite of the both MeB and of the 4–MDA. Thus, IRSE spectra obtained from surfaces modified with these molecules have similar absorption features, as shown in Fig. 5.13. This figure presents a spectrum obtained from Si(111) surface modified with 4–MDA along with a spectrum of MeB on Au surface for comparison. The spectra from the MeB/Au were chosen for this comparison due to a better signal to noise ratio than was obtained for MeB/Si as was shown earlier in Fig. 5.12.

Absorption bands due to the $C_6H_5OCH_3$ are present in both 4–MeB and 4–MDA. Table 5.4 shows the assignment of the prominent absorption bands marked in Fig. 5.13. The wealth of absorption bands between 1040 cm^{-1} to 1100 $^{-1}$ as reported in Ref. [134] may overlap with SiO_x vibrational frequencies thus the assignment in this spectral range is not unequivocal. The bigger 4–MDA molecules need a greater volume than NB or MeB on a surface since it consists of two phenyl rings. Section 6.2 will show that this property plays an important role in a protection (passivation) of the Si substrate from oxidation.

5.4 Electrochemical grafting on porous silicon

Preparation of porous silicon (PSi) through electrochemical treatment in acidic fluoride solutions was mentioned in section 2.3. In this section the IR spectroscopic properties of hydrogen passivated and of organically modified PSi is presented. Specifically, the organic modification will include the nitrobenzene ($C_6H_5NO_2$) and methyl (CH_3) termination.

Fig. 5.14 shows the SEM micrograph obtained from the PSi surface. According to refs. [41, 42, 43, 44, 45], the pores in the silicon surface are formed as walls which are perpendicular to the Si surface plane. Fig. 5.15 schematically

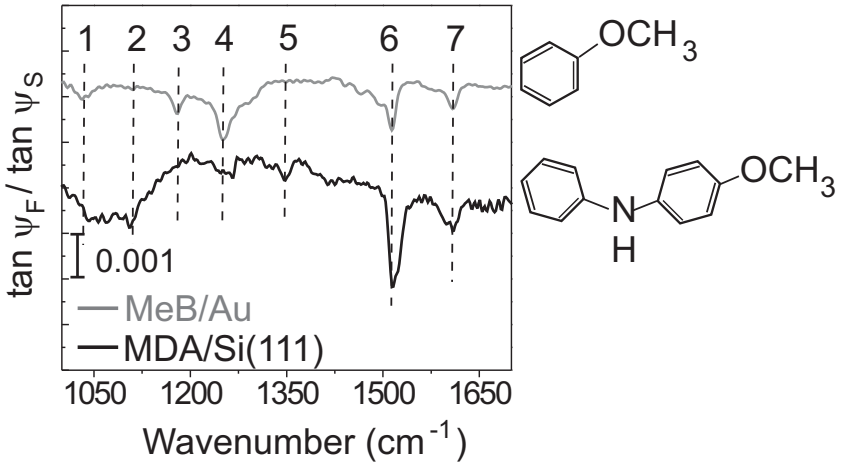

Figure 5.13: IRSE referenced tan ψ spectra of MeB/Au (upper spectrum) and 4–MDA on Si(111) (lower spectrum). Spectrum of MeB/Au is shown for comparison. The assignment of the marked bands is summarized in Table 5.4.

Band No. Fig. 5.13	4-MeB/Au cm^{-1}	Assignment [102, 131]	4-MDA/Si(111) cm^{-1}	Assignment [102, 131, 134]
1	1030	ν(O-CH_3)	not clear	ν(O-CH_3), ν(C-N)
2	1110	$\delta(C-H)$	1105	$\delta(C-H)$
3	1178	$\rho(CH_3)$	-	$\rho(CH_3)$
4	1250	ν(Ph-O)	1240-1267	ν(Ph-O)
5	-	-	1348	ν(C-N)
6	1515	ν(C-C)	1515	δ(N-H)
7	1610	ν(C-C)	1610	ν(C-C), δ(N-H)

Table 5.4: Observed frequencies for grafted 4–MeB and 4–MDA as shown comparatively in Fig. 5.13. ν–stretching, ρ–rocking, δ–bending vibrational modes as assigned on the basis of the references above. Absorption bands between 1040 cm^{-1} to 1100 cm^{-1} in Fig. 5.13 may overlap with SiO_x vibrational frequencies thus the assignment in this spectral range is not unequivocal.

shows orientation of the hydrogen and methyl (CH_3) on such walls in porous silicon and compares to the orientation on flat silicon surfaces. The support of the model shown in Fig. 5.15 is provided in the following, through the comparison of the line shapes of the IRSE spectra obtained from the porous and flat silicon surfaces. The next subsections are structured as follows: first, the

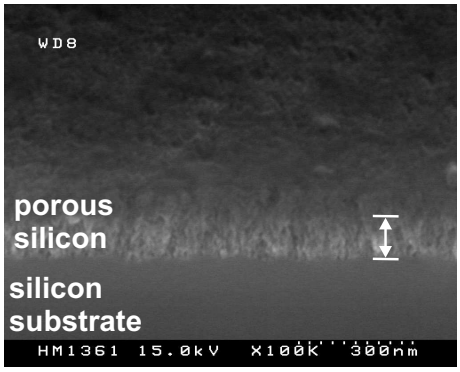

Figure 5.14: SEM micrograph obtained from the porous silicon surface.

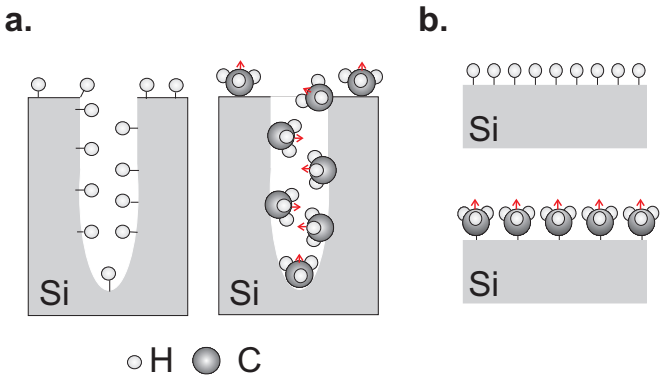

Figure 5.15: a. Schematic drawing of hydrogen (left) and CH_3 (right) orientation in the pores of the silicon. b. Schematic drawing of the molecules attached to the flat silicon surfaces. The molecular symmetry axis is indicated by red arrows for the CH_3 groups.

spectra obtained from the hydrogen passivated silicon surfaces are presented. The support to the model described in Fig. 5.15 is provided in accordance to the observations of the spectral line shapes. Next, IRSE results obtained from organically modified flat Si(111) surfaces will be compared to those obtained from PSi surfaces. Orientation of nitrobenzene ($C_6H_4NO_2$) and methyl (CH_3) grafted on porous silicon surfaces will be discussed.

5.4.1 IRSE characterization of PSi: comparative studies with Si(111) and Si(001)

In this section, IRSE spectra obtained from the flat Si(111) and Si(001) hydrogen passivated surfaces are compared to those obtained from porous silicon (PSi), as shown in Fig. 5.16. At lower frequencies, spectrum obtained from the PSi surface (Fig. 5.16 (a)) exhibits absorption peaks due to the bending vibrational modes as follows: at 636 cm^{-1} due to Si–H bending vibrations [135, 136, 137], at 669 cm^{-1} due to Si–H wagging vibrations [135,136], and at 906 cm^{-1} due to SiH_2 scissors mode [135, 136, 137]. At higher frequencies, absorption peaks due to stretching vibrations are observed: the mode at 2094 cm^{-1} is assigned to Si–H stretching vibrations [135,137], the mode at 2121 cm^{-1} is due to SiH_2 stretching vibrations [135, 137] and the absorption at 2140 cm^{-1} is due to SiH_3 stretching vibrations [135, 137]. The absorption peaks due to the Si–O_y–H_x molecular vibrations at 2200 cm^{-1} and around 2250 cm^{-1} [138] were not observed.

Fig. 5.16 (b) exhibits spectra obtained from Si(001) surface in the spectral range between 2000 and 2280 cm^{-1}. The absorption peak around 2110 cm^{-1} is assigned to dihydride stretching vibrations and the feature at 2140 cm^{-1} to tryhydride stretching vibrations [64]. The absorption peak due to the monohydride stretching vibrations is expected at 2080 cm^{-1}, it is however at the noise level of the obtained tan ψ and Δ spectra.

Fig. 5.16 (c) shows the spectra obtained from hydrogen–passivated Si(111) surface, which exhibit two sharp absorption peaks due to silicon monohydrides vibrational modes: at 2082 cm^{-1} the mode is due to Si–H stretching vibrations and at 626 cm^{-1} is due to the Si–H bending vibrations [135]. Comparison between the spectra in Fig. 5.16 reveals striking differences in band shapes. While the spectra obtained from the well-defined Si(111) surface exhibit a peak–up feature due to the absorption through the bending Si–H vibrations and a peak–down feature due to the absorption by the stretching Si–H vibrational mode, the spectra obtained from the PSi exhibit inverse features. Comparison between the IRSE spectra obtained from the PSi and Si(001) reveals the peaks positioned at the same frequencies due to the dihydride and trihydride stretching vibrations in the spectral range between 2000–2200 cm^{-1}, which however have different line shapes.

In section 3.4 we showed that the peak–up features on H/Si(111) surfaces arise due to the absorption through the molecular vibrations with transition dipole moment parallel to the surface plane. On the other hand, peak–down features arise due to the absorption through the molecular vibrations with transition dipole moment perpendicular to the surface plane (see Fig. 3.8 in section 3.4). The inverted peak shape for the PSi suggests that the transition dipole moments have inverse features in PSi as compared to the flat silicon surfaces, with respect to the radiation plane of incidence.

These observations support the earlier presented model as shown in Fig. 5.15. The lineshapes differences can be understood when orientation of the transition dipole moment relatively to the surface plane are taken into account. The pores in the silicon surface were formed as walls which are perpendicular to the Si

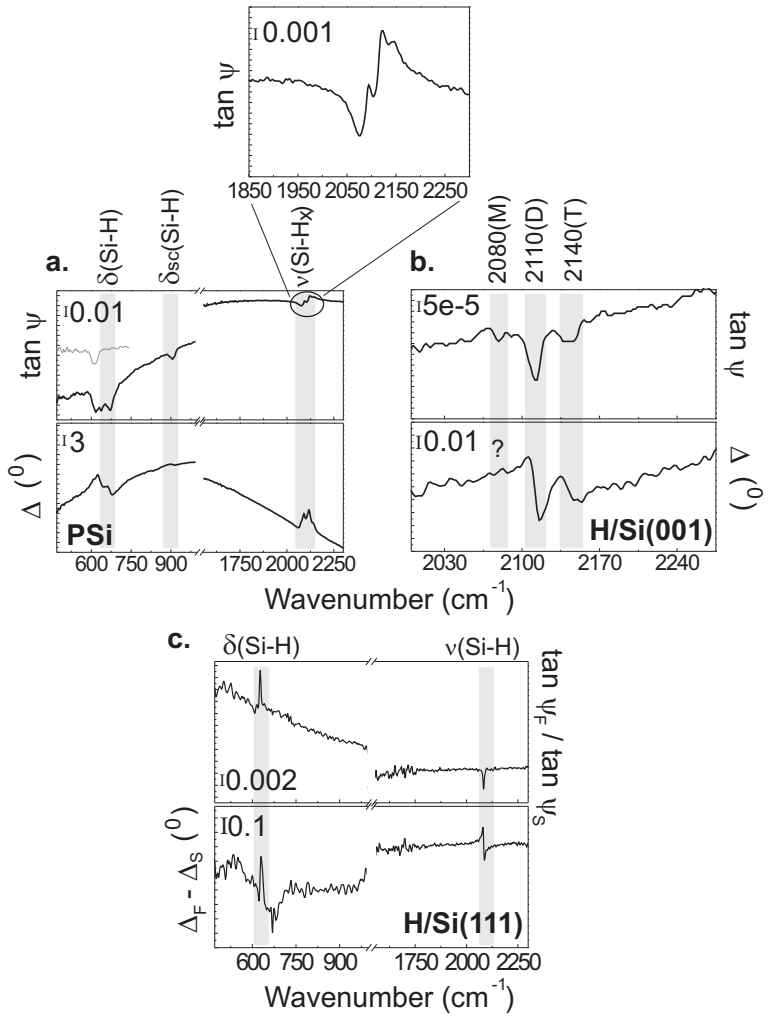

Figure 5.16: a. IRSE spectra of hydrogenated porous silicon; b. H–passivated Si(001) surface (from Ref. [121]); c. H–passivated Si(111) surface referenced to oxidized Si(111) surface. δ stands for bending and ν for stretching vibrations. Panel (a) zooms in the absorption peaks due to the ν(Si–H_x). In panel (b) the dihydride (D) and trihydride (T) stretching vibrations with the corresponding Kramers–Kronig related parts in Δ spectrum are marked. For monohydride (M)–related band at around 2080 cm^{-1} no correspondence in Δ was observed. The set–up related spectral between 590 and 632 cm^{-1} is shown in light gray on panel (a).

surface plane, in agreement with other works [41, 42, 43, 44, 45]. These perpendicular walls have a high volume for hydrogen passivation. This is reflected in the inverse band shapes of IRSE spectra of PSi as compared to the flat Si(001) and Si(111) cases.

5.4.2 Organic modification of porous silicon

In this section, IRSE spectra obtained from the organically modified porous silicon (PSi) are discussed. The focus is on two different types of modifications: nitrobenzene modification and methyl modification from Grignard compounds [139, 140, 141], as was described in section 2.2.1.

Fig. 5.17 shows spectra obtained from CH_3 and CD_3 modified, as well as from a non–modified PSi surfaces, for comparison. All spectra represent absorption bands due to Si–H bending vibrations in the range between 630 and 730 cm^{-1}. Thus, methylation does not replace all of the Si–H bonds of PSi. The absorption peak due to the rocking CD_3 vibration lies around 605 cm^{-1} [142], which unfortunately overlaps with the absorption band due to the IRSE setup (Fig. 5.17, gray curve). Spectrum obtained from CH_3/PSi exhibit an absorption band at 773 cm^{-1}, due to the rocking CH_3 vibrations [143]. The mode at 906 cm^{-1} also appears on all of the spectra and belongs to SiH_2 scissors vibrational mode. The modes between 2060 and 2150 cm^{-1} belong to the absorption peaks due to SiH_x stretching vibrations, as discussed in the previous section. This is also the region where the absorption bands due to stretching vibrations of CD_3 are expected [142]. The absorption peaks due to stretching vibrations of CH_3 are present at 2902 cm^{-1} (ν_{ss}(C-H)CH_3), 2931 cm^{-1} (ν_{as}(C-H)CH_2, hydrocarbon contamination remnants) and at 2969 cm^{-1} (ν_{as}(C-H)CH_3) [143]. Unfortunately, the above mentioned spectral overlaps hindered the observation of the absorption peaks due to the CD_3 molecular vibrations.

Similar to the discussion of Si–H orientation on the walls of the PSi, also here the shape of the absorption peak due to the molecular vibrations can be used to estimate the orientation of the CH_3 groups on the PSi walls. The peak due to rocking vibrations at 773 cm^{-1} has a peak-down feature, corresponding to a transition dipole moment perpendicular to the surface plane. On the other hand, the absorption bands between 2902 and 2980 cm^{-1} appear as peak–up features. The orientation of the transition dipole moments due to the methyl stretching vibrations ν_{ss}(C-H) and ν_{as}(C-H) thus should be considered. While the transition dipole moment due to the symmetric stretching vibration is oriented parallel to the symmetry axis of the methyl group, the transition dipole moment due to the asymmetric mode has projected components both in the direction of methyl symmetry axis and perpendicular to it [144]. The peak–up feature due to the symmetric stretching mode can arise due to the transition dipole moment oriented parallel to the surface (perpendicular to the walls of the PSi.) The transition dipole moment due to the asymmetric stretching vibration has components both parallel to the surface and perpendicular to it. However, the appearance of this absorption peak as a peak–up feature presumes that the major component of the transition dipole moment is also oriented parallel to

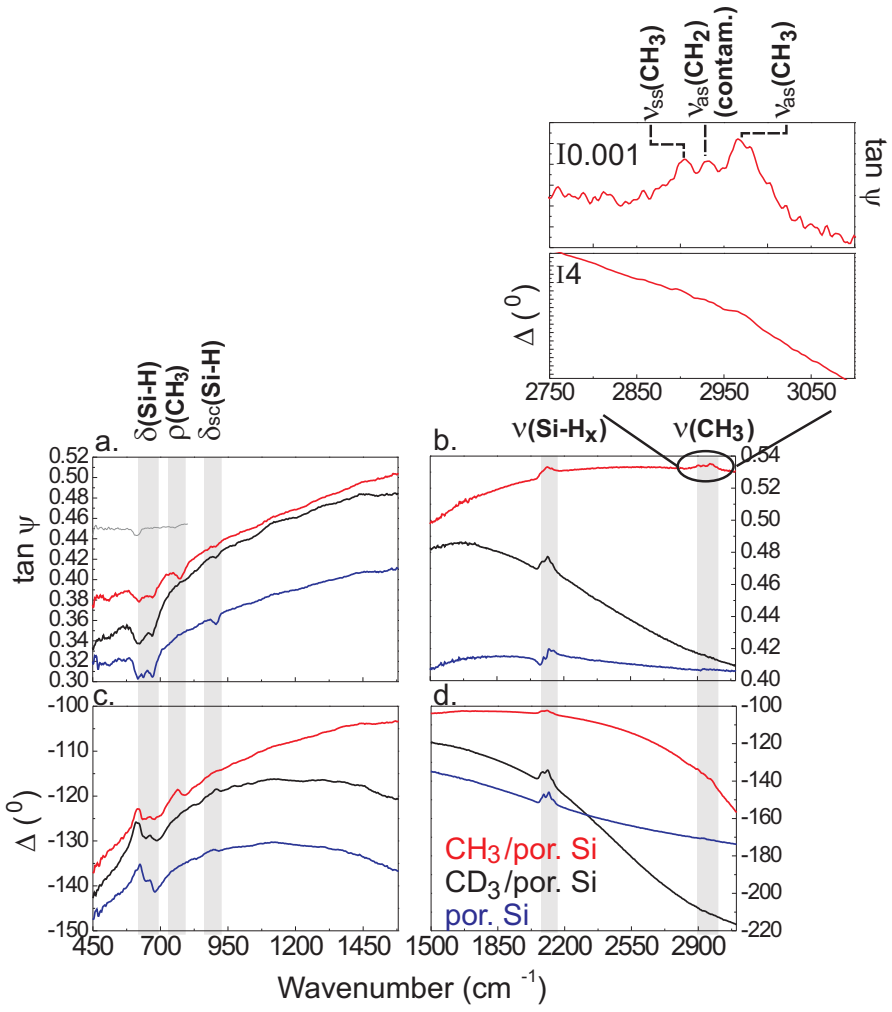

Figure 5.17: IRSE spectra obtained from PSi surfaces modified with CH_3 (red), CD_3 (black) and non–modified PSi (blue). a,b: tan ψ spectra in the spectral range between 450 to 1500 cm^{-1} and 1500 to 3100 cm^{-1}, respectively. c,d: the corresponding Δ spectra of the plots a,b respectively. The gray plot in (a) shows the absorption peak due to the IRSE setup, arising from the polarizers. ν: stretching; ρ: rocking; δ: bending vibrational modes.

the surface (perpendicular to the porous walls of the Si). Schematic drawing of the orientation of hydrogen and of the CH_3 groups on PSi as suggested by the observed lineshapes in the IRSE spectra was shown schematically in Fig. 5.15 (a). However, theoretical calculations involving pore parameters and the opening angle of the C–H bond of the methyl group are necessary in order to give a more precise understanding of the orientation of the methyl group in PSi.

On the other hand, the grafting of nitrobenzene on PSi does not result in any preferential orientation as no peak–up features in the spectra were observed, as shown in Fig 5.18. The assignment of the nitrobenzene vibrational modes was given earlier in Table 5.2. The spectra in Fig. 5.18 do not show any absorption peaks due to the bending vibrations of the remnant Si–H bonds between 630 and 700 cm^{-1}. Instead, observation of the absorption features in regions (a),(b) and (c) in Fig. 5.18 indicate the formation of SiO_x on the porous surface. Region (a) in Fig. 5.18 belongs to SiO_x related absorption bands in Si–O–H vibrational modes [135, 145] and to the Si–O bending vibrations in O–Si–O units [136]. A broad peak in region (b) between 1010 and 1265 cm^{-1} arises due to the Si–O–Si stretching vibrations [135, 145]. Spectral range (c) marked in Fig. 5.18 exhibits weak broad absorption peaks observed at 2130 and 2250 cm^{-1}, which were assigned to Si–H stretching mode in Si_2O–SiH units and to Si–H in O_3–SiH units in PSi, respectively [136, 138]. The main nitrobenzene related absorption peaks are band (3) in Fig. 5.18 at 1350 cm^{-1} ($\nu_{ss}(NO_2)$), band (4) at 1523 cm^{-1} ($\nu_{as}(NO_2)$) and band (5) at 1600 cm^{-1} (ν(C-C)$_{ring}$). These appear as peak–down features, similarly to the spectra obtained from Si(111), Au and TiO_2 surfaces as discussed in the previous sections. Band (2) at 1112 cm^{-1} was observed also for NB/TiO_2 (see Table 5.2) and was assigned to a combination C–N stretch and ring breathing vibration mode. The origin of the weak band at 752 cm^{-1} labeled (1) is not clear. As no mode at this frequency was listed as resulting from the nitrobenzene molecular vibrations as adsorbed on a surface or in a liquid state [114], one of the possibilities can be that this mode belongs to the Si–C stretching vibrations. The detailed discussion of Si–C bond will be presented in section 5.4.3.

The spectra in Fig. 5.18 suggest that in contrast to methylated PSi surface, oxidation occurred for NB–modified PSi. The oxidized interface results from the grafting in aqueous solution, which was not the case for the methylated surfaces. In addition, no preferential orientation similar to the CH_3–modified PSi was observed. This could be due to the polymerization of radicals discussed in section 5.2 which probably occurs during grafting on PSi, leading to a loss of the structure of the grafted molecules.

5.4.3 The Si–C bond: discussion

In principle, strong signals from absorption peaks of PSi can be utilized for searching for the Si–C bond, that should arise due to a covalent attachment of the molecules to the surface. Yamada et al [146] performed HREELS studies on methylated Si(111) surfaces and assigned Si–C stretching mode at 683 cm^{-1} and Si–C bending mode at 507 cm^{-1}. Theoretical studies on methylated Si(111) sur-

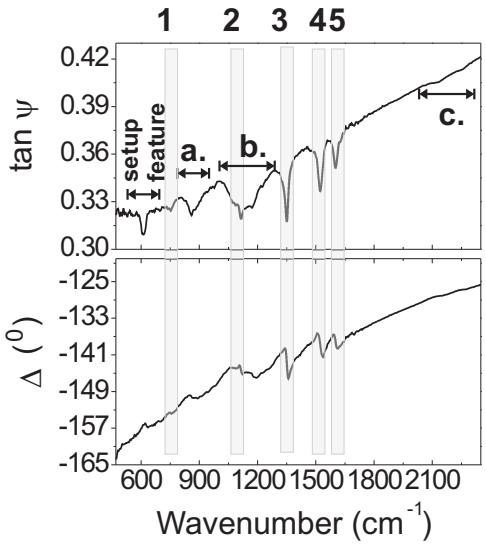

Figure 5.18: IRSE spectra of nitrobenzene on PSi. The absorption feature between 590 and 632 cm^{-1} was due to polarizers in the setup. Regions a–c, as well as the absorption peaks 1–5 are discussed in the text.

faces [147] resulted in assignment of Si–C stretching mode at around 640 cm^{-1} and of the bending mode in the range between 480–500 cm^{-1}. Our spectra of PSi (Fig. 5.17) show a weak peak at 509 cm^{-1} which is however observed for all of the surfaces: H-passivated PSi, CH_3–modified and CD_3–modified PSi. Thus a clear assignment of the bending mode is not possible in our case. The absorption peak due to the stretching Si–C vibrations is expected in the range of the Si–H bending vibrations, thus we could not observe it either. As to nitrobenzene Si–C bond, the HREELS results of Ref. [148] showed a Si–C bond at 615 cm^{-1} for benzene at Si(100) and at 540 cm^{-1} for benzene at Si(111) surfaces. These modes either overlap with the absorption band resultant from our setup or outside the detection region. An additional possibility is that nitrobenzene binds to Si surfaces through Si–O–C bond. All of our XPS spectra have indicated suboxides species even when HF was added to the electrolyte, raising a possibility that the grafting may require the formation of Si–O–C bond. However, these suboxides could result also from the rinsing of the sample in water after grafting. FTIR studies of methanol on Si surfaces indicate the formation of absorption peak due to Si–O–C between 1085 and 1100 cm^{-1} [149]. Similar studies by Michalak et al [150] on deuterated methanol showed absorption due to Si–O–C bond of Si–O–CD_3 between 1078 and 1088 cm^{-1}. In nitrobenzene on PSi spectrum, this spectral range is overlapping with a broad peak due to the vibrations of SiO_x.

As was already mentioned, spectrum shown in Fig. 5.18 exhibits a weak band at 752 cm^{-1} labeled (1) whose origin is not clear. For instance, no mode at this frequency was listed as resulting from the nitrobenzene molecular vibrations as adsorbed on a surface or in a liquid state [114]. There is a possibility that this mode belongs to the Si–C stretching vibrations. Gurthner et al [151] observed an absorption peak at 762 cm^{-1} for electrochemical grafting of methyl iodide on PSi. While unfortunately this spectral range overlaps with strong absorption peaks due to the Si–H for methyl terminated PSi (Fig 5.17), the absorption band (1) present in the NB/PSi spectrum in Fig. 5.18 can be due to the Si–C absorption. However a more clear assignment may be provided upon isotope labeling of either C or H atoms in the phenyl ring, which will lead to the shift of the possible absorption peak due to the Si–O–C or Si–C stretching vibrations. Additionally, further extension of the spectral range toward even lower wavenumbers may help in detection of Si–C bending vibration if this is the case for the electrochemical attachment of the molecules to Si surfaces.

5.5 Summary

This chapter summarized the characterization work on electrochemically grafted organic thin films. Through the combined XPS and IRSE results we showed that electrochemical preparation leads to organic termination with the grafted molecules on different surfaces. Cross–referencing the data from complementary techniques helped us in quantitative determination of optical parameters and thickness of the thin films. IRSE analysis enabled studies of molecular orientation of the organic molecules on various substrates. The obtained results point to formation of films consisting of several layers of the organic molecules, which is likely due to polymerization of radicals during the electrochemical procedure. The films grafted from benzene derivatives showed no preferential orientation on the host surfaces.

The situation was different when IRSE spectra of PSi were compared to those obtained from Si(111) and Si(001) surfaces. First, the spectra showed substantial differences in absorption peak shapes due to Si–H vibrational modes. Second, absorption peaks due to molecular vibrations of CH_3 terminated porous silicon showed similar trends in lineshapes as hydrogenated PSi. Based on these obsevations, we estimated the orientation of the hydrogen and of the CH_3 on porous silicon with the molecular symmetry axis perpendicular to the porous walls. Such orientation was not detected in nitrobenzene grafted on PSi, which exhibited features similar to those detected in unordered thick films on TiO_2 surfaces.

The next chapter presents characterization of the silicon oxide interface which forms below the organic layer as a result of the exposure to atmospheric conditions and during the electrochemical grafting process.

Chapter 6

Passivation and oxidation of Si surfaces

In the previous chapter, it was shown that electrochemical grafting leads to a successful termination of the electrode surfaces with organic molecules. For silicon surfaces, the formation of the oxidized SiO_x interface was briefly mentioned. In this chapter the studies on interfacial structure between grafted organic layer and Si(111) surfaces are presented in more details. Generally, uncontrolled SiO_x interfaces are undesired in the engineering of the hybrid organic/silicon devices, since they introduce a large number of surface electronic trap states [152]. The understanding of the processes governing the formation of the SiO_x interface and its prevention are thus important.

These studies were realized through the measurements delivered by IRSE, XPS, VIS–ellipsometry and AFM methods. Deconvolution of the Si2p core level spectra gave insight to the SiO_x structure of the sample. Cross–referencing of the results from IRSE and XPS enabled quantification of the SiO_x layer thickness. The model included the substrate/SiO_x/nitrobenzene layer, where the SiO_x layer was simulated taking into account the possibility of an "island"–like structure (see Fig. 4.12 in the earlier section 4.2.2).

It is shown that in general, organic thin films slow down the oxidation when the samples are exposed to ambient conditions. It was found that different organic molecules dictate different oxidation kinetics of the silicon interface.

This chapter presents that the HF addition into the electrolyte can prevent the formation of an oxidized interface. HF also was found to successfully remove the oxidized SiO_x interface which formed when the samples were stored for a certain time under atmospheric conditions. It was expected that such HF treatment would also remove the organic layer grafted above the oxidized silicon interface. However, the absorption peaks due to the overlying organic layer remained unchanged as exhibited by the IRSE spectra after the HF treatment. A model for such peculiar behavior is proposed.

This chapter is structured as follows: First, characterization of hydrogen-

passivated Si(111) exposed to atmospheric conditions is presented along with the simulations of the degrading absorption peaks due to the Si–H molecular vibrations as measured by IRSE. Further, we show that during storage under atmospheric conditions, grafted organic monolayers slow down the formation of the SiO_x interface. Using cross–correlated XPS, IRSE and VIS–ellipsometric studies, quantitative analysis of the SiO_x layer forming on the Si(111) substrate under ambient conditions in the initial stages of oxidation and after 1 year of storage is performed.

6.1 Stability of H-passivated Si (111) surfaces

Optical characterization of the Si surfaces gives insight into the initial composition of the surface before the grafting as to its hydrogen termination, surface oxides presence and contaminations. In section 5.4.1 we presented IRSE studies of Si(111) hydrogenated surfaces and compared the results to the spectra obtained from PSi. In this section, we perform studies on degradation of the Si–H passivation as a result of exposure to ambient conditions.

Fig. 6.1 shows a series of spectra that were obtained from the Si(111) surface upon storage under ambient air conditions. Degradation of the surface is expressed in disappearance of the initially strong ν(Si–H) absorption band around 2082 cm^{-1}. Si surfaces are very unstable under ambient conditions and the degradation typically occurs within 24 hours. The red curves in Fig. 6.1 show the results of simulations. The fitting parameters are summarized in table 6.1. The measured optical constants of oxidized Si substrate were taken to simulate the substrate, thus the simulated spectra include the measurement noise. In the simulations, the value for the high frequency refractive index $n_\infty = 1.1$ was taken from the ref. [64,38]. The Si-H layer thickness was taken as the length of the Si-H bond of 1.5 Å [65].

The degradation was simulated varying the fraction of a surface coverage with the Si-H bonds. This was done through the superposition of the reflection coefficients, with $r_{total} = \theta r_{SiH} + (1 - \theta) r_{Si}$ where θ was the coverage of the Si surface with Si–H bonds, r_{SiH} was the reflection coefficient calculated with the Lorentz oscillator for simulation of the absorption peak due to the Si–H stretching vibrations and r_{Si} was calculated as r_{SiH} but without the Lorentz oscillator at this position. The superimposed quantity r_{total} represents the radiation reflected from H–terminated parts of a Si surface and the radiation which is reflected from Si atoms which are not bonded to the H atoms due to the degradation under air.

Initially, the surface is fully hydrogen-terminated, with the S-H coverage fraction of 1. As oxidation proceeded, the Si-H coverage fraction gradually became smaller and after 24 hours, it was fitted with the coverage value of 0.1. However, this parameter did not compensate for the Si-H peak broadening which occurred during the oxidation. It was necessary to change the broadening oscillator parameter Γ in order to simulate the spectrum broadening.

Integration of the coverage parameter into our simulations is based on the

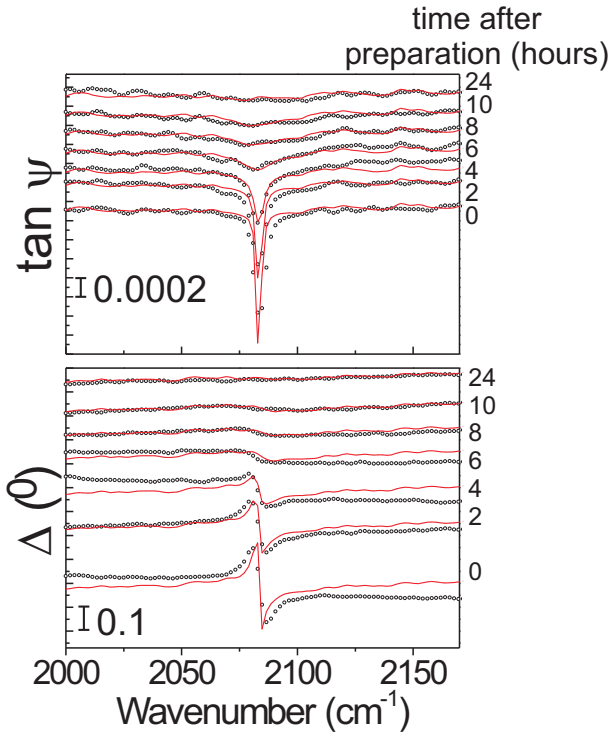

Figure 6.1: Ellipsometric spectrum obtained from hydrogen passivated Si(111) surface. Black circles: measured data; red line: simulated spectra. On the right side a storage time in hours is shown beside each spectrum. The measured optical constants of oxidized Si substrate were taken to simulate the substrate, thus the simulated spectra include the measurement noise. For the lowest presented absorption amplitude after 10 hours the tan ψ SNR was 3 and SNR of Δ was 7.

Frequency ω_0 (cm^{-1})	time (hours)	F (cm^{-2})	Γ (cm^{-1})	coverage
2077	0	32000	2	1
2077	2	32000	3	0.9
2077	4	32000	5	0.75
2075	6	32000	10	0.6
2075	8	32000	16	0.5
2075	10	32000	16	0.4
2075	24	32000	16	0.1

Table 6.1: Fitting parameters for hydrogen degradation series as shown in Fig.6.1

model proposed by Miura et al [153]. In this model, the water present in the air is predominantly involved in the oxidation of surface Si-H bonds. At the next step, native oxide grows where most of the surface Si-H bonds were already eliminated (Fig. 6.2). The variable $\theta = \theta_1 + \theta_2$ in Fig. 6.2 corresponds to the coverage fraction used in our simulations.

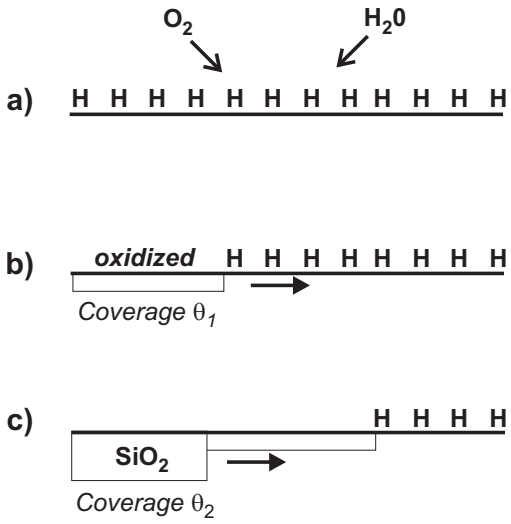

Figure 6.2: A model proposed for oxidation kinetics of hydrogen-passivated Si surfaces, after Miura et al [153]. a. Initially H-terminated Si surface; b. Initiation of the surface oxidation; c. Native oxide formation favorably proceeds on the oxidized surface simultaneously with further degradation of the Si-H bonds.

The broadening of the Si–H absorption peak is also in agreement with the literature. Ogawa et al [154] confirmed that the broadening does not result from physically adsorbed contaminations from ambient atmosphere. They proposed that the spectral broadening can be inferred to the oxygen entering subsurface of silicon lattice sites and distorting the lattice, influencing Si-H vibrational properties. Broadening due to the interaction with the lattice was confirmed from observation of the deuterium-terminated diamond C(111) surfaces as compared to the hydrogen-terminated C(111) surface [155]. The broadening of the absorption line for deuterium-terminated C(111) was found to be stronger than for the hydrogen-terminated C(111) diamond surface. For the deuterium on C(111) the stretching frequency is situated closer to diamond surface phonons compared to that of the C–H stretch. Thus the C–D stretching motions can easily relax via a two-phonon process, resulting in broad features in the IR spectra. Dephasing due to coupling to the lattice phonon modes on hydrogenated semiconducting surfaces was confirmed by measurements and calculations performed by Wang et al [156].

Other effects that can be responsible for the broadening of the absorption peak and its frequency shift are the dynamic and static multipole coupling mechanisms. The former is due to the transition multipole coupling, with the dominating dipole coupling. The latter is due to interaction between permanent multipoles, i.e. the chemical environment of the adsorbates [157]. The close spacing of surface adsorbates affects the vibrational spectrum because the motion of an individual oscillating dipole is influenced by the electric dipole field generated by the motion of its neighbors. This effect forces adsorbates bound to a surface to vibrate together instead of individually and shifts the vibrational transition relatively to single Si-H vibration. The coupling is dependent on the morphology of the overlayer, thus the surface structure (etch pit density, roughness) determines the frequency shift and broadening [158]. This effect is relevant in studies of surface morphology upon preparation of hydrogenated Si surfaces, where etch-pits have a strong influence on the shape and frequency of the Si-H absorption peak [158].

In case of hydrogen passivated Si(111), dynamic dipole coupling is influenced by changes in morphology during the surface degradation. For instance, AFM studies showed that within the first 10 to 22 hours under atmospheric conditions, the surface roughness increased [159,160]. The roughness influences the dynamic dipole coupling and leads to broadening of the absorption spectra and to the frequency shift to lower frequencies [158]. Additional effect that might have an influence on the dynamic dipole coupling is a removal of part of the Si-H bonds during the oxidation, which may lower the overall dipole field [158]. A similar red-shift and broadening of the Si-H absorption peak was observed by Lambers and Hess [161] upon F_2 laser induced oxidation (wavelength 157 nm), and was assigned to the loss of the dynamic dipole coupling.

6.2 Oxidation under atmospheric conditions

In order to investigate the stability of organic layers/Si(111) interfaces to atmospheric conditions, we monitored IRSE spectra of H/Si(111), NB/Si(111), and 4–methoxydiphenylamine (4–MDA) on Si(111) for one year. Fig. 6.3 presents the monitored spectra for each of the substrates (plots a,b,c). A comparative graph between the above samples is shown by plot (d). As was discussed in section 5.3, there are several absorption bands due to molecular vibration of 4–MDA overlapping with the SiO_x absorption region. However, it is clear from Fig. 6.3 (d) that the oxidation process of the 4–MDA modified Si surface proceeds much slower than for the other two substrates. There are also some differences in oxidation pattern for H/Si and NB/Si. After 18 hours of storage, no bands due to SiO_x can be yet observed for NB/Si and H/Si samples. However, after 50 hours, there appear major differences in the absorption region of SiO_x. For H/Si sample, a distinguishable SiO_x absorption band can be observed. A similar band also appears for NB/Si sample, but of about half of the amplitude which is observed for H/Si sample. Similar tendency is seen also after 6 days of oxidation: the amplitude of the SiO_x–related absorption bands is

much smaller for NB/Si than for H/Si sample. After this time period, the oxide thickness on H/Si sample reaches about 0.6 nm, based on IRSE simulations as described in section 6.3. After 27 days, the amplitude of the SiO_2 related bands on the spectrum obtained from NB/Si approaches the one that can be seen on H/Si spectrum. After 388 days, the SiO_x–related absorption bands become of a similar amplitude at 1220 cm^{-1}, with minor differences between 1140 and 1160 cm^{-1}. The amplitude of the SiO_x–related absorption bands of 4–MDA/Si sample remains smaller than for H/Si and NB/Si during this observational period. The thickness of the SiO_2 on H/Si sample was 2.5 nm after 388 days, as obtained from VIS–ellipsometric measurements. All of the spectra exhibit a shift of the SiO_x related absorption band to higher frequencies as the oxidation proceeds. This shift is due to changing oscillator parameters which is the result of the changing bonding configuration from SiO_x to SiO_2 interface. The next section will present the simulations of the IRSE spectra in this region, showing that the shift can be reproduced in optical models.

AFM images of the H/Si, NB/Si and 4–MDA/Si are shown in Fig. 6.4 after 19 days after 466 days of oxidation. The RMS roughness after 19 days of oxidation was 0.8 Å for H/Si, 2 Å for NB/Si and 1.5 Å for 4–MDA/Si. The roughness value for H/Si surface is in a good agreement with refs. [160,159], but somewhat underestimated in comparison to ref. [162] which reported the lowest RMS roughness of 1.4 Å upon NH_4F treatment. After 466 days, the RMS roughness of 6 Å was observed for H/Si sample, 3 Å for NB/Si and 3 Å for 4–MDA/Si. The roughness of H/Si surface varies strongly with oxidation, and eventually after 466 days was higher than the roughness observed for organically protected Si(111) surfaces.

These results demonstrate that the organic thin films slow down the oxidation of the interface, and that the size of the molecule plays an important role in oxidation dynamics. Surface morphology is also effected by oxidation. However, surfaces covered with thin organic films exhibited a lesser roughness than the non–coated Si surface. The roughness after one year of oxidation was found to be independent on the type of the grafted molecules. These properties can be utilized in engineering of electronic devices for protection against interface oxidation.

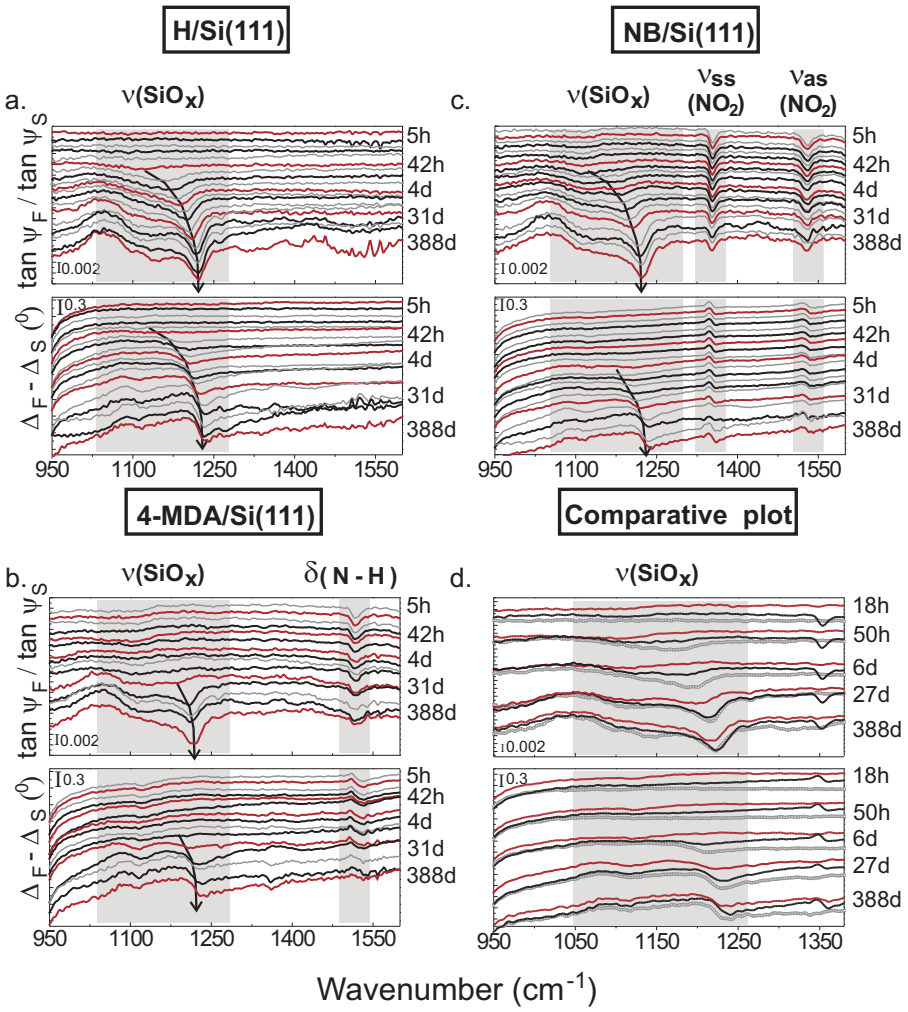

Figure 6.3: IRSE spectra monitoring oxidation of the H-passivated Si(111) (a), NB–modified Si(111) (b) and 4–MDA modified Si(111) (c) under atmospheric conditions. Time of storage is selectively shown for spectra marked in red. (d). Comparative plot of the spectra obtained from the above samples. In plot (d), 4–MDA/Si is shown by red line, NB/Si by black and H/Si by gray. In plots (a,b,c) the colors are implemented only for a contrast. All data was referenced to the spectrum of freshly prepared H-passivated Si(111).

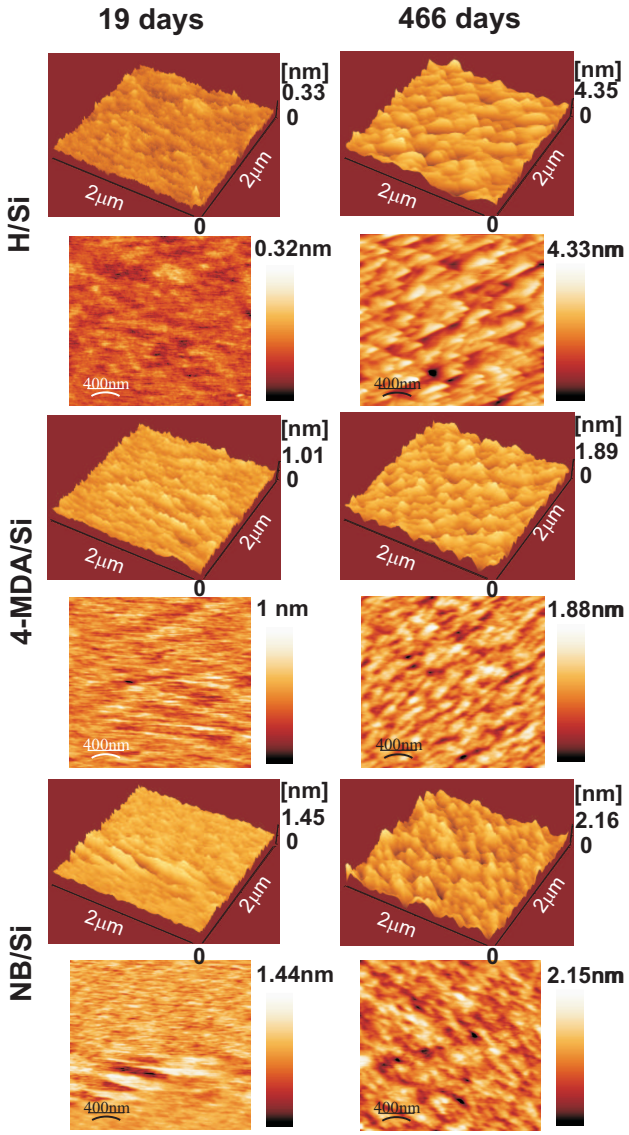

Figure 6.4: AFM images of H/Si, 4–MDA/Si and NB/Si after 19 days (left column) and 466 days of oxidation (right column). The RMS roughness after 19 days oxidation was 0.8 Å for H/Si, 2 Å for NB/Si and 1.5 Å for 4–MDA/Si. After 466 days, the RMS roughness was 6 Å for H/Si sample, 3 Å for NB/Si and 3 Å for 4–MDA/Si.

6.3 Determination of the optical parameters in mid–IR spectral range for SiO_x layer forming under ambient conditions on Si(111) surface

In this section we determine the Lorentz oscillator parameters for SiO_x forming on Si(111) in the initial stages of oxidation (below 1 month of storage) and subsequently after 1 year of oxidation. For this, we used a cross–correlated analysis of IRSE with XPS and VIS–ellipsometry. In the initial stages of oxidation, XPS was used for determination of the thickness of the forming SiO_x layer. After one year of oxidation, VIS–ellipsometry was used for this purpose.

Fig. 6.5 shows XPS results for the freshly prepared H–passivated Si(111) and Fig. 6.6 (a) shows the same sample in its initial stages of oxidation, including the assignment of the Si^0 to Si^{+4} peaks. Both figures contain IRSE results obtained from the other piece of the same sample, synchronously.

IRSE spectra in Fig. 6.5 reveal a strong ν(Si-H) band due to Si-H stretching vibration at around 2082 cm^{-1}. At the same time, broad absorption band due to $\nu(SiO_x)$ can be observed between 1060 cm^{-1} and 1170 cm^{-1}. However, this peak probably results mainly from the *interstitial* oxides. This is supported by deconvolution of X-ray photoelectron spectra, which reveal only a minor sub–oxide structure of the sample. Here, the predominance of the Si^{+1} peak points out the formation of the Si–OH surface hydroxides. There is also a minor contribution due to the silicon in the Si^{+4} oxidation state, which presumes a minor occurrence of the silicon back–bond oxidation. Fig. 6.6 (a,b) shows the results of

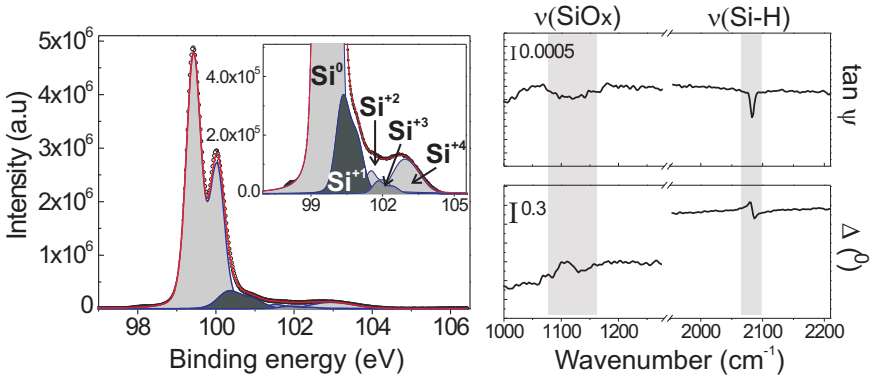

Figure 6.5: XPS (left) and IRSE (right) spectra from freshly prepared hydrogen-passivated Si(111) surface. XPS data was obtained at 150 eV photon energy. On the inset: zoom–in of the XPS spectrum showing the sub–oxide deconvoluted components.

the measured sample after several days of storage under atmospheric conditions. The XP spectrum exhibit the predominance of the Si^{+4} component, pointing out the silicon oxidized back–bonds. Calculations based on XP spectrum shown in (Fig. 6.6 (a)) resulted in oxide thickness of 6 Å . Using this data as input, we performed simulations of the IRSE spectra. The results of the simulations are presented along with the measured IRSE data in Fig. 6.6 (b). The sample was measured subsequently after one year of oxidation with VIS–ellipsometry and exhibited a thickness of 2.5 nm. Fig. 6.6 (c) illustrates the fitted IRSE spectrum obtained from the sample after 1 year of oxidation. Table 6.2 summarizes the parameters that were obtained from the best–fit calculations of the above IRSE spectra using the Gaussian distribution of Lorentzians model [59] (see section 3.2.1 for details), for the sample in initial stages of oxidation and after 1 year storage under atmospheric conditions. IRSE spectra exhibited in panels (b,c) in Fig. 6.6 mark the positions of the resonance frequencies ω_0 which were used in the simulations. However, the related absorption peaks positions are shifted in both the measured and the simulated spectra. This is the result of the optical effect for Lorentz oscillators with a relatively high oscillator strength F. This optical effect is frequently referred to as the Berreman effect [66].

Fit	Frequency ω_0 (cm^{-1})	F (cm^{-2})	Γ (cm^{-1})	σ (cm^{-1})
Fig. 6.6 (b)	1053	281570	10	36
(initial stages of oxidation)	1146	89047	10	39
Fig. 6.6 (c)	1075	170000	10	36
(1 year of oxidation)	1185	83000	6	32.5

Table 6.2: Parameters used in simulations of SiO_x absorption peak as shown in Fig. 6.6. The thickness was 6 Å as obtained from XPS data for the sample under initial stages of oxidation and 2.5 nm as obtained from VIS–ellipsometry for the sample stored for 1 year under ambient conditions. The ϵ_∞ was 2.1.

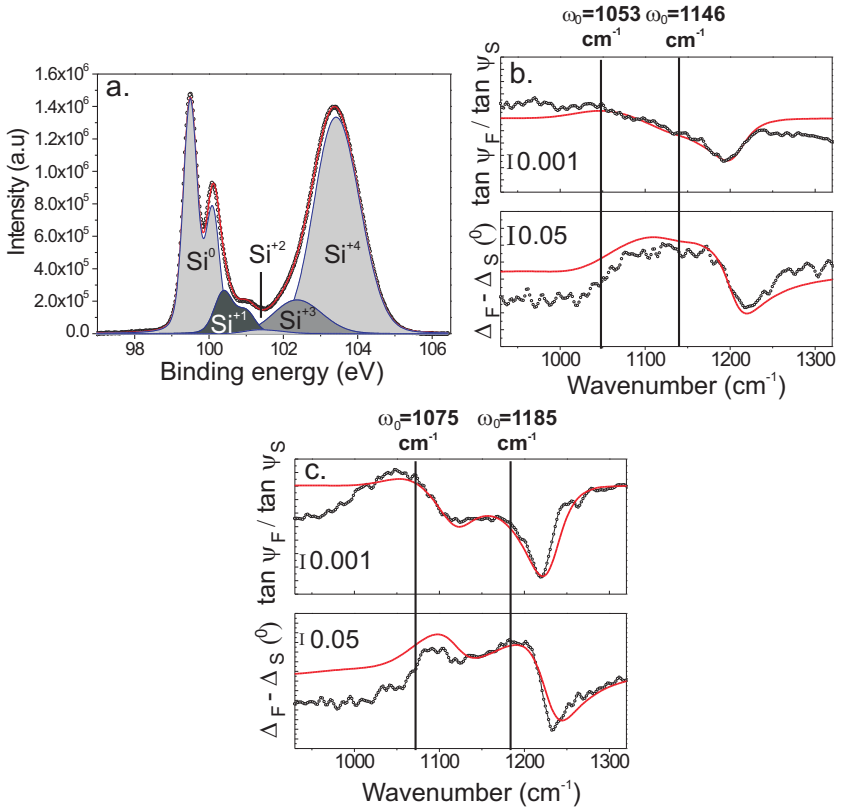

Figure 6.6: a. XPS and b. IRSE spectra from initially hydrogen-passivated Si(111) surface after storage under atmospheric conditions. Si^0 to Si^{+4} deconvoluted components are marked on the XPS spectrum. IRSE spectra show the measured data (black) and calculations (red) using ϵ_∞=2.1 and thickness of 6 Å , as calculated from XPS. XPS data was obtained at 150 eV photon energy. c. IRSE spectrum obtained after one year of oxidation and fitted with thickness of 2.5 nm as obtained from VIS–ellipsometry with ϵ_∞=2.1. Positions of the Lorentz oscillator used in the calculations (see Table 6.2) are marked in panels (b) and (c).

6.4 SiO_x interface formation during the electrochemical grafting

As was presented in section 2.2.3, SiO_x interface can form during electrochemical grafting in the aqueous surrounding. Formation of the oxide interface may be prevented when HF is added to the electrolyte [163]. The goal of this work was to compare the interfacial structure of two samples: the one on which the nitrobenzene was grafted in HF–free solution (sample A) and the other prepared in HF–containing solution (sample B).

Addition of HF into the electrolyte can prevent formation of the SiO_x interface during electrochemical grafting as outlined in Fig. 2.10 of section 2.3. The process results in etch–back of the Si surface atoms from hydrogen–passivated surface. Thus, when aryl diazonium salts are added into the HF–containing electrolyte, the grafting process proceeds in parallel with the HF–etch of the surface. Fig. 6.7 shows XPS and IRSE results obtained from the two pieces of the same freshly–prepared samples A and B. Both XPS and IRSE spectra in Fig. 6.7 clearly indicate that a higher amount of SiO_x was present in sample A. IRSE spectra indicated also a higher nitrobenzene amplitude of the absorption peaks of about 20% for sample A. This is in agreement with our previous observations of NB grafting on oxidized Si surfaces. Fig. 6.8 shows histograms of Si^{+x} distribution in samples A and B. Fig. 6.8 (a) shows histogram of the Si^{+x} integrated intensities, normalized to the integrated intensity of the bulk Si^{+0} component. The ratios I(Si^{+x}) / I(Si^{+0}) are proportional to a number of Si atoms in the intermediate oxide state. From this comparison, it is evident that the total oxide content Si^{+all} ($Si^{+all}=\sum_{i=0}^{n} Si^{+x}$) is higher for sample A. Also, Si^{+x} oxide contents in sample A are higher than in sample B for x=1..3. However, it is not the case for Si^{+1} component, where the normalized integrated intensity is higher for sample B. In other words, there are more Si atoms in this intermediate state in sample B than in sample A. Fig. 6.8 (b) presents the percentage of Si^{+x} components from the sum of integrated intensities Si^{+all}. The Si^{+1} integrated intensity in sample B is around 20% of the sum over the Si^{+x} normalized integrated intensities Si^{+all}, while in sample A, it is only around 4%. These results point out the predominance of the Si^{+1} oxidation state in sample B and on the advanced oxidation stage in sample A (lower Si^{+1} intensity, higher intensity of the fully oxidized Si^{+4} component.)

For calculation of the interfacial SiO_x layer thickness from XPS data nitrobenzene overlayer should be taken into account. This demands a knowledge of the nitrobenzene IMFP values. To our knowledge, such values have not been reported in literature so far. However, this can be avoided if calculations are performed using data obtained at several photon energies, as discussed in section 4.2.2. Equation 4.15 can be used to estimate the upper limit for SiO_x thickness. Using IMFP of 6.5 Å and $\frac{c_i}{c_{sub}} = 0.84$ for SiO_2 layer at 240 eV [90], the estimated upper limit for the SiO_x thickness is 9 Å for sample A and 3.5 Å for sample B. The oxidized NB/Si(111) interface for sample B is most probably a result of water rinsing after the grafting. Due to the nitrobenzene molecular

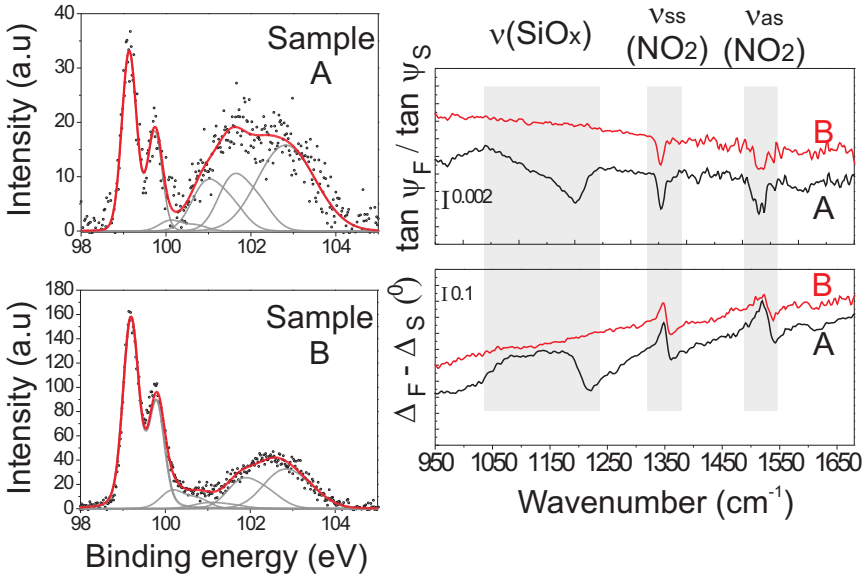

Figure 6.7: XPS (left) and IRSE (right) spectra obtained from the samples prepared without addition of HF into electrolyte (sample A) and with HF (sample B). XPS data was obtained at 240 eV photon energy. The histogram comparing the Si^{+x} relative distribution in samples A and B is shown in Fig. 6.8.

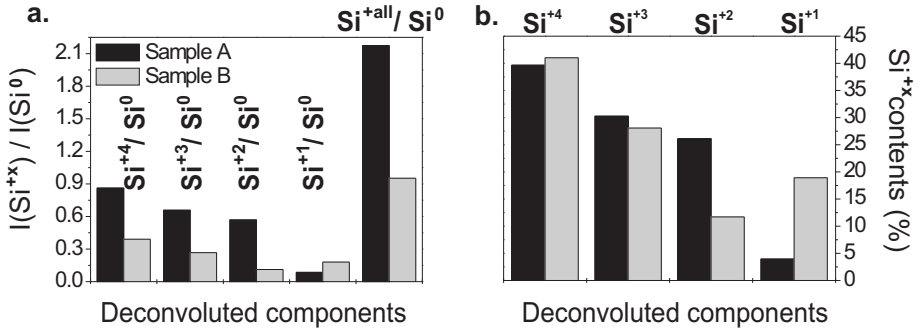

Figure 6.8: a. Histogram of Si^{+x} (x=1..4) intensities normalized to the bulk Si^{+0} intensity, for sample A (black) and sample B (gray), as shown in XP spectra in Fig. 6.7. The right–most columns present a Si^{+all}/Si^{+0} ratio, where $Si^{+all}=\sum_{i=0}^{n} Si^{+x}$. b. Distribution of Si^{+x} percentage from the total Si^{+all} value.

steric hindrance, not every Si atom is occupied by nitrobenzene molecule, living a space for Si–OH formation of the top Si atoms and the further process of the back-bond oxidation.

When no HF is added into the electrolyte, a competition between nitrobenzene grafting and reaction of the Si surface with the H_2O molecules in aqueous solution presumes silicon oxide island formation, which can be the case for sample A. Island formation can also proceed for sample B as a result of the above mentioned post–grafting oxidation during water rinsing. Thus, the actual calculation of the SiO_x thickness is even more complicated if the SiO_x island structure is taken into account. We employed Eq. 4.19 as described in section 4.2.2 to estimate the silicon oxide thickness and coverage, using the XPS spectra obtained at 650 eV and at 240 eV. To calculate the NB layer thickness we used IRSE simulations with the parameters from Table 5.3. The nitrobenzene thickness values were cross-checked using XPS Multiquant program (see section 4.2.2), where the obtained SiO_x thickness and coverage were used as input parameters. A good agreement for the thickness values was found between the IRSE simulated results and the XPS Multiquant analysis (the difference between the results obtained from simulations of IRSE spectra and XPS Multiquant analysis lied within 15% of the obtained thickness values). Table 6.3 summarizes our results.

Sample	Thickness d_{SiOx} [nm]	Coverage θ_{SiOx}	Product $d_{SiOx}\theta_{SiOx}$ [nm]	NB thickness d_{NB} [nm]
Sample A (HF-free)	0.85	0.9	0.77	7
Sample B (HF-treated)	1.3	0.2	0.26	5

Table 6.3: Estimated thickness and coverage parameters as obtained from XPS data. The thickness and coverage of the model were defined in Fig. 4.12 of section 4.2.2.

The results show that the total SiO_x thickness $d_{SiOx}\theta_{SiOx}$ is about three times higher for sample A. In addition, the obtained coverage (θ_{SiOx}=0.9) for sample A points out an almost fully formed SiO_x interface. These results suggest that the competition between grafting of the NB radicals and reaction with the H_2O molecules favors the attachment of the OH radicals to Si atoms. The relatively high contribution of the Si^{+4} component in the XP spectrum of sample A in Fig. 6.7 suggests the silicon back–bond oxidation. SiO_x coverage θ_{SiOx} for sample B was 0.2, with thickness d_{SiOx}=1.3 nm. IRSE spectra did not show any pronounced peak in the SiO_x region for this sample. For comparison, H–passivated Si(111) surface oxidized under atmospheric conditions (see in Fig. 6.6) exhibited a much higher absorption intensity in the IRSE spectra, while the estimated thickness of SiO_x was 0.6 nm. In case of sample B, the product $d_{SiOx}\theta_{SiOx}$ was 0.26 nm, which is about three times smaller than the thickness value obtained for the above hydrogen–passivated Si stored under atmospheric

conditions. Probably the low coverage and the low overall thickness $d_{SiOx}\theta_{SiOx}$ play an important role in formation of the IRSE spectra. Another possibility is that irradiation with X–rays triggers an additional oxidation of the sample through reduction of the nitrobenzene where the release of oxygen can cause the oxidation of the silicon interface (see chapter 7 for details of the X–rays induced reduction.) However, as will be seen in chapter 7, the decomposition results in larger time scales than the time that it takes to obtain a single XP spectrum. Thus the measured intensities do reflect to some extent the *initial* state of the sample as prepared, although the silicon–oxide composition might be somewhat higher in the X–ray irradiated part of the sample than in the non–irradiated one which was measured by IRSE. This is due to the photochemical oxidation processes triggered by X–ray irradiation. An additional source for interface oxidation can be the residual water which may be included in the electrochemically grafted thin films as was discussed in section 5.2. The oxidation of the interface can be caused by irradiation of these residual water inclusions [164].

6.4.1 Stability of the organic films on oxidized surfaces to HF treatment

In this section, we explore the post–grafting oxidation of the interface between the organic films and the silicon substrate in air and discuss the removal of this layer in HF solution. Subsequent oxidation of samples A and B was monitored with IRSE after two months of exposure to atmosphere. The spectra are shown in Fig. 6.9 by black curves. For sample B, the absorption band due to SiO_x appears in the range between 1050 and 1250 cm^{-1}, which was not seen directly after the preparation (see Fig. 6.7 for comparison). For sample A, the amplitude of this band becomes larger in comparison to the as–prepared sample (compare with the results in Fig. 6.7). These results illustrate that oxidation proceeds on the NB/Si interface upon exposure to atmospheric conditions on both of the samples.

In order to investigate the stability of such interfacial SiO_x layer to HF etch, the samples were etched in 2% HF solution for 20 sec. The results are shown in Fig. 6.9 by red curve, for both sample A and sample B. While the absorption bands due to SiO_x disappear from the IRSE spectra, the NB–related absorption bands remained unchanged. This is a surprising result, since one would expect that NB would be etched off from the sample with the below–lying SiO_x interface.

For a better understanding of these results, electrochemical grafting on chemically oxidized Si surfaces was performed, with a subsequent HF etch. In Fig. 6.10 the IRSE spectra for the samples as prepared are shown in red and the HF–treated samples are shown in black. In this figure, "sample a" refers to a bare chemically oxidized sample, "sample b" was grafted during 110 sec (thickness d_{NB}=3 nm) and "sample c" was grafted during 550 sec (thickness d_{NB}=14 nm). Chemical oxidation resulted in about 2 nm of silicon oxide layer, as obtained from IRSE simulations on sample a. HF treatment resulted in disappearance of the SiO_x–related absorption peak, while NB–related absorp-

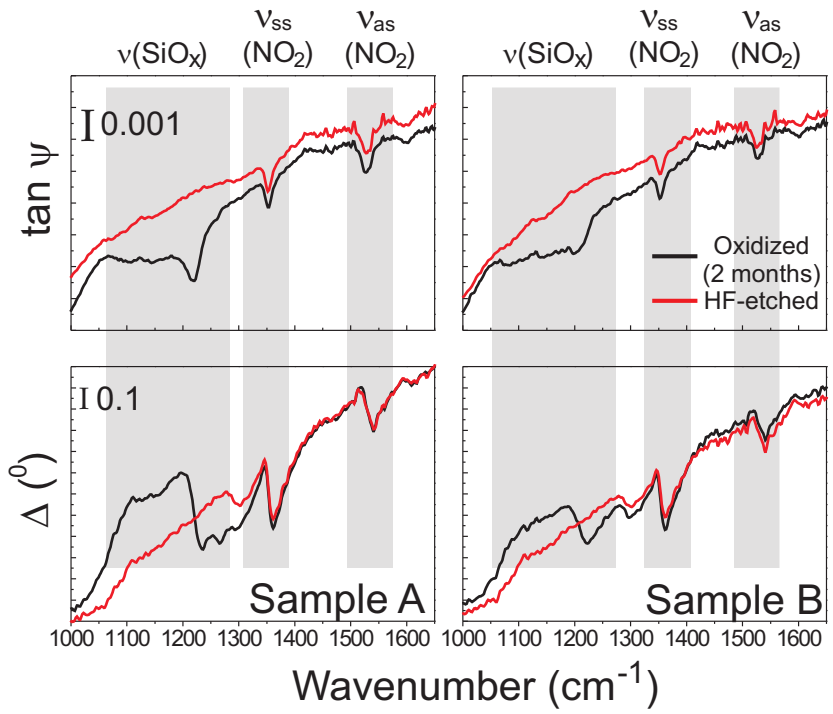

Figure 6.9: IRSE spectra of sample A prepared without addition of HF into electrolyte (left) and sample B prepared with addition of HF (right) after 2 months of oxidation under atmospheric conditions (black) and after a subsequent HF–treatment (red). The SiO_x – related absorption peak disappears in both cases upon HF–treatment, while NB-related peaks remain unchanged.

tion bands remained unchanged. In addition, appearance of the peak due to Si–H stretching vibration at 2082 cm^{-1} points out on hydrogen–termination of the available surface Si atoms. Similar results were obtained for bromobenzene grafted on chemically oxidized Si surface: HF–etching resulted in disappearance of the silicon oxide–related absorption peaks, while the bromobenzene absorption peaks remained nearly unchanged. Similar results were obtained for 1.5 years old samples of NB/Si, where the removal of oxide did not result in the removal of the organic layer (spectra not shown). HF–etching presumes an etch–back of the Si atoms, as was schematically shown earlier in Fig. 2.10. The obtained results however point out that the electrochemically grafted molecules are not etched together with the removed surface Si atom.

Allongue at al [165] performed similar experiments for bromobenzene grafted on Si surfaces. They reported however different results: upon HF–dip of a 6–

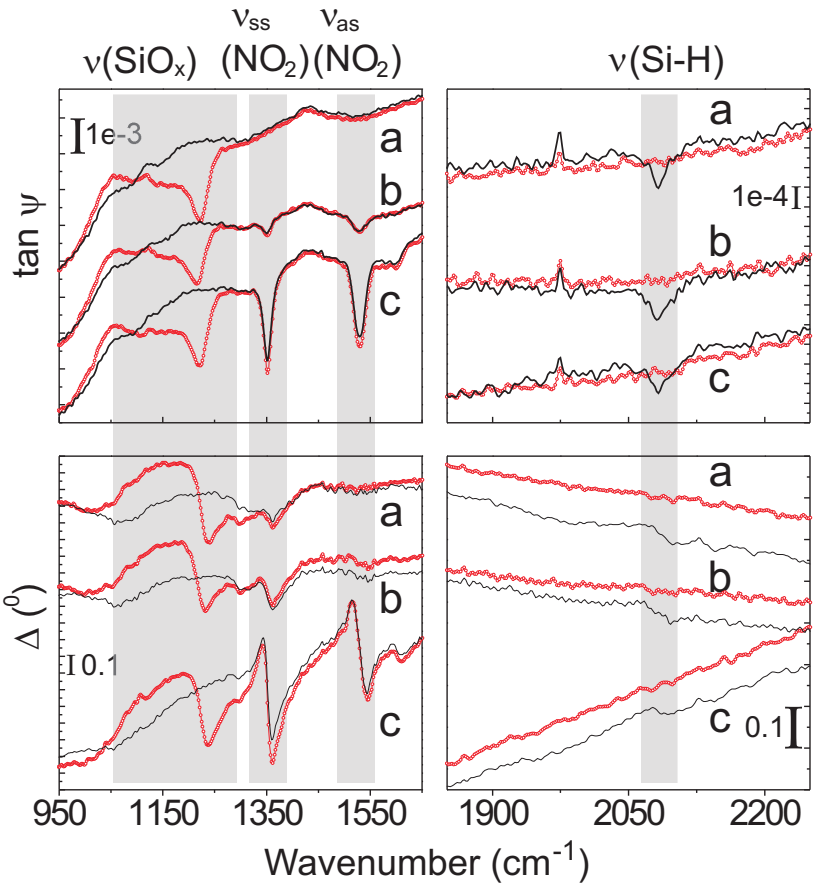

Figure 6.10: IRSE spectra of (a) chemically oxidized Si(111), (b) NB grafted during 110 sec and (c) NB grafted during 550 sec on chemically oxidized Si surfaces. Red: initial spectra after the preparation; black: spectra obtained after HF etch.

month old sample, the bromobenzene layer was etched away together with the underlying silicon oxide layer. They explained their results as follows: the oxidation starts from the defects in the organic layer and at the step edges of the Si surface, since the molecular grafting does not take place there [165]. The oxide starts to grow as islands, followed by a nucleation and eventually the complete layer formation. Removal of the complete oxide layer also removes the overlying molecules. Our results above however point out on a different situation: although the HF removes the oxide, the organic layer stays intact.

One of the possibilities is that attachment of the HF fluorine atom(s) to a Si surface atom leads to polarization of SiO_2 back bonds, upon which the Si atom becomes slightly positive, as shown schematically in Fig. 6.11. The grafted molecules of interest were nitrobenzene and bromobenzene, molecules of electron–acceptor type. The slightly positive and slightly negative ends of the attached molecule are indicated in Fig. 6.11. The positively–charged end of the phenyl ring may get repulsed from the Si atom, which becomes more positive upon attachment of fluorine atom(s). The organic molecule can rebind either to underlying less positive oxygen or silicon atoms. However, theoretical calculations similar to those performed in ref. [166] for simulations of HF interactions with oxidized Si surface are necessary in order to reveal the validity of this simple model.

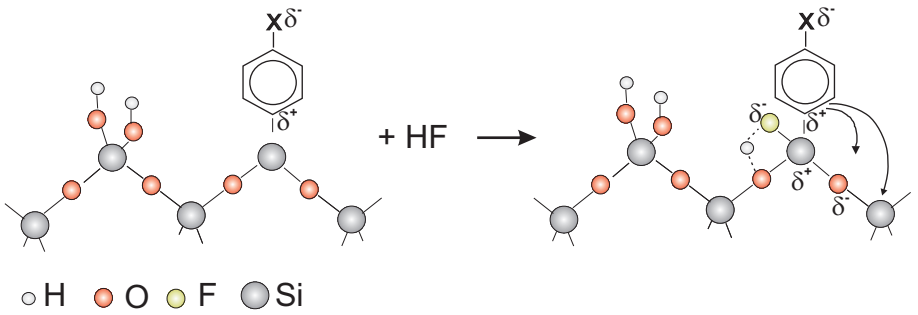

Figure 6.11: Schematic drawing of a possible scenario for reattachment of phenyl ring to slightly more negative atoms on a silicon surface. The arrow indicate possible re–attachment sites for the phenyl ring.

6.5 Summary

In this chapter we discussed the SiO_x interfaces that form between the organic films and the Si substrates as side reactions of electrochemical grafting and under atmospheric conditions. XPS techniques gave an insight into the sub–oxide structure of the Si surfaces. Using appropriate models, the thickness and coverage of the SiO_x interface were quantified.

It was shown that in general, addition of HF into electrolyte prevents formation of the oxidized silicon interface during the grafting. This was presented

by the absence of the SiO_x–related absorption peaks in the IRSE spectra. However, XPS spectra included the SiO_x peaks in the spectra obtained from the samples for which HF was added into the electrolyte. One possibility is that the post–grafting water rinsing of the samples induces the formation of this interface. However, there is also a possibility that grafting proceeds through the Si–O–C bonds, explaining the oxide peaks in the XPS measurements.

Another finding of this work was that oxidation under ambient conditions proceeds more slowly beneath the organic layer than on an unprotected silicon surface. We found out that under larger molecule (4–MDA), the oxidation is slowed down considerably, which is probably due to the steric hindrance of the molecule. This finding can be useful in design of electronic devices for protecting of silicon against oxidation.

It was also observed that HF etching of the organically modified surfaces with an underlying SiO_x interface removes the interface, but molecules remain on the surface. The possibility of the rebinding of the molecules to more negative surface atoms was discussed. Theoretical calculations are necessary in order to prove the validity of this simple model.

Chapter 7

X–ray induced reduction of nitrobenzene to aniline on Si(111) surfaces

In the previous chapters it was shown that electrochemistry leads to a successful functionalization of inorganic electrodes with organic thin films. Here, a process that converts the NO_2 nitro groups of electrochemically grafted nitrobenzene on Si surfaces into NH_2 amino groups is presented. Such conversion of nitro groups in aromatic compounds into amino species by *electrochemical* methods is a well–established procedure and has been reported in refs. [167, 168].

Recently, conversion of nitro groups to amino species by external irradiations using hard and soft X-rays [169, 170], electrons [171] and even visible laser light [172] has received considerable attention. This peculiar type of irradiation damage is usually an unwanted effect. Yet, it opens up new interesting technological perspectives in the case of the nitro-to-amino conversion, such as employing chemical lithography [171] by focused beams or shadow masks.

Laterally patterned surfaces in the micro- or even nanoscale regime can be prepared where the surface functional groups, NO_2 or NH_2, determine the local surface reactivity. Thereby connectivity to further functional units can be achieved. Such lateral chemical patterning by external irradiation has been demonstrated previously [171, 172].

A number of studies has dealt with the irradiation–induced nitro–to–amino conversion, and there is a consensus in the literature that electrons cause the NO_2 conversion. In the case of photon irradiation, the electrons generated in the photoemission process (i.e., photoelectrons and secondary electrons) trigger the conversion processes. As Moon et al. pointed out [170], the reaction cross-section is too large to be interpreted as a photocleavage reaction under non-resonant conditions. The details of the mechanism and chemistry of NO_2 conversion are still under investigation. Concerning the source of the hydrogen atoms or protons that are necessary for the conversion of NO_2 to NH_2, different

opinions prevail. Electron induced C-H bond splitting [171] as well as solvent or water remaining within or adsorbed on the organic layer [172] were quoted as likely sources of hydrogen. Concerning the effect of (soft) X-ray irradiation, the selective cleavage and complete desorption of the nitro group [169] instead of (mainly) chemical conversion [173] were reported.

Other non-consistent findings relate to the oxygen species. Whereas refs. [169, 170, 173] did not observe a decrease in the O1s core level for NO_2 reduction by X-rays, changes in the O1s core level induced by low-energy electron beam exposure were reported by Eck et al [171].

This chapter addresses those unresolved issues of the irradiation-induced nitro-to-amino conversion. High-resolution in situ studies of thin nitrobenzene layers irradiated with light from an undulator of a third generation synchrotron source at BESSY II was performed. The chemical conversion was monitored on-line by acquiring high-resolution X-ray photoelectron spectra.

The nitrogen-related emissions were analyzed by a detailed curve fitting, where the measured data were fitted into up to six individual components. In particular, shakeup satellites [174] were included in the data analysis and interpretation.

In order to have an insight into the time–dependent changes in the spectra, the deconvoluted integrated intensities as function of irradiation time t were plotted. These data were fitted with an equation of the type $A + B\exp(-t/\alpha)$. In this formula, A and B are constants, where B can be either positive or negative, depending on whether a certain component was growing or decaying, respectively. The exponential part includes t, which is the irradiation time, and α, the constant of the decay/growth of a certain component. Here, we report on the constant α for some of the processes involved in the modification of nitrobenzene during irradiation. The accuracy of the decay constant α is dependent on background subtraction, the quality of the fit, and the amount of data that was analyzed. Thus, the reported values of the decay constant α have an error bar of 25%.

Careful examination of the core level spectra of nitrobenzene monolayers grafted on the Si substrate allowed us to identify not only the NH_2 groups that resulted from the irradiation but a rather complex ensemble of amino-related species. A considerable oxidation of the supporting silicon substrate by oxygen released from the nitro groups was observed. Our measurements confirmed that no decrease in the overall C1s core level was induced by X-ray irradiation, in agreement with other authors [170, 173]. In the following sections, the results of simultaneous X-ray irradiation and photoelectron monitoring are described. The deconvoluted core level emissions and their assignments to the observed components is presented. Finally, the chemical processes that take place upon nitro-to-amino conversion is proposed, passing through the intermediate stages.

7.1 Overview of the X–ray irradiation induced changes on the observed core level spectra

Fig. 7.1 gives an overview of the irradiation-induced changes of a nitrobenzene layer grafted onto Si(111). The detailed spectra of the Si2p, C1s, N1s, and O1s

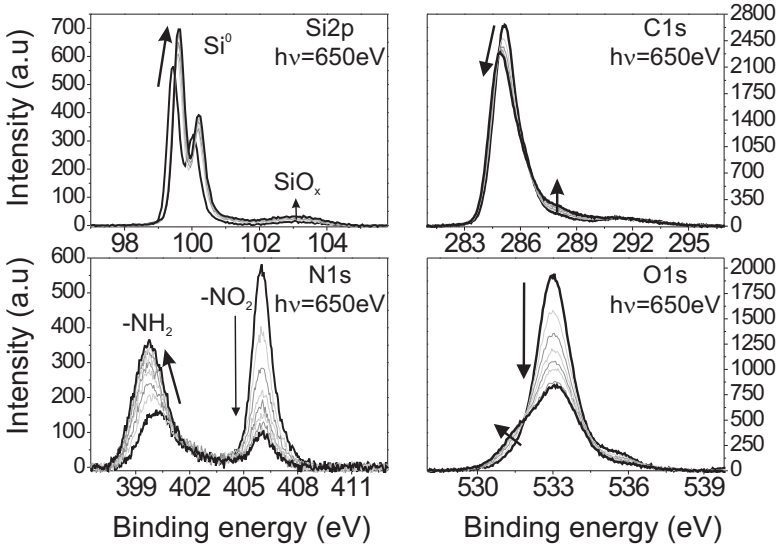

Figure 7.1: Development of the Si2p, C1s, N1s, and O1s core levels upon irradiation with hν=650 eV. The spectra series were obtained in 2 min intervals, within 20 min total. The arrows on each graph emphasize the irradiation-induced changes. Please note the scaling factors.

core levels are shown. They were obtained sequentially within 20 min of irradiation/observation time at an excitation energy of 650 eV. The N1s line exhibits the NO_2–related emission at a binding energy of about 406 eV, which quickly decays upon irradiation. On the other hand, the amino-related emission at about 400 eV increased with time. In contrast to earlier studies [173] significant changes were observed within the O1s core level: the dominating emission at 533 eV decayed in intensity, and the evolution of a distinct shoulder at 531.5 eV indicates the formation of a new chemical species. The irradiation-induced changes of the C1s emission are comparatively subtle, nonetheless significant. The main emission at 285 eV is slightly reduced in intensity, which is compensated by an increase in emission intensity around 288 eV. The overall C1s emission intensity, however, remains unchanged, as the detailed core level analysis by curve fitting will confirm. The Si2p emission shows the Si^0 doublet emission from elemental bulk silicon at 99.24 eV (Si2p3/2, 0 min). In the course of the irradiation, the Si

2p emission increases in intensity and shifts continuously toward higher binding energies. This energetic shift is presumably related to an increase in the surface band bending (the silicon substrate is p–type doped), which is brought about by the secondary electron irradiation [175, 176] The Si2p region contains also emissions from silicon (sub)oxide species SiOx around 103 eV, which apparently exist at the interface with the electrografted nitrobenzene layer. The irradiation-induced binding energy shift toward higher energy was detected for both the bulk Si^0 and the oxide Si^{+x} components, where Si^{+x} denotes the (intermediate) oxidation states with Si bonded to x oxygen atoms.

To obtain a better insight into the silicon/nitrobenzene interface structure, the Si2p core level was monitored in a separate experiment run on a pristine, non-irradiated surface spot by excitation with hν=240 eV photon energy. These spectra were used for the data analysis of the Si2p core level rather than those obtained with hν=650 eV photon energy due to a higher surface sensitivity. Figure 7.2 shows Si2p spectra obtained sequentially within 26 min, where the changes in the Si^{+0} and Si^{+x} components are emphasized by the arrows. Because

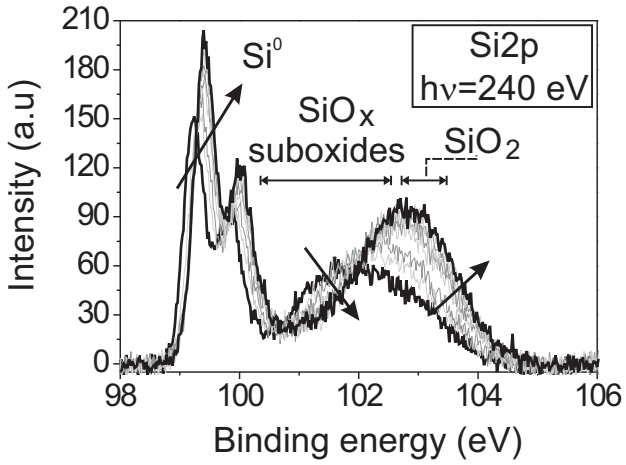

Figure 7.2: Development of the Si2p core level upon irradiation with hν=240 eV. The spectra series were obtained in 2 min intervals, within 26 min total. The arrows on each graph emphasize the irradiation induced changes.

of the higher surface sensitivity, the relative intensity of the SiO_x related emissions is now much higher. The center of gravity of the (sub)oxide species shifts from about 102 to 103 eV, which is much higher than the band bending change (0.3 eV) monitored by the Si^0 emission. This shift is interpreted as an increase in the oxidation state (chemical shift). Interfacial silicon suboxides SiO_x undergo a transition to fully oxidized silicon oxide SiO_2 during irradiation. The

increase of the Si^0 and SiO_x intensities indicates a reduction of the density of the organic layer. All core level spectra in Figures 7.1 and 7.2 were thoroughly analyzed by curve fitting. The results of these detailed studies will be presented in the following sections, in the order N1s, C1s, O1s, and Si 2p.

7.2 Deconvolution of the N1s core level

The N1s core level was fitted using six components, labeled N1 to N6. Fig. 7.3 displays the fits of the first spectrum, describing the chemical state of the pristine as–deposited surface, and after 1200 s of irradiation, representing a largely converted surface containing mainly amino-related species. The fitting parameters for all six components are given in Table 7.1.

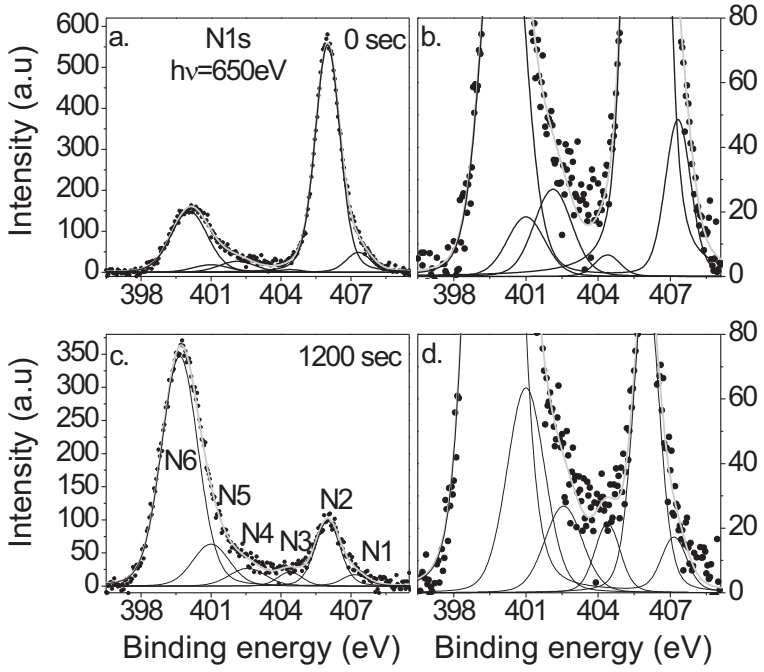

Figure 7.3: N1s core level spectra obtained at a photon energy of 650 eV. (a and b) Spectrum obtained in the first scan and (c and d) spectrum after 1200 s exposure to X-rays. (b and d) Enlargement of panels a and c, respectively. The components labeled N1 to N6 are shown in panel c and are discussed in the text.

Fig. 7.4 shows the temporal evolution of the integrated intensities of these components. The component N2 is centered at 406.0 eV and is related to the

N1s components	Assignment	BE (eV)	Gaussian width (eV)
N1	π-π^* shake–up [177]	407–407.3	1.1
N2	NO_2	406.0	1.1
N3	π-π^* shake–up [178]	404.4	1.1
N4	protonated imine N^+H [179, 180] or diazonium $–N_2{}^+H$ [181]	402.1–402.6	1.7
N5	nitroso (solid) –N=O [182] or protonated amine $N^{+\bullet}H$ [180]	401	1.7
N6	NH_2 neutral amine [180, 183]	400–399.7	1.7

Table 7.1: Fitting parameters of binding energy (BE) and Gaussian width FWHM for components N1 to N6 (as defined in Fig. 7.3 (c)). Lorentzian FWHM was 0.135 eV for all N1s components [184]. Components were allowed to vary during the fit in the range shown in the table. N4 and N5 components are also in the range of the N=O–related signal in nitrosobenzene (401.6 eV in solid nitrosobenzene) [182].

nitrogen in the NO_2 group of the grafted NB molecules. This peak diminished substantially during exposure to the X-rays. The asymmetry of the amino-related emission line at 400 eV necessitated the fitting into the two components N5 and N6. These components grow during the X-ray exposure time. The component N6 is centered around 400.0 eV, but it gradually shifts toward 399.7 eV during the irradiation. The component N5 was fixed at 401.0 eV during the fits. The binding energy of N5 is close to the one reported by Kumar et al. [179] for the positively charged nitrogen species in polyaniline (400.8 eV), as well as to that of solid nitrosobenzene, H_6C_5–N=O, which was reported at 401.6 eV [182]. Reduction of nitrobenzene that involves the nitrosobenzene intermediate state was also reported in ferric oxide suspensions [185] and through electrochemical reduction [167,168] with the aniline as the final product. The N1 component at around 407 eV is attributed to the N1s shakeup satellite in nitrobenzene [177]. This is supported by the fact that it decays with a rate similar to that of the nitrobenzene related component N2 at 406.0 eV. The position of this shakeup satellite was observed at a lower BE than reported in the literature for gas phase nitrobenzene [177]. According to Distefano et al. [177], the shakeup band in the N1s core level has about 2 eV separation from the main N1s peak due to the NO_2 group, while in our case, a separation of only about 1 eV was found. This discrepancy is probably due to the different chemical environment of our molecules, which are polymerized $C_6H_4NO_2$ units in a solid layer [186, 187] instead of isolated gas phase species. Both the N3 and the N4 components show a more complex behavior: there is an initial increase in their integrated intensities and a subsequent decrease. The integrated intensities of these components were very low, and difficulties arose in the background subtraction as well as in the peak fitting process itself. The N3 component is attributed to a shakeup process in aminobenzene (aniline) [178] The N4 component may be related either

to a positively charged imine species [179, 180] or to $-N_2^+$ diazonium residuals [181]. It should be mentioned, however, that no diazonium residuals were detected previously after similar grafting of aryldiazonium salts on various substrates [181, 188, 189, 187]. The decay of the N3 and N4 peaks that occurs after about 150 s of irradiation might be due either to conversion of these species further to aminobenzene or to desorption of the nitrogen in these species from the surface.

7.2.1 Dynamics of the integrated intensities

An overall nitrogen loss from the system was detected during the irradiation, as can be seen from Fig. 7.4. There, the total N1s plot stands for the sum of

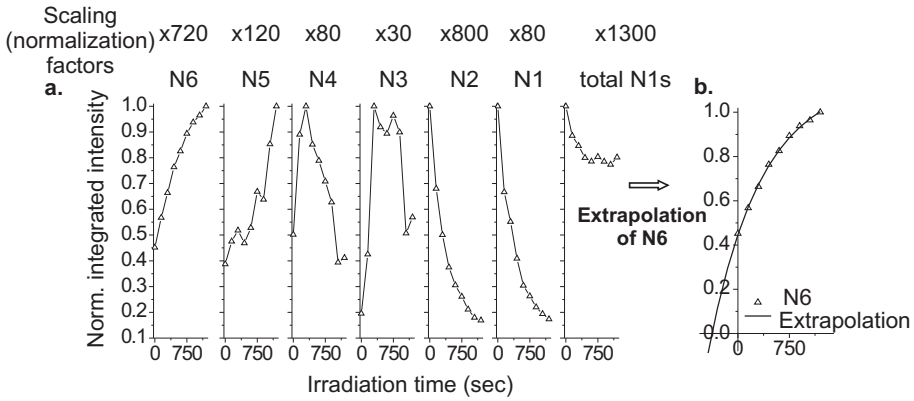

Figure 7.4: (a) Normalized integrated intensity (peak area) of the N1s core level components as a function of irradiation duration. (b) Extrapolation of N6 component to zero intensity. Please note the scaling factors.

the components N1 to N6. Loss of about 20% in nitrogen was observed after around 450 s of irradiation. After this time, the total N1s intensity seems to saturate. For comparison, Mendes et al. [173] reported a decrease of 18% after 447 min in aromatic NO_2-containing self-assembled monolayers, using a laboratory MgKα source (1253.6 eV). The much faster progress of nitro reduction in our experiment is due to the orders of magnitude higher photon flux. In contrast to La et al [169], the 100% bond cleavage and desorption of NO_2 groups upon synchrotron irradiation with hν=550 eV was not observed in this work. Fitting of the growth and decay constants showed that the growth rate of NH_2-related peak N6 and the decay rate of NO_2–related peak N2 were different. It was found that the decay constant α of the N2 component was about 350 s, while the growth constant of the N6 component was about 800 s. However, the decay constant of the sum of components N6 + N5 + N4 +N3, situated at lower energy to the NO_2–related N2 component, was 480 s, which is closer to

the decay constant α of the N2 (350 s) peak than the decay constant of the N6 peak alone (800 s). This again supports the argument that the NB molecules decompose to additional species and that the reduction to aniline is not a single-product process. The remaining gap between the growth constant of the sum of the components N6 + N5 + N4+ N5 (480 s) and the decay constant of the NB–related N2 and N1 peaks (350 s) is due to the partial detachment of the N atoms from the surface. Finally, it should be commented on the emissions from reduced nitrogen species (N5 and N6) that were already present in the first monitoring spectra. It is clear from Fig. 7.4 that these emissions do not result from an insufficient time resolution but exist already on the as–received, non–irradiated surface. The N1s spectrum was collected first and required less than 60 s. Extrapolating the N6 emission to zero intensity (Fig. 7.4 (b)) shows that it would require an irradiation time of about 380 s for these reduced species to evolve. Thus, it can be concluded that the amino-related species were present already on a pristine surface and were introduced probably by the amino compounds that serve as the precursors for the aryl diazonium salts from which the nitrobenzene was electrochemically grafted onto the surface. The interpretation as a contaminant was supported by ref [186], where amino–type emissions also had been observed for electrochemically grafted bromobenzene layers. As a second possibility, the electrochemical grafting process itself may have been accompanied by an electrochemical reduction of NO_2 as a side reaction, as pointed out by Allongue et al. [190].

7.3 Deconvolution of the C1s core level

The C1s core level was fitted using six components (Fig. 7.5). A summary of fitting parameters for all six components is shown in Table 7.2.

The main peak C1 was initially centered at 285.1 eV and shifted gradually toward a lower binding energy at longer exposure time to X-rays. The energetic separation of component C2 from C1 was 1.2 eV (at 0 s) and was found to gradually diminish to about 1.0 eV. These two main peaks are caused by the carbon atoms in the benzene ring [191, 192] where the C1 peak at the lowest energy is due to neutral C-C or C-H bonds and the C2 peak is due to the carbon on the benzene ring bonded to the nitrogen atom. The growing C2 peak has roughly a similar constant α (200 s) as compared to the decay constant of the C1 peak (170 s). The binding energy of the carbon bonded to a N atom in gas phase aniline was reported to be 291.29 eV and 292.09 eV in gas phase nitrobenzene [192]. Thus, the difference in the binding energy of carbon nonbonded to N and bonded to N is about 1.3 eV in aniline and about 0.95 eV in nitrobenzene. An analogue asymmetry in the C1s core level was also reported for aniline adsorbed on Ag(110), [196] where the separation in the binding energy for carbon nonbonded to N and bonded to N was 1.0 eV. Consequently, the increasing C2 component separated by about 1 eV from the main C1 peak is attributed to carbon atoms bonded to nitrogen atoms in either nitrobenzene or aniline-like species. An increase in intensity of the C2 component as a function of the irra-

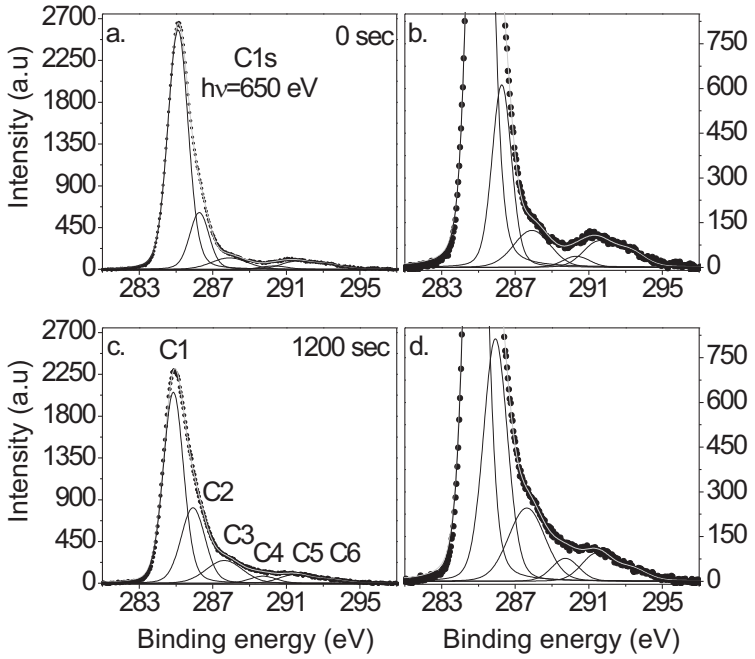

Figure 7.5: C1s core level spectra obtained at 650 eV photon energy. (a and b) Spectrum obtained during the initial irradiation and (c and d) spectrum after 1200 s. exposure to X–rays. (b and d) Enlargement of panels a and c, respectively. Components C1 to C6 are shown in panel c and are discussed in the text.

diation time thus suggests an increase in the number of the ring carbon atoms bonded to nitrogen (i.e., through polymerization, [197, 198, 199]. The gradual shift of the C1 component toward lower binding energies can be explained as a gradual reduction of nitrobenzene to aminecontaining species. For instance, the average observed energy for the benzene carbon atoms nonbonded to N atoms was reported to be 290 eV in aniline, while in NB, this value was 291.1 eV in the gas phase [192]; thus, the shift of the peak due to carbons at the benzene ring toward lower energies was expected upon reduction of nitrobenzene. The C3 component was separated from the C1 peak by 2.8 eV and is possibly due to bonding to positively charged amine groups [179]. C4 is separated from C1 by about 4.9 eV and is attributed to a shakeup π–π^* satellite characteristic of aniline [178, 194]. The growth constant α of the C4 component (1770 s) is close to the growth constant of the sum of amino-related components N5 + N6 (1600 s), supporting assignment of the C4 component as related to the shakeup

C1s components	Assignment	BE (eV)	Gaussian width (eV)
C1	carbon in benzene ring nonbonded to nitrogen [180, 187, 191, 192]	285.1–284.9	1.16
C2	carbon in benzene ring bonded to nitrogen [180, 187, 192]	286.3–285.9	1.1–1.43
C3	carbon in benzene ring bonded to NH^+ [179, 193]	287.9–287.6	2.2
C4	π–π^* shake–up satellite in aniline [194]	290.3–289.7	1.6
C5	π–π^* shake–up satellite in benzene [194, 195]	291.5–291.3	1.8
C6	π–π^* shake–up satellite in benzene [194, 195]	293.1–293.3	1.8

Table 7.2: Fitting parameters of binding energy (BE) and Gaussian width FWHM for components C1 to C6 (as defined in Fig. 7.5 (c)). Lorentzian FWHM was 0.125 eV for all C1s components [184]. Components were allowed to vary during the fit in the range shown in the table.

process at the benzene rings bonded to the amino groups. The components C5 and C6 are related to shakeup π–π^* transitions at the benzene ring, which are characteristic for benzene [195] and were also observed in both nitrobenzene and aniline [194]. The occurrence of these peaks is thus indicative of the integrity of the benzene ring during the investigation.

7.3.1 Dynamics of the integrated intensities

Fig. 7.6 shows a plot of the integrated intensities of the C1s deconvoluted emission peaks. The sum of the C1s components (total C1s in Fig. 7.6) shows no significant change as a function of irradiation time. Thus, no desorption of phenyl units or smaller carbonaceous fragments from the surface was observed. The sum of the C5 and C6 components, related to π-π^* shakeup satellites of the benzene ring, also shows no change in intensity: this indicates that the aromatic rings remain intact during the irradiation. The irradiation affects a change of the line shape of the C1s emission: a reduction of the C1 intensity and growth of the C2, C3, and C4 peaks during the irradiation process were found.

7.4 Deconvolution of the O1s core level

The O1s core level was fitted using four components (Fig. 7.7). A summary of the fitting parameters for all four components is shown in Table 7.3.

The main peak O2 was centered at 533.0 eV and is related to oxygen from the nitro group of the NB molecule [187]. The O4 component is related to a shakeup

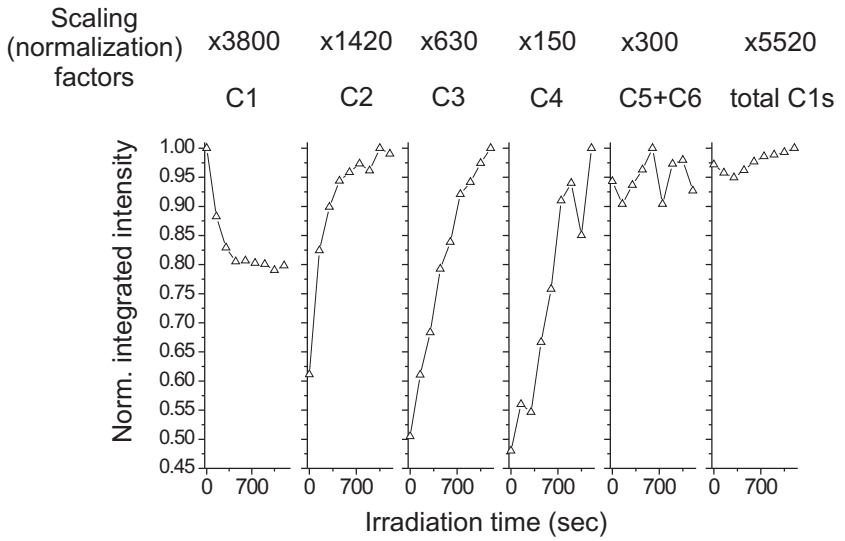

Figure 7.6: C1s normalized integrated intensity plots as a function of irradiation duration. The sum of C5 and C6 corresponds to integrated intensities of the shakeup satellite related components. Total C1s is the sum of all C1s integrated intensities in fitted peaks.

O1s components	Assignment	BE (eV)	Gaussian width (eV)
O1	LBC (SiO_2) Si–O–Si [200, 201, 202]	531.4–531.7	0.68–1.32
O2	$C_6H_5NO_2$ [187]	533.0	1.32
O3	nitrosobenzene N=O [203]	534–534.1	1.37–1.42
O4	π–π^* ($C_6H_5NO_2$) [177]	535.5–536	1.2

Table 7.3: Fitting parameters of binding energy (BE) and Gaussian width FWHM for components O1 to O4 (as defined in Fig. 7.7 (c)). Lorentzian width was 0.2 eV for all O1s components [204]. Binding energies of the components varied during the fit in the range shown in the table. Possible contribution from nitroso groups N=O would be within the range of the components O2 and O3 (532.6-534.1 eV in solid nitrosobenzene [182, 203]). HBC component of interfacial SiO_x would be expected within the O2 component [200, 201].

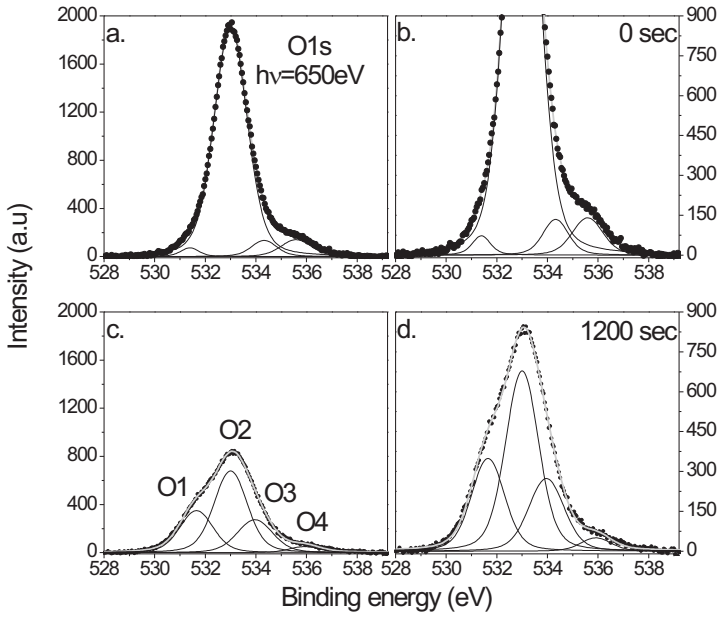

Figure 7.7: O1s core level spectra obtained at 650 eV photon energy. (a and b) Spectrum obtained during the initial irradiation and (c and d) spectrum after 1200 s exposure to X-rays. (b and d) Enlargement of panels a and c, respectively. Components O1 to O4 are shown in panel c and are discussed in the text.

process in the NB molecule [177]. The component O1 is generally related as a lower binding energy component (LBC [200]) and is characteristic for fully Si coordinated, Si-O-Si bridge bonded oxygen on oxidized Si surfaces [200, 205, 201, 202]. In the initial stages of irradiation, this peak was fitted with 1.58 eV separation from the main peak, but for fitting of the successive data, it was positioned at about 1.32 eV separation from the main peak. Initially, the Gaussian FWHM of the O1 component was 0.68 eV, but already after 150 s of irradiation, the FWHM value was 1.25 eV and increased gradually at longer exposure to X–ray irradiation. The component O3 shifted gradually toward a lower binding energy as the exposure to X-ray irradiation continued. The Gaussian FWHM was kept constant at 1.42 eV, except in the data from the initial exposure, where the best fit was achieved for a FWHM of 1.37 eV. The assignment of O3 is not straightforward: on one hand, O3 could be related to the higher binding energy component (HBC [200]) of surface silicon oxide and is attributed to oxygen in Si–O configurations [200, 205, 201, 202]. However, the

observed O1-O3 separation was around 2.4 eV, whereas the HBC-LBC energy separation was consistently reported to be 1.4 eV [205, 201, 202]. Thus, we do not assign O3 to a silicon oxide or hydroxide species. A possible assignment for the O3 component could be intermediate nitrobenzene reduction states such as nitrosobenzene. The BE values for the O1s emission of aromatic nitroso compounds reported in the literature vary considerably from 532.6 [182] to 534.1 eV [203]. Further support for this assignment will be given in section 7.6.

7.4.1 Dynamics of the integrated intensities

Fig 7.8 shows the integrated intensities for the O1s components. From Fig. 7.8

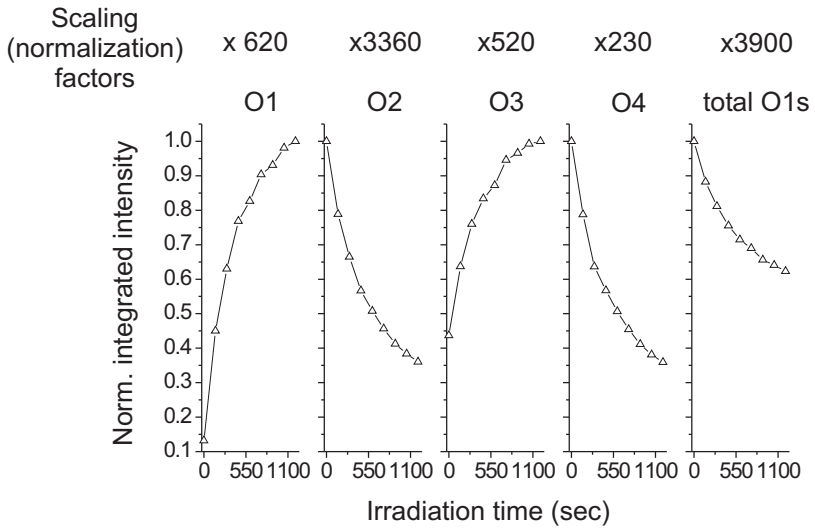

Figure 7.8: Normalized integrated intensity plot of the O1s emission components as a function of irradiation duration. O1, O2, O3, and O4 components are as shown in Fig. 7.7 (c). Please note the scaling factors.

, it is evident that there is an overall loss of oxygen from the surface (total O1s). This oxygen is released from the NO_2 groups of the NB molecules and mostly desorbs into the vacuum during the irradiation process. Part of the oxygen that leaves the NB molecules, however, participates in an oxidation of the Si substrate since the O1 component that is related to LBC on the Si substrate increases considerably. The growth constant α of the O1 and O3 peaks is similar and equal to about 400 s. This constant also correlates well with the decay constant of the NO_2– related O2 component (450 s), implying that upon irradiation–induced cleavage from the NO_2 group, a part of the released oxygen incorporated into the interfacial SiO_x layer. The O4 component, related to the shakeup process in the NB molecule, decreases with the same constant α (450 s) as the main NB–related O2 component, supporting the assignments of both

the O4 and the O2 components as related to the NO_2 group in nitrobenzene. Remnants of the solvent (i.e., water) incorporated into the solid nitrobenzene layer would exhibit an emission around 533 eV [123, 124, 125] (i.e., they would overlap with the NO_2–related emission O2). The parallel decay of O_2 and the NO_2 shakeup structure O4 indicates, however, that the contribution of H_2O to the total O2 signal must be uninfluenced by irradiation. For comparison, the observed decay constant α for the NO_2-related N2 component was 350 s. These decay constants appear to be close within the error bar of α. These results suggest that the O2 and N2 components are correlated and that both result from the decomposition of the NO_2 group in the NB molecules.

7.5 Deconvolution of the Si2p core level and dynamics of the integrated intensities

The Si2p core level was fitted using five components (Fig. 7.9). A summary of fitting parameters for all five components is given in Table 7.4. The silicon

Si2p components	BE (eV)	Gaussian width (eV)
Si^0	99.24–99.41	0.37–0.38
Si^{+1}	Si^0 + 0.97	0.8
Si^{+2}	Si^0 + 2.1	0.8
Si^{+3}	Si^0 + 2.7	0.8
Si^{+4}	Si^0 + 3.5	1.1

Table 7.4: Fitting parameters of binding energy (BE) and Gaussian width FWHM for components Si^{+0} to Si^{+4} (as defined in Fig. 7.9 (c)). Lorentzian width was 0.055 eV for all Si2p components [74]. For the Si2p core level, spin-orbit splitting was fixed at 0.605 eV, and the branching ratio was set to 0.52. Components were allowed to vary during the fit in the range shown in the table. For assignments and fitting, parameters similar to those reported earlier in refs. [90, 206, 207] were used.

bulk peak Si^0 shifted toward a higher binding energy during the irradiation, from 99.24 to 99.41 eV. The other components related to Si atoms in (intermediate) oxidation states (Si^{+1} to Si^{+4} components) were fixed at certain relative energies from the Si^0 component as shown in Table 7.4. Fig. 7.10 shows integrated intensities as a function of irradiation time for the Si^0 to Si^{+4} components, as well as the sum of the Si^{+1}, Si^{+2}, Si^{+3}, and Si^{+4} components.

There is a slow growth of the Si^0 component, which is due to the continuous decrease of the density of the organic layer through nitrogen and oxide desorption. Taking an electron inelastic mean free path of 0.9 nm for the Si2p photoelectrons in organic matter [99], an equivalent effective thickness decrease of 0.3 nm over the total irradiation time can be estimated. There is a slight increase in the amount of the Si^{+1} intermediate oxidation state. The Si^{+2} intermediate

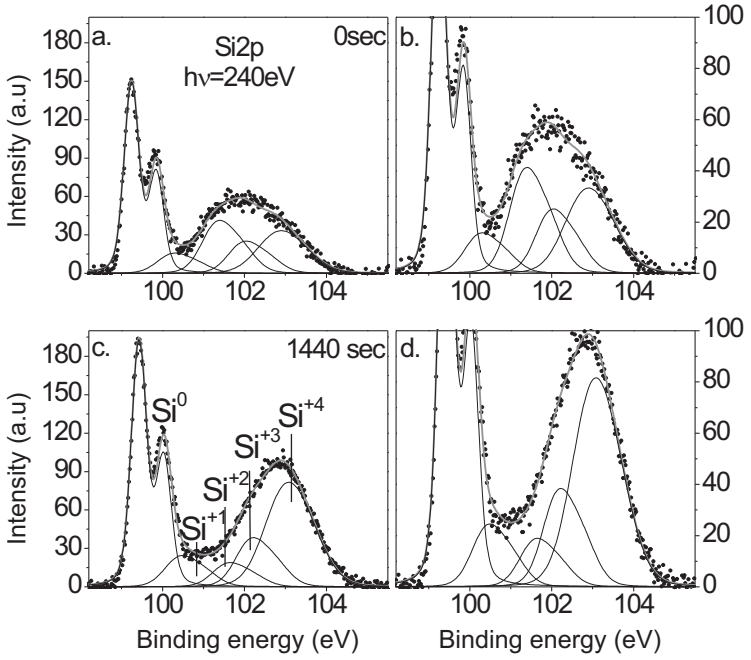

Figure 7.9: Si2p core level spectra obtained at 240 eV photon energy. (a and b) Spectrum obtained during the initial irradiation and (c and d) spectrum after 1440 s exposure to X–rays. (b and d) Enlargement of panels a and c, respectively. Components Si^0, Si^{+1}, Si^{+2}, Si^{+3}, and Si^{+4} are shown in panel c and are discussed in the text.

state is an energetically unfavorable state for the oxidation of Si(111) [208], and it decays substantially with increasing irradiation time. At the same time, the Si^{+3} component is initially growing, but after about 480 s of irradiation, the intensity of this component decreases. The Si^{+4} component is continuously increasing as a function of the irradiation time. The growth constant of the sum of all oxidation states Si^{+x} (total Si^{+x} in Fig. 7.10) is close to that of the O1s LBC component (about 400 s). Taking all the individual changes together, the line shape change of the Si 2p emission is to be described as a transition from intermediate oxidation states (suboxides) to the fully oxidized state, SiO_2. As the intensity ratio between the (partially) oxidized (total Si^{+x}) and the bulk Si^0 emission does not significantly change, the thickness of the interfacial (sub)oxide layer remains relatively constant. Its effective thickness was approximately 0.3 nm.

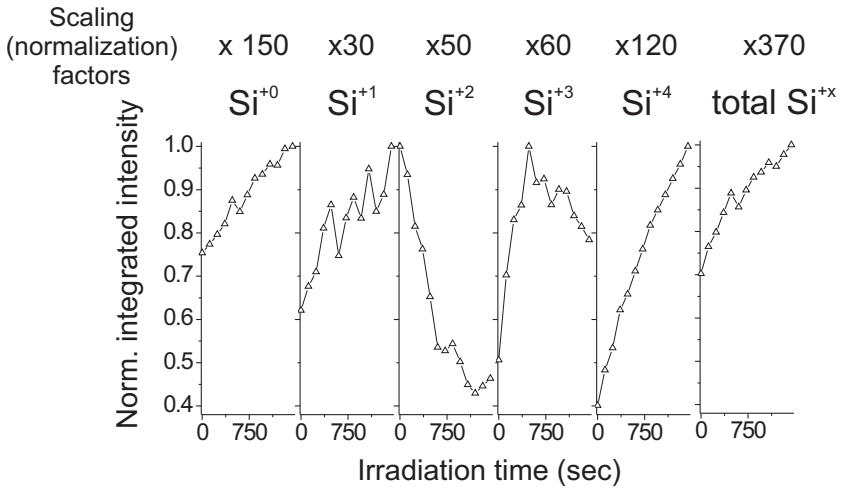

Figure 7.10: Normalized integrated intensities of the silicon components as a function of irradiation time. Data are normalized to the highest integrated intensity in each data set. Please note the scaling factors.

7.6 Discussion

A careful fitting of the X-ray photoelectron spectra allowed us to follow in detail the complicated process of nitrobenzene reduction upon X-ray irradiation. From the N1s core level, we could conclude that during the irradiation not only a chemical reduction takes place but also a partial desorption of nitrogen-containing species. The appearance of the N5, N4, and N3 peaks, which are positioned at higher binding energies than the uncharged aniline-related N6, proposes that several chemical species with a higher local charge at the nitrogen core than in a neutral amine–like environment have been created. The protonated or positively charged amino groups –NH^+–Ph can be generated either in a molecular aminobenzene–like or a polymerized polyaniline-like state.

Development of the nitroso groups during this process can be concluded from cross-referencing the studies from N1s and O1s core levels. We tentatively assign the component O3 to nitrosobenzene or hydroxylamino–like environments. The similarity of the irradiation–induced nitrobenzene reduction to the electrochemical reduction process as illustrated in Fig. 7.11 suggests that these intermediate states might be formed. The binding energies of N1s and O1s for aromatic nitroso compounds reported in the literature exhibit a considerable scatter, but a trustworthy reference experiment was reported by Batich and Donald [203], which reported 400.3 eV for the N1s and 534.1 eV for the respective O1s emission. Thus, identifying O3 with emission from –N=O or –NH–OH environments, the corresponding N1s signal would overlap with N6 (or N5). Identifying O2 with –NO_2, and O3 with –N=O or NHOH only, it can be estimated that 10–20%

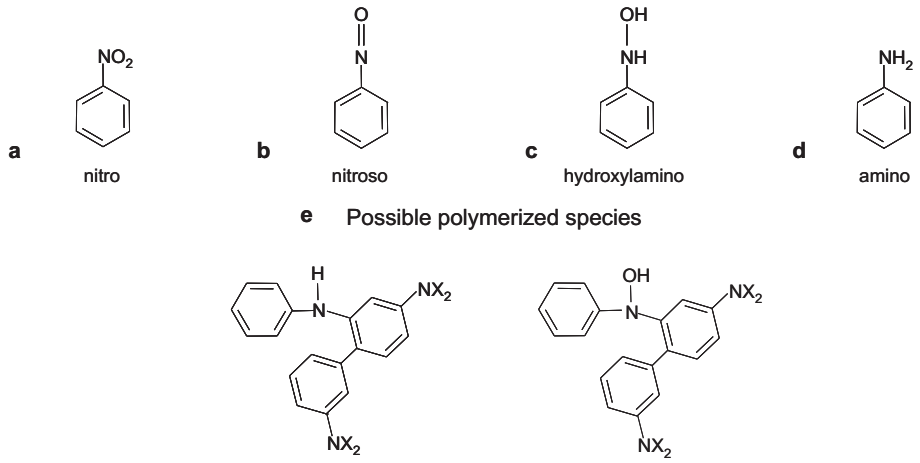

Figure 7.11: Comparative representation of the electrochemical reduction series from nitrobenzene (a) to aminobenzene (d) with intermediate states of nitrosobenzene (b) and phenylhydroxylamine (c) and suggestions for possible polymerized species (e).

of the initially present NO_2 groups was converted into the intermediate nitroso– or hydroxylamino–like environment after 1200 s irradiation.

Cross-referencing the Si2p and O1s core level data, we conclude that upon irradiation-induced cleavage from the NO_2 group, a part of the released oxygen is incorporated into the interfacial SiO_x layer. As a consequence, the initially prevailing suboxide species Si^{+1}, Si^{+2}, and Si^{+3} are further oxidized, and Si^{+4} (SiO_2) becomes the dominating chemical species. Fitting of the C1s core level indicated that the benzene rings themselves do not detach from the surface and do not decompose during irradiation. An increase in intensity of the C2 component, attributed to carbon atoms bonded to nitrogen atoms in either nitrobenzene or aniline-like species, suggests an increase in the number of the ring carbon atoms bonded to nitrogen. We interpret this increase as a polymerization process of benzene rings through nitrogen-containing bridges.

The reduction and polymerization processes are illustrated in Fig. 7.11 and were derived in analogy to the electrochemical reduction process (Fig. 7.11 a-d) [167, 168]. Intermediate states of nitrosobenzene (H_5C_6–N=O) and phenylhydroxylamine (H_5C_6-NH-OH) are formed during the electrochemical reduction process of nitrobenzene to aminobenzene (aniline) [167,168,185]. In the electrochemical series, this process is achieved via the supply of electrons and protons. During the irradiation-induced reduction of nitrobenzene, electrons are supplied via the secondary electron current through the nitrobenzene thin film; however, the source of hydrogen to convert from nitrobenzene to aminobenzene is obscure. In other studies, the electron–induced hydrogen–carbon bond splitting was cited as the origin of the hydrogen for the nitro–to–amino conversion. Sim-

ilarly, we believe that it is hydrogen from the phenyl rings that is the source of the amine-like coordination of the reduced nitrogen species; however, we suggest an electron–induced polymerization process as depicted in Fig. 7.11e rather than a three-step process like C–H bond splitting followed by –N–O bond splitting and –H capture for the N–H bond formation

7.7 Summary

In this work, we investigated the effects of synchrotron irradiation on a nitrobenzene film grafted electrochemically on a Si(111) surface. In agreement with earlier reports, we observe an irradiation-induced reduction of nitrobenzene to an aminobenzene–like compound. This process can be employed for the purpose of chemical lithography.

A detailed study of the chemical conversion process by acquiring time–dependent spectra, by careful fitting of the high–resolution spectra, and by calculation of the related decay and growth constants was presented. The photon irradiation-induced secondary electron current modifies the surface layer by a reduction of nitrobenzene. The irradiation-induced reduction of nitrobenzene is accompanied by a partial desorption (about 25%) of nitro groups. Oxygen atoms that were freed from the remaining nitro groups were observed to oxidize the silicon substrate and to convert the initially present suboxide into fully oxidized SiO_2.

The irradiation-induced reduction of NB is not a single-product process, as a variety of reduced nitrogen species was observed. The main components are neutral and positively charged protonated amine groups. Indications of a polymerization of the benzene ring were found, and generally, the spectral features comply with those reported in the literature for polyaniline [179].

Intermediate reduction states in a nitroso or hydroxylamino-like environment were observed. The polymerization through attachment of the nitrogen to the benzene rings [197, 198, 199] explains the hydrogen source for the creation of the amine-like environment. There was no evidence for participation of water solvent remnants in the chemical conversion process as claimed by others. The carbon density remained constant during the irradiation-induced NB reduction. Benzene rings did not detach or decompose during the X-ray irradiation, as indicated by the persistence of the benzene-ring-related π-π^* shakeup satellites.

To conclude, detailed studies of irradiation induced damage of organic nitrobenzene layer on a Si(111) substrate were performed. We proposed a reduction scheme of nitrobenzene to amino-related species. Understanding of this process will allow for further developments in chemical lithography and micropatterning of hybrid organic/inorganic surfaces.

Chapter 8

Concluding remarks

In this work, structural characterization of organically modified metallic and semiconducting surfaces and interfaces was carried out. The characterization was performed using surface sensitive techniques, such as infrared spectroscopic ellipsometry (IRSE), atomic force microscopy (AFM), X-ray photoelectron spectroscopy (XPS) and VIS-ellipsometry. Cross correlated studies employing those experimental methods allowed to determine the influences of the electrochemical preparation conditions on thin films and interfaces properties, and to improve them accordingly. Our investigations revealed a successful modification of surfaces with nitrobenzene, bromobenzene, methoxybenzene and 4–methoxydiphenyl amine thin films through the electrochemical reduction of benzenediazonium salts. It was shown that grafting from the Grignard compounds on porous silicon led to termination with CH_3 and CD_3 groups.

Spectra obtained using IRSE techniques enabled a direct observation of surface chemical composition at a sub–monolayer regime. For instance, it enabled to observe the degradation of the hydrogen passivated silicon surfaces (section 6.1), to explore the structural properties of grafted organic thin films (sections 5.2, 5.3 and 5.4) and to study the interfacial properties of the samples (sections 6.2 and 6.4). Combination with other techniques, such as XPS and VIS–ellipsometry was important for independent determination of the thicknesses and optical properties of thin organic layers. Based on these observations, conclusions on side reactions during the preparation, passivation behavior, stability and structure of the organic thin films were drawn.

Cross correlated analysis using IRSE and XPS enabled to quantify also the properties of the silicon oxide interfaces. In particular, XPS studies provided the discrimination between the silicon sub–oxides (Si^0.. Si^{+4}). Using appropriate models, the SiO_x coverage and thickness in differently prepared surfaces, i.e. with and without HF in the electrolyte were quantified. The main finding was that an almost complete SiO_x layer forms at the silicon/organic film interface in the electrolyte when HF was not added to the electrolyte, while addition of HF was found to generally prevent the interface oxidation. However, when HF was added to the electrolyte, the XPS results pointed out a low coverage of the

interfacial SiO_x, while no absorption bands due to SiO_x were observed in the IRSE spectra. This small discrepancy between the XPS and IRSE results was argumented by additional possible oxidation processes that may take place during the XPS measurements. First, XPS triggers the reduction of nitrobenzene upon which the released oxygen can participate in the interface oxidation. Second, the oxidation could be triggered through the residual water in the organic layer from the grafting in aqueous solution when irradiated by X–rays.

Another finding of this work was a peculiar behavior of the organically modified SiO_2/Si surfaces when subjected to HF etching. While HF removed the SiO_2 layer, as supported by IRSE results, the organic layer was not removed together with the SiO_2 interface on which it was grafted. This behavior was reasoned by HF etching kinetics, upon which we proposed that the removal of the SiO_2 was slower than the rebinding of the organic molecules to other (slightly positive) sites on the silicon surface. For a detailed understanding of this process further theoretical calculations are necessary.

Organic functionalization allows tailoring of the surface and interface properties, and thus it is becoming of high importance in research and industry. Tuning of the surface properties, such as electron affinity, wettability, pH sensitivity and so forth can be enabled by a change of the functional group of the attached organic material. In this work it was shown that oxidation of the underlying silicon surface can be slowed down through organic modification. We proposed that the size of the molecule plays an important role in oxidation kinetics, where the 4–methoxydiphenyl amine (C_6H_5–NH–C_6H_5–OCH_3), composed of two phenyl rings, slows down the interface oxidation more than the nitrobenzene ($C_6H_5NO_2$), composed of one benzene ring. These results are important, for instance, in photovoltaic technology where the stable, well passivated interfaces are crucial for the control of the charge recombination centers.

Biological compatibility of the surfaces can be realized through the bio–reactive functional groups such as NH_2. One of the aims of this work was to study in detail the reduction of nitrobenzene ($C_6H_5NO_2$) to aniline ($C_6H_5NH_2$) on silicon surface upon irradiation with X-rays. The components of the reduction process were proposed upon a detailed deconvolution of the observed core levels. It was found that the irradiation induced the reduction of the NO_2 to a NH_2 functional group, leaving the benzene rings intact. Additionally, we proposed that polymerization of the benzene units takes place as a result of the X–ray irradiation. The procedure of lithographic patterning through X–ray irradiation can be employed in fabrication of biosensor arrays for biological analysis and diagnostics.

While this work provided a wealth of information useful for understanding and improvement of the electrochemical processes, several open questions still remain unresolved. Many of the difficulties are related to the detectivity limits of the experimental methods. For instance, our interpretation of the IRSE spectra was based on the relatively strong infrared active vibrational bands. However, weaker bands which were in the noise level could have supplied additional information on the film structure and bondings. One such problem was related to the proof of the formation of covalent Si–C (or Si–O–C) bonds between the

organic films and the silicon substrates. Since the expected amplitude of such absorption band is relatively week, additional techniques may be required for confirmation of this covalent attachment. In this work, expansion of the IRSE technique to lower frequencies was performed for the direct proof of the Si–C or (Si–O–C) formation. Further improvement of the signal–to–noise ratio is still necessary. This can be achieved, for example, by surface-enhanced infrared absorption (SEIRA) spectroscopy, where evaporation of discontinuous metallic films on the organically modified surfaces results in enhanced absorption bands.

Additional open issues are related to the lack of optical data on the studied organic materials. This is the situation in the research of every new material, and the related problems may be solved by cross correlated analysis employing several surface sensitive techniques. Such cross–correlated approach was the focus of this work, where IRSE, XPS and VIS–ellipsometric studies were performed for the determination of the optical constants of the thin films. However, improvement of those techniques and development of new surface–sensitive methods are necessary for the analysis of organic/inorganic surfaces and interfaces.

Those open questions of this work introduce new interesting research possibilities. Directions for future research are diverse. On one hand, it includes the development of the well controlled, technologically relevant deposition methods for engineering of new hybrid organic/inorganic devices. On the other hand, it demands improvement of the surface sensitive techniques. In parallel, expansion of the theoretical background should be performed for the interpretation of the experimentally obtained results.

Appendix A

Simulations of the IRSE spectra

In this appendix we discuss simulations of the IRSE spectra, and show the possibilities and limitations of the technique for the determination of the high–frequency refractive index and thickness of the measured thin films. Advantages of the multiple-angle measurements will be demonstrated.

A.1 Spectroscopic properties of thin films

Fig. A.1 shows plots of the reflectance Rp, Rs and ellipsometric parameters $\tan\psi$ and Δ for films of 5 nm, 50 nm and 500 nm and 5000 nm thickness. While multiple minima and maxima occur across the whole spectral range for thicker films (Fig. A.1), no such minima and maxima occur for the thinner films in the MIR spectral range. The extrema are at higher photon energies, which would be more sensitive for thickness determination of thinner films. Fig. A.1 implies that for investigations of the film thickness, the choice of the spectral range might be critical. In the next sections we present a careful theoretical analysis of the parameters that influence the determination of the high-frequency refractive index and film thickness in ellipsometric investigations.

In the next sections we are going to perform theoretical calculations in order to demonstrate the results for "model" case, which does not take into account experimental limitations or frequency–dependent dispersion. The calculations of thin film of a high-frequency refractive index of 1.46 will be assumed. We will discuss two types of substrates: the one with a refractive index n_2=3.48 and the other representing a metallic substrate with n_2=3.48+31.7i. These values were chosen with the same real part in the refractive index in order to perform comparison between the two cases. Moreover, the value n_2=3.48 represents well the properties of a Si substrate in the MIR spectral range, while the value n_2=3.48+31.7i is representative for Au substrate at 2000 cm^{-1} [209]. The simplified dispersion–free approach will be justified in section A.2 for the

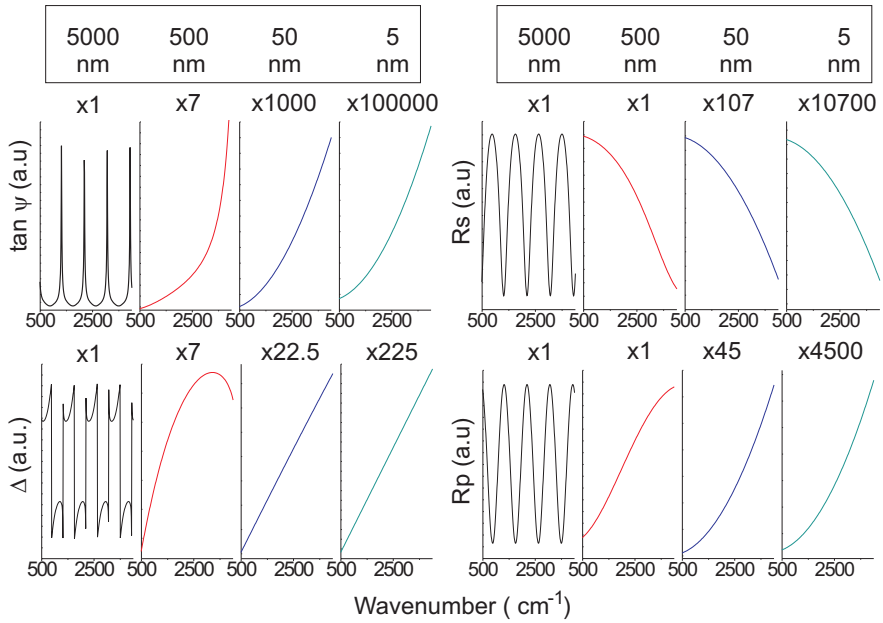

Figure A.1: Calculated ellipsometric parameters $\tan\psi$ and Δ and reflectance Rp, Rs for films of 5000 nm, 500 nm and 50 nm and 5 nm of a refractive index 1.46 on a substrate of n_∞=3.48 (typical for Si), at the angle of incidence 65^0 in MIR spectral range. The numbers on the plots indicate zoom factors relatively to the data shown for 5000 nm film.

purpose of the present discussion only. Otherwise, frequency–dependent values of the optical constants of substrates and thin films were taken into account throughout the rest of this thesis.

A.2 Best-fit calculations

For best-fit calculations, the least-squares routine is typically applied [210]. In this work it was done by fitting of the measured ellipsometric parameters tan ψ and/or Δ using models described in chapter 3. Typically for evaluation of film's thickness d and its refractive index n, the fit on ellipsometric parameter Δ is performed, since the parameter Δ is more sensitive for thickness and refractive index of a film. This is demonstrated in Fig. A.2, where the results of simulations of a thin nitrobenzene film on Au substrate are shown. The spectra shown in gray were calculated using constant refractive index n=1.46 in the spectral range of interest. For spectra shown in black dispersion model based on the Lorentz oscillators was implemented (for oscillator parameters employed in this simulation see section 5.2). The major differences between the spectra simulated employing the dispersion and those for which the refractive index n

was wavelength–independent was in the absorption region of the NB molecule, between 1300 and 1620 cm^{-1}. Outside this spectral range, the spectra carry a nearly identical character. Fig. A.2 shows that the background, the band amplitudes and the slope of the Δ change in response to the thickness variation. The difference in the slope of the Δ is for instance 20 % between the 5 nm and 15 nm organic films. Both ellipsometric parameters tan ψ and Δ exhibited a change in the absorption bands amplitude for spectra for calculations of which the dispersion model was implemented.

When the absorption constants are known, they can be used in Lorentz oscillator model for independent thickness evaluation. However, it is not the case for many organic materials. Consequently, the best fit is typically applied to the Δ spectrum in the spectral range where contributions of vibrational features are negligibly small. During such best–fit procedure, film thickness d and film refractive index n are varied until the best fit is achieved. In our case, the fit of

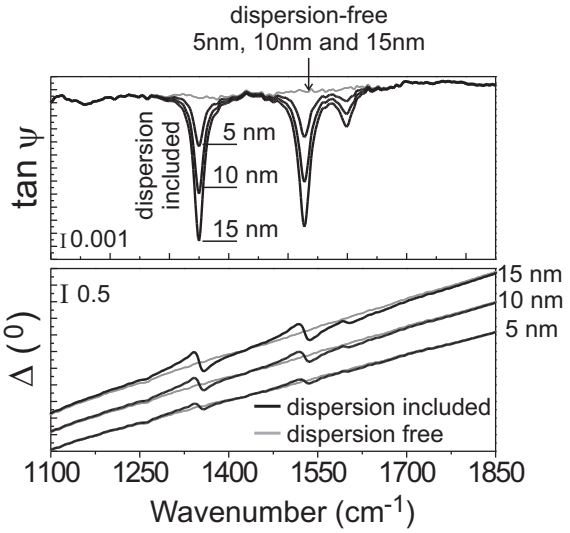

Figure A.2: Simulated ellipsometric parameters tan ψ and Δ for nitrobenzene thin films with 5 nm, 10 nm and 15 nm film thicknesses on Au–coated glass substrate at 70^0 incident angle. Black: simulations including the dispersion due to NB absorption bands; gray: no dispersion was assumed. Simulations were performed using models from chapter 3 and optical constants from section 5.2. In these simulations the *measured* gold–coated substrate optical constants were employed.

the ellipsometric parameters is based on Airy reflection coefficients r_A (Eq. 3.35, chapter 3). Eq. 3.35 however implies a complex dependency of r_A coefficients (and thus the ellipsometric parameters tan ψ and Δ) on a thickness d and a refractive index n of a film. This dependency enables several {n,d} solutions for a single measured curve. It is thus useful to investigate these dependencies

in detail. We perform a theoretical analysis of the n,d film solutions using the following procedure: Firstly, a theoretical spectrum of the ellipsometric parameter Δ_{ini} is calculated at a certain angle of incidence. For convenience, we take n_{ini}=1.46 of the thin film (representing a typical organic polymer film, for example), and n_2=3.48, simulating the refractive index of a Si substrate. Next, we fit the Δ_{ini} using the least–square trust region dogleg routine [211] looking for minimum of $\sum_i(\Delta_{ini}(w_i) - \Delta_{fit}(w_i))^2$, where Δ_{fit} is calculated through variation of the high-frequency refractive index n_{fit} and thickness d_{fit} of a film, where *fit* stands for *fitted* values (to distinguish them from the *initial* values at which Δ_{ini} was calculated). Ideally, a single solution for n_{fit} matching n_{ini} and for d_{fit} matching d_{ini} should be found.

Fig. A.3 shows the results of the calculations for 5 nm thin film at 65^0 incident angle in the infrared spectral range between 700 and 4000 cm^{-1}. At a single angle, the minimum of $\sum_i(\Delta_{ini}(w_i) - \Delta_{fit}(w_i))^2$ is achieved, however, for a set of pair values n and d, which is situated along the minima of the 3–D chart shown on left panel in Fig. A.3. The right panel of Fig. A.3 shows the actual solution by the crossing white lines, which falls within the space of the all other possible pair values n and d giving the solution for Δ_{ini}.

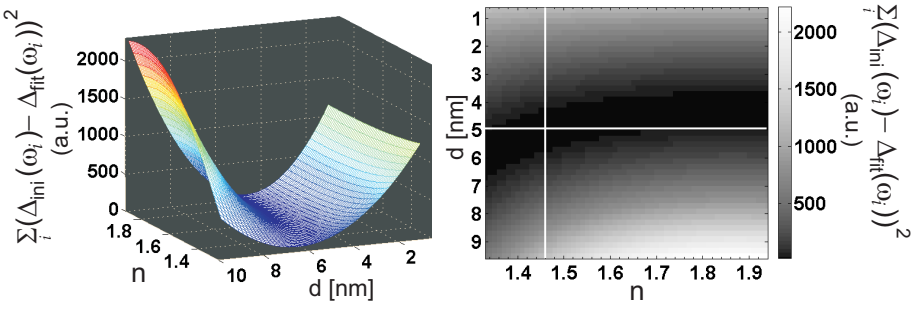

Figure A.3: The charts of $\sum_i(\Delta_{ini}(w_i)-\Delta_{fit}(w_i))^2$ as a function of the film high frequency refractive index n and thickness d. Left: a 3D chart view; Right: same as left panel, chart view from above. The set of the {n,d} solutions for Δ_{ini} is situated along the minima of the left chart and along the dark shaded area in the right chart. The intersection of the white lines shows the actual parameters of n_{ini}=1.46 and d_{ini}=5 nm at which Δ_{ini} was calculated. Calculations were performed in the infrared spectral range between 700 and 4000 cm^{-1} at 65^0 incident angle.

.

Fig. A.4 shows the plots of $\sum_i(\Delta_{ini}(w_i) - \Delta_{fit}(w_i))^2$ as a function of varying n and d, for simulated films with several different thicknesses. For thicknesses above 30 nm, solutions (shown as minima in the plots of Fig. A.4) could be found. However, below this thickness value, the values of $\sum_i(\Delta_{ini}(w_i) - \Delta_{fit}(w_i))^2$ could not converge to the given solution. The problem can be al-

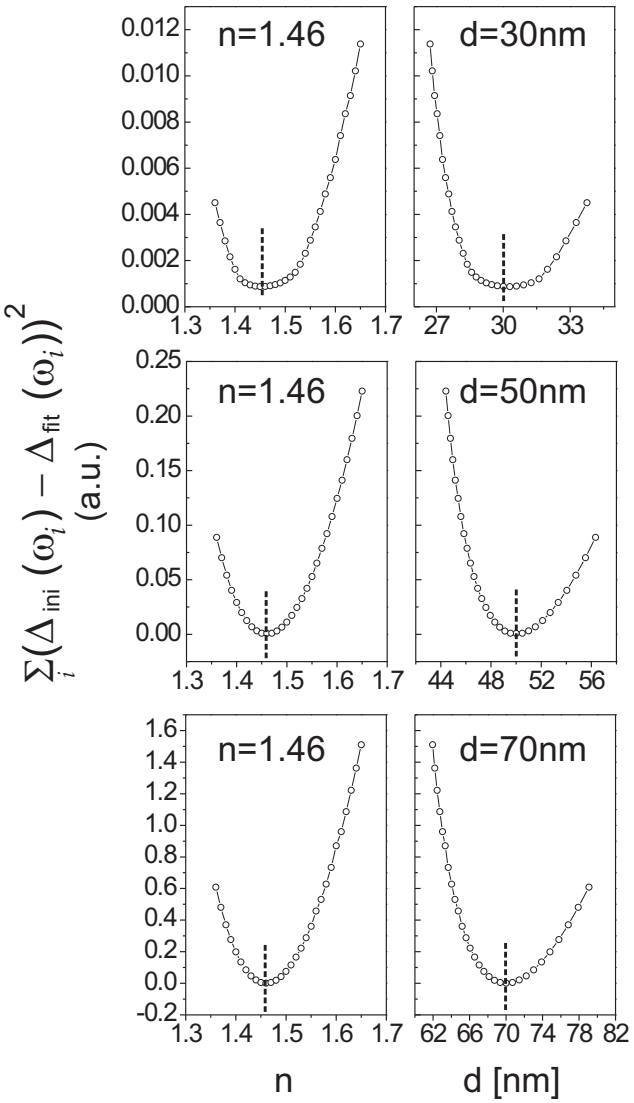

Figure A.4: The values of $\sum_i(\Delta_{ini}(w_i) - \Delta_{fit}(w_i))^2$ as a function of the film high frequency refractive index n and thickness d. Each figure exhibits the actual parameters of d_{ini} at which Δ_{ini} was calculated (n_{ini}=1.46 was kept for all graphs). These values are marked by the broken lines. Calculations were performed in the infrared spectral range between 700 and 4000 cm^{-1} at 65^0 incident angle.

ready observed for the solution for the 30 nm film, where a "flat" minimum is achieved for the extended range of the {n,d} values.

A.3 Multiple-angle measurements routine

The purpose of using multiple angles in ellipsometry measurements is to increase the amount of data available to characterize a material. Varying the angle of incidence changes, for instance, the path length in the film and the reflectance of the s- and p- polarized radiation, Rp and Rs. For evaluation of the multiple-angle spectra, often best-fit calculations are used. Here we will describe and analyze a method of fitting the Δ spectra at multiple angles. Typically the substrate optical constants are available from separate ellipsometric measurements. This is also advisable since a certain variation in optical constants can prevail due to varying doping and surface treatment (for semiconductor materials such as Si) or due to different coating methods (such as Au/glass substrates).

The calculated data is optimized to fit the experimental spectra taken at several different incidence angles, and the results are refined until the best fit is reached. Following this procedure, improved consistency of the deduced values can be attained.

The procedure for determination of the thickness and high-frequency refractive index of thin organic films generally follows the same steps as described earlier for a single angle of incidence in section A.2. As before, we are looking for $\{n, d\}$ pairs resulting in a solution of $\sum_i(\Delta_{ini}(w_i) - \Delta_{fit}(w_i))^2 = 0$. As in section A.2, however, multiple solutions of $\{n, d\}$ pairs are available for spectra at each incidence angle. The advantage of performing this procedure for several angles of incidence is that in general a unique solution of single $\{n, d\}$ pair for the given film can be found. Fig. A.5 shows such solution for a 70 nm thick film with n=1.46 on a Si substrate (left panel). The solution is given as an intersection of {n,d} plots at different incident angles. However, simulations for Au substrate result in an overlap of {n,d} solutions for all 4 simulated angles of incidence in the spectral range between 2000 cm^{-1} and 4000 cm^{-1}. The reason for this can be revealed from observation of wavelength-defendant plots in Fig. A.5. For Si, there is a strong change in Δ around 75^0 in the spectral region of interest (2000 cm^{-1} – 4000 cm^{-1}) as shown in Fig. A.6. Thus there is also a strong change in the $\{n, d\}$ solution occurring around this angle (Fig. A.5). This is the Brewster angle region ($\varphi_{Brewster} \approx 74^0$ for $n_{substr} = 3.48$, which was taken to represent Si substrate). For n_{substr}=3.48+i*31.7, which was taken to represent the Au substrate, there is no steep angle dependence analogue to that of the Si in the spectral range of interest, as can be seen in Fig. A.6. However, for thicker film thickness it becomes possible to find the single {n,d} solution also for a metallic substrate, as demonstrated in Fig. A.7 for a 250 nm thick film. This example illustrates the importance of the substrate optical properties on determination of the film {n,d} parameters. In experimental IRSE measurements, however, the 75^0 angle of incidence is problematic due to a high opening angle of the radiation coming from the globar source.

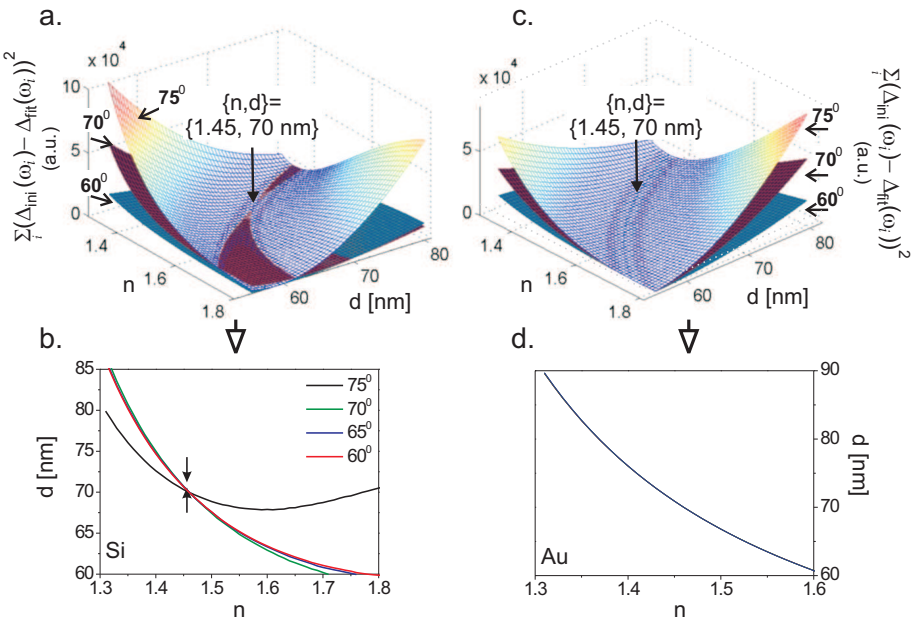

Figure A.5: Plots of the $\{n, d\}$ of thin film (d=70 nm, n=1.46) giving solution for $\sum_i(\Delta_{ini}(w_i) - \Delta_{fit}(w_i))^2 = 0$. (a) and (b): substrate with n_{substr}=3.48 (Si); (c) and (d): n_{substr}=3.48+i*31.7 (Au). In the upper panel, a three dimensional representation for the $\sum_i(\Delta_{ini}(w_i) - \Delta_{fit}(w_i))^2 = 0$ at 60^0, 70^0 and 75^0 is shown by three colored surface plots. The solutions are represented by the intersections of all three plots, where a single solution is available for Si and multiple solutions for Au substrate. The actual solution $\{n, d\}$={1.46,70 nm} is marked. Lower panel: only the data along the *minimum* of the $\sum_i(\Delta_{ini}(w_i) - \Delta_{fit}(w_i))^2 = 0$ is shown. The solution for n,d for Si substrate is given by an intersection of the individual curves for each angle. For gold substrate, all of the solution curves for all angles coincide on the same curve. Spectra were simulated in a spectral range between 2000 cm^{-1} and 4000 cm^{-1}.

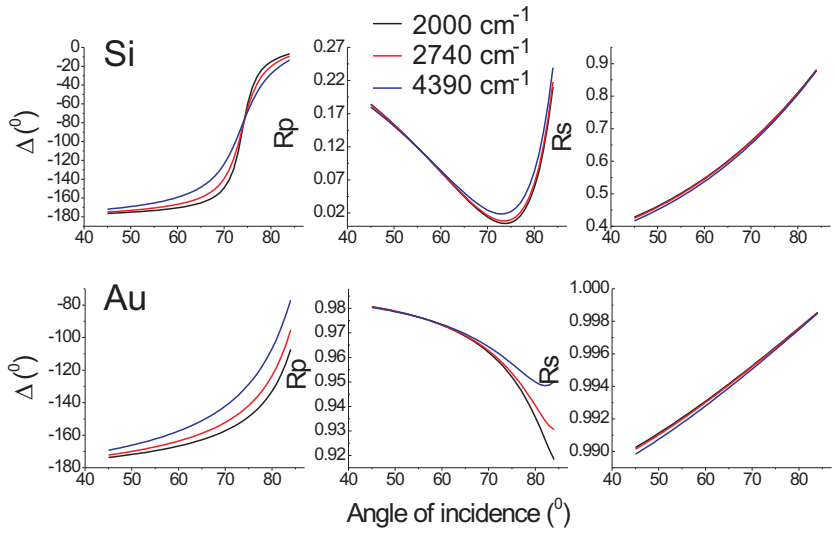

Figure A.6: Plots of Δ,R_p, R_s as a function of angle of incidence for different wavelength in MIR spectral range (see color code). Calculated for a film of 70 nm thickness with high-frequency refractive index n=1.46.

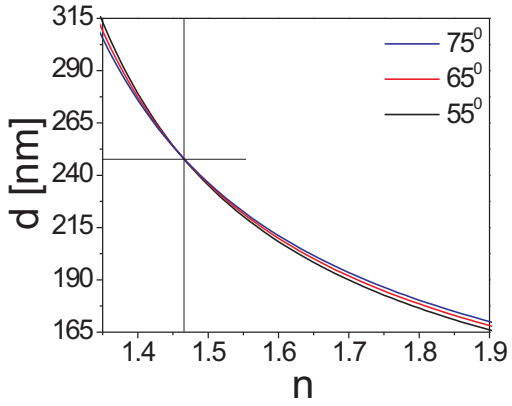

Figure A.7: Plots of the $\{n, d\}$ for a thin film with thickness d=250 nm and n=1.46 giving solution for $\sum_i(\Delta_{ini}(w_i) - \Delta_{fit}(w_i))^2 = 0$. n_{substr}=3.48+i*31.7 (Au),in the spectral range 2000 cm^{-1} to 4000 cm^{-1}.

Using the measured Δ spectra for evaluation of the refractive index and thickness of thinner films on silicon substrate in MIR spectral range is not straight-forward. For instance, fitting of the simulated 15 nm thin film on a Si substrate leaded to coinciding curves (multiple solutions) at 3 different angles in the spectral region of interest. Thus the measurements at a lower wavelength is desirable. Alternatively, in IRSE the thickness can be scaled from the strength of the absorption bands, but this will require the proof of the linearity of the strength of the absorption bands with the thickness of a given thin film. For our purposes, thickness and refractive of the ultra-thin films were measured using VIS–ellipsometry, improving the sensitivity to $\{n, d\}$ parameters of ultra-thin films. As a complimentary method, XPS analysis was used to determine thickness in ultra-thin nitrobenzene films.

Additional complication when working with measured data is the offset that may arise due to detector non–linearity. However, the procedure of the multiple angle fit can be in general adapted to treat this offset problem. This is because although each measurement shifts the Δ offset, it keeps the rest of the characteristic features of the spectrum without any change. The discussion is even more simplified when paying attention that in the spectral range of interest and for the thicknesses below 100 nm the Δ spectra can be approximated by a linear curve of the type Δ=$a\omega$+b with a being the slope of the curve and b is the Δ value at ω=0 (ω is the wavenumber). Using this property, the problem can be now separated into two parts: the slope of the Δ spectrum, which is kept unchanged during the measurements and the shifting parameter b. For our purposes, it makes sense to use the offset parameter b at the wavenumber ω in the range of interest (mid–infrared). Thus in the following discussion we use b=$\Delta(\omega = 2000cm^{-1})$.

The fitting procedure is in general the same as described earlier for multiple angle fit of the whole Δ spectrum. Previously, we were looking for $\{n, d\}$ pairs resulting in a solution of $\sum_i(\Delta_{ini}(w_i) - \Delta_{fit}(w_i))^2 = 0$. The change now is that we are looking for the solutions for a and b independently: $abs(a_{ini} - a_{fit}) = 0$ and $abs(b_{ini}(w$ =2000 cm$^{-1}) - b_{fit}(w$ =2000 cm$^{-1}) = 0$ should keep. Fig. A.8 shows the solution for a and b parameters which can be seen along the minima of the graphs. It should be pointed out that each of these parameters gives independent {n,d} solutions. This fact was exploited by the fitting of the *whole* Δ spectrum previously through looking for zeros of $\sum_i(\Delta_{ini}(w_i) - \Delta_{fit}(w_i))^2 =$ 0. However, Fig. A.8 shows that the solutions can also be found by fitting on the a and b components of the linear Δ spectra in the range of interest. Fig. A.9 shows the result of the multiple-angle approach, for slope a and for the parameter b. For each of these parameters, the single {n,d} solution can be obtained independently. Thus, it is in general sufficient to use the *slope* of the Δ spectrum and to ignore the background shift which is caused through the measurement. This approach can be also extended to more complicated shapes of Δ spectra, when a polynomial fit can be applied to the Δ spectrum and then the analysis can be performed on the individual polynomial coefficients.

To summarize, IRSE measurements are suitable for evaluation of thickness and refractive index. This can be either done by scaling of the absorption bands

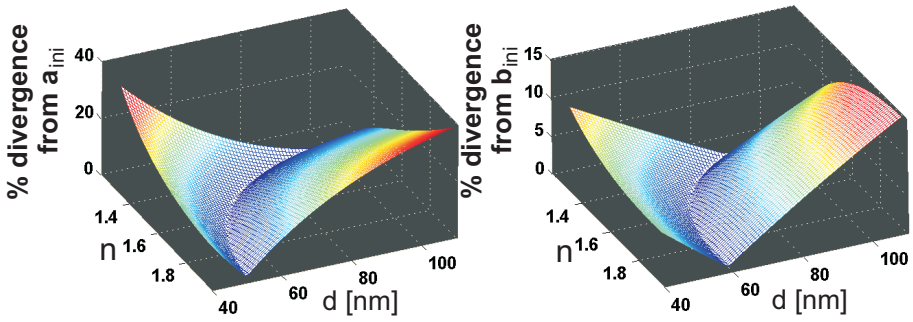

Figure A.8: Maps showing the solution for the slope a (left panel) and for b=$\Delta(\omega$ =2000 cm^{-1}) (right panel), when the measured Δ spectra are approximated by a linear curve. The solution for {n,d} are given along the minima of the graphs, where the divergence (shown in %) of the a_{fit} and b_{fit} from a_{ini} and b_{ini}, respectively, is zero. The calculated range was 2000 cm^{-1} to 4000 cm^{-1}, at 70^0 angle of incidence.

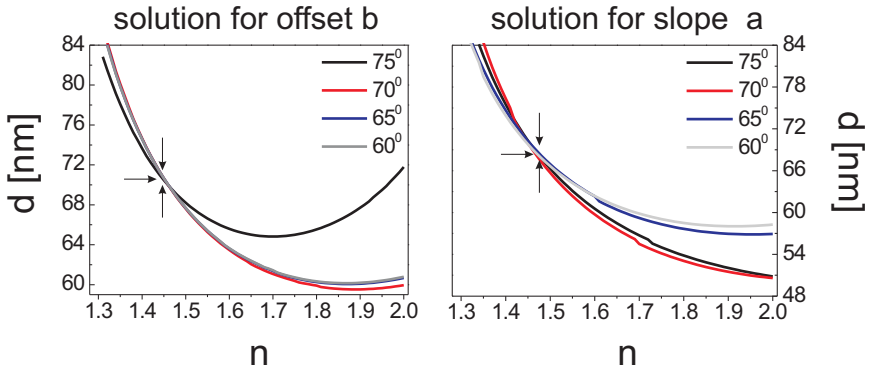

Figure A.9: Plot of the $\{n, d\}$ of thin film giving the zero solution for $abs(b_{ini}(w$ =2000 cm$^{-1}) - b_{fit}(w$ =2000 cm$^{-1})^2 = 0$ (left) and $abs(a_{ini} - a_{fit}) = 0$ (right), at multiple angles of incidence, with n_{substr}=3.48. The intersection of these functions gives the unique {n$_{ini}$,d$_{ini}$} solution of the thin film (d$_{ini}$=70 nm,n$_{ini}$=1.46). The calculated range was 2000 cm^{-1} to 4000 cm^{-1}.

due to molecular vibrations from the well-known "calibration" sample, or using the interference properties of the obtained spectra. When the latter attitude is applied, optimal parameters (such as angle of incidence, appropriate spectral range) should be chosen in accordance to the substrate and the film optical properties. We have shown that the background shift that can occur during the measurements due to different radiation passage through the optical setup can be overcome.

In this work, we used multiple approaches and complementary techniques (VIS–ellipsometry, XPS) for analysis of the thickness and refractive index of the thin films.

Bibliography

[1] Morrison S. T. *Electrochemistry at semiconductor and oxidized metal electrodes*. Plenum press, New York, 1980.

[2] Hartig P., Rappich J., and Dittrich Th. *Appl. Phys. Lett.*, 80:67, 2002.

[3] Cahen D. and Hodes G. *Advanced Mater.*, 14:789, 2002.

[4] Hunger R., Jaegermann W., Merson A., Shapira Y., Pettenkofer C., and Rappich J. *J. Phys. Chem. B.*, 110:15432, 2006.

[5] Guenes S., Neugebauer H., and Sariciftci N. S. *Chem. Rev.*, 107:1324, 2007.

[6] Goh C., Scully S. R., and McGehee M. D. *J. Appl. Phys.*, 101:114503, 2007.

[7] Goetzberger A., Luther J., and Willeke G. *Sol. En. Mat. and Solar Cells*, 74:1, 2002.

[8] Bartic C., Campitelli A., and Borghs S. *Appl. Phys. Lett.*, 82:475, 2003.

[9] Song K.S., Hiraki T., Umezawa H., and Kawarada H. *Appl. Phys. Lett.*, 90:063901, 2007.

[10] Patolsky F., Zheng G., Hayden O., Lakadamyali M., Zhuang X., and Lieber C. M. *PNAS*, 101:14017, 2004.

[11] Ling M. M. and Bao Z. *Chem. Mater.*, 16:4824, 2004.

[12] Briggs D., Brewis D.M., and Konieczko M.B. *J. Mater. Sci.*, 14:1344, 1979.

[13] Wells R.K., Badyal J.P.S., Drummond I.W., Robinson K.S., and Street F.J. *Polymer*, 34:3611, 1993.

[14] Rye R.R. and Martinetz R.J. *J Appl Polym Sci*, 37:2529, 1989.

[15] Wolkow R. A. *Annu. Rev. Phys. Chem.*, 50:413, 1999.

[16] Forrest S.R. *Chem. Rev.*, 97:1793, 1997.

[17] Umbach E., Sokolowski M., and Fink R. *Appl. Phys. A*, 63:565, 1996.

[18] Rochet F., Jolly F., Bournel F., Dufour G., Sirotti F., and Cantin J.L. *Phys. Rev. B*, 58:11029, 1998.

[19] Quinn J. F., Johnston A. P. R., Such G. K., Zelikin A. N., and Caruso F. *Chem. Soc. Rev.*, 37:707, 2007.

[20] Buriak J. M. *Chem. Rev.*, 102:1271, 2002.

[21] Ulman A. *An Introduction to Ultrathin Organic Films: From Langmuit-Blodgett to Self-Assembly*. Academic Press, Boston, 1991.

[22] Ashkenasy G., Cahen D., Cohen R., Shanzer A., and Vilan A. *Acc. Chem. Res.*, 35:35, 2002.

[23] Hartig P., Dittrich Th., and Rappich J. *J. Electroanal. Chem.*, 524-525:120, 2002.

[24] Bard A. J. and Faulkner L. R. *Electrochemical Methods: Fundamentals and Applications*. Wiley, 2nd ed., 2000.

[25] Allongue P., de Villeneuve C. H., Cherouvrier G., Cortes R., and Bernard M. C. *J. Electroanal. Chem.*, 550-551:161, 2003.

[26] Merson A., Dittrich Th., Zidon Y., Rappich J., and Shapira Y. *Appl. Phys. Lett.*, 85:1075, 2004.

[27] Gensch M., Roodenko K., Hinrichs K., Hunger R., Guell A.G., Merson A., Schade U., Shapira Y., Dittrich T., Rappich J., and Esser N. *J. Vac. sci. and Technol. B.*, 23:1838, 2005.

[28] Roodenko K., Rappich J., Gensch M., Esser N., and Hinrichs K. *Appl. Phys. A*.

[29] Boukherroub R., Morin S., Bensebaa F., and Wayner D. D. M. *Langmuir*, 15:3831, 1999.

[30] Fellah S., Boukherroub R., Ozanam F., and J.-N. Chazalviel. *Langmuir*, 20:6359, 2004.

[31] Rappich J., Merson A., Roodenko K., Dittrich Th., Gensch M., Hinrichs K., and Shapira Y. *J. Phys. Chem. B.*, 110:1332, 2006.

[32] Vlasov Y. G., Tarantov Y. A., and Bobrov P. V. *Anal. Bioanal. Chem.*, 376:788, 2003.

[33] Madou M. J., Frese K. W. Jr., and Morrison S. R. *Phys. Stat. Sol. A*, 57:705, 1980.

[34] Yamashita Y., Asano A., Mishioka Y., and Kobayashi H. *Phys. Rev. B.*, 59:15872, 1999.

[35] Angermann H., Henrion W., Rebien M., and Röseler A. *Appl. Surf. Sci.*, 235:322, 2004.

[36] Bernard M. C., Chausse A., Cabet-Deliry E., Chehimi M. M., Pinson J., Podvorica F., and Vautrin-Ul C. *Chem. Mater.*, 15:3450, 2003.

[37] Higashi G. S, Becker R. S, Chabal Y. J., and Becker A. J. *Appl. Phys. Lett.*, 58:1656, 1991.

[38] Jakob P. and Chabal Y. J. *J. Chem. Phys.*, 95:2897, 1991.

[39] Allongue P., de Villeneuve C. H., Morin S. Boukherroub R., and Wayner D. D. M. *Electrochim. Acta*, 45:4591, 2000.

[40] Trucks G. W., Raghavachari K., Higashi G. S., and Chabal Y. J. *Phys. Rev. Lett.*, 65:504, 1990.

[41] Foell H., Christophersen M., Carstensen J., and Hasse G. *Mater. Sci. Engineering R.*, 39:93, 2002.

[42] Smith R. L. and Collins S. D. *J. Appl. Phys.*, 71:R1, 1992.

[43] Yahyaoui F., Dittrich Th., Burke Th., Aggour M., Lust S., Levy-Clement C., and Rappich J. *J. Electrochem. Soc.*, 149:E472, 2002.

[44] Lehmann V. and Roennebeck S. *J. Electrochem. Soc.*, 146:2968, 1999.

[45] Lehmann V. and Goesele. *Appl. Phys. Lett.*, 58:856, 1991.

[46] Canham L. T. *Appl. Phys. Lett.*, 57:1046, 1990.

[47] Hirschman K. D., Tsybeskov L., Duttagupta S. P., and Fauchet P. M. *Nature*, 384:338, 1996.

[48] Cullis A. G., Canham L. T., and Calcott P. D. J. *J. Appl. Phys.*, 82:909, 1997.

[49] Blyholder G. *J. Phys. Chem*, 68:2772, 1964.

[50] Chabal Y.J. and Raghavachari K. *Surf. Sci.*, 502:41, 2002.

[51] Morse P. M. *Phys. Rev.*, 34:57, 1929.

[52] Nakamoto K. *Infrared and Raman Spectra of Inorganic and Coordination Compounds, 5th edition*. Willey Interscience, New-York, 1997.

[53] Nielsen J. R. and Holland R. F. *J. Molec. Spectrosc.*, 6:394, 1961.

[54] Kittel C. *Introduction to Solid State Physics*. John Willey and Sons, New-York, 1996.

[55] Yu P. Y. and Cardona M. *Fundamentals of Semiconductors. Physics and Material Properties*. Springer, Berlin, 1996.

[56] Röseler A. and Korte E. H. *Handbook of vibrational spectroscopy*, volume 2. Editors: Griffith P. R and Chalmers J. (John Wiley and Sons, Chichester, 2002), 2002.

[57] Hasegawa T., Nishijo J., Umemura J., and Theiss W. *J. Phys. Chem. B*, 105:11178, 2001.

[58] Tu Y. and Tersoff J. *Phys. Rev. Lett.*, 84:4393, 2000.

[59] Brendel R. and Bromann D. *J. Appl. Phys.*, 71:1, 1991.

[60] Naiman M. L., Kirk C. T., Aucoin R. J., Terry F. L., and Wyatt P. W. *J. Electrochem. Soc.*, 131:637, 1984.

[61] Teitler S. and Henvis B. W. *J. Opt. Soc. Am*, 60:830, 1970.

[62] Berreman D. W. *J. Opt. Soc. Am*, 62:502, 1972.

[63] Azzam R. M. A. and Bashara N. M. *Ellipsometry and Polarized Light*. North Holland Publishing Company, Amsterdam, 1977.

[64] Chabal Y. J. *Physica B*, 170:447, 1991.

[65] Ong C. K. and Khoo G. S. *J. Phys. C*, 20:419, 1986.

[66] Berreman D. W. *Phys. Rev.*, 130:2193, 1963.

[67] Tolstoy V.P., Chernyshova I. V., and Skryshevsky V. A. *Handbook of Infrared Spectroscopy of Ultrathin Films*. Willey Interscience, New-York, 2003.

[68] Vickerman J. C. *Surface analysis. The principle techniques*. Wiley-VCH, Weinheim, Germany, 1997.

[69] Sakamoto K., Hashizume H., Nagafusa M., Sato H., and Ushioda S. *Surf. Sci.*, 368:292, 1996.

[70] Campion A. and Kambhampati P. *Chem. Soc. Rev.*, 27:241, 1998.

[71] Duwez A.-S. *J. Elect. Spectr. Relat. Phenom.*, 134:97, 2004.

[72] Reinert F. and Huefner S. *New Journ. Phys.*, 7:97, 2005.

[73] Himpsel F.J. *Brazil. Journ. Phys.*, 23:31, 1993.

[74] Hunger R., Fritsche R., Jaeckel B., Jaegermann W., Webb L. J., and Lewis N.W. *Phys. Rev. B*, 72:045317, 2005.

[75] Hinrichs K., Gensch M., and Esser N. *Appl. Spectr.*, 59:272A, 2005.

[76] Brunet-Bruneau A., Fisson S., Vuye G., and Rivory J. *J. Appl. Phys.*, 87:7303, 2000.

[77] Yang F., Roodenko K., Hinrichs K., and Rappich J. *J. Micromech. Microeng.*, 17:S56, 2007.

[78] Tiwald T. E., Woollam J. A., Zollner S., Christiansen J., Gregory R. B., Wetteroth T., Wilson S. R., and Powell A. R. *Phys. Rev. B*, 60:11464, 1999.

[79] Röseler A. and Molgedey W. *Infrared Physics*, 24:1, 1984.

[80] Schubert M. *Thin Solid Films*, 313:323, 1998.

[81] Röseler A. *J. Opt. Soc. Am.*, A 9:1124, 1992.

[82] Roodenko K., Gensch M., Heise H.M., Schade U., Esser N., and Hinrichs K. *Infrared Phys. and Technol.*, 49:39, 2006.

[83] Schade U., Bartl F., Hofmann K.P., Illing G., Korte E.H., Peatman W.B., and Röseler A. *BESSY Annual Report*, 1998:457, 1998.

[84] Snyder R. G. *J. Chem. Phys.*, 47:1316, 1967.

[85] Keyes R. J. (editor). *Optical and Infrared Detectors, 2nd edition*. Springer-Verlag, Berlin, 1980.

[86] Wolfe W. L. and Zissis G. J. *The Infrared Iandbook*. The Infrared Information Analysis (IRIA) Center, Michigan, 1993.

[87] Rogalski A. *Infrared Detectors*. CRC, Singapore, 2000.

[88] Richards P. L. *J. Appl. Phys.*, 76:1, 1994.

[89] Seah M.P. and Dench W. A. *Surf. Interface Anal.*, 1:2, 1979.

[90] Himpsel F. J., McFeely F. R., Taleb-Ibrahimi A., and Yarmoff J. A. *Phys. Rev. B.*, 38:6084, 1988.

[91] Lu Z. H., Graham M. J., Jiang D. T., and Tan K. H. *Appl. Phys. Lett.*, 63:2941, 1993.

[92] Briggs D. and Seah M. P. *Practical surface analysis: Auger and X-ray photoelectron spectroscopy*. John Wiley and Sons Ltd, 1996.

[93] Beamson G. and Briggs D. *Molec. Phys.*, 76:919, 1992.

[94] Mayer T., Lebedev M. V., Hunger R., and Jaegermann W. *Appl. Surf. Sci.*, 252:31, 2005.

[95] Proctor A. and Sherwood P. M. A. *Anal. Chem.*, 54:13, 1982.

[96] Tougaard S. *Surf. Interface Anal.*, 25:137, 1997.

[97] Steiner P., Höchst H., and Hüfner S. *Z. Physik B*, 30:129, 1978.

[98] Wagner C. D., Davis L. E., Zeller M. V., Taylor J. A., Raymond R. H., and Gale L. H. *Surf. Interf. Anal.*, 3:211, 1981.

[99] Tanuma S. and Powell C.J.and Penn D.R. *Surf. Interface Anal.*, 21:165, 1994.

[100] Mohai M. *Surf. Interface Anal.*, 36:828, 2004.

[101] Clarkson J. and Smith W. E. *J. Mol. Struct.*, 655:413, 2003.

[102] Balfour W. J. *Spectrochim. Acta Part A*, 39:795, 1983.

[103] Nuttall R. H., Roberts E. R., and Sharp D. W. A. *Spectrochim. Acta*, 17:947, 1961.

[104] Tabei K. and Ito C. *Bull. Chem. Soc. Jap.*, 41:514, 1968.

[105] Whetsel K. B., Hawkins G. F., and Johnson F. E. *J. Am. Chem. Soc.*, 78:3360, 1956.

[106] Cote G. L. and Thompson H. W. *Proc. Royal Soc. London A: Math. Phys. Sci.*, 210:217, 1951.

[107] Mayo D. W., Miller F. A., and Hannah R. W. *Course notes on the interpretation of infrared and Raman Spectra*. John Wiley and Sons, Inc., Hoboken, New Jersey, 2004.

[108] Zollinger H. *Diazo Chemistry I.* VCH Verlagsgesellschaft, Weinheim, 1994.

[109] Glaser R., Horan C. J., Lewis M., and Zollinger H. *J. Org. Chem.*, 64:902, 1999.

[110] Chabal Y. J., Higashi G. S., and Raghavachari K. *J. Vac. Sci. Technol. A.*, 7:2104, 1989.

[111] Yota J. and Burrows V. A. *J. Appl. Phys.*, 69:7369, 1991.

[112] Angermann H., Henrion W., Rebien M., and Röseler A. *Solar Energy Mater. Solar Cells*, 83:331, 2004.

[113] Bocharov S. and Teplyakow A. V. *Surf. Sci.*, 573:403, 2004.

[114] Syomin D., Wang J., and Koel B. E. *Surf. Sci.*, 495:L827, 2001.

[115] Hayden B. E. *Vibrational Spectroscopy of Molecules on Surfaces*. Plenum Press, New York, 1987.

[116] Laforgue A., Addou T., and Belanger D. *Langmuir*, 21:6855, 2005.

[117] Jin H., Kinser C. R., Bertin P. A., Kramer D. E., Libera J. A., Hersam M. C., Nguyen S. T., and Bedzyk M. J. *Langmuir*, 20:6252, 2004.

[118] Senf F., Flechsig U., Eggenstein F., Gudat W., Klein R., Rabus H., and Ulm G. *J. Synchr. Radiation*, 5:780, 1998.

[119] Beckhoff B., Fliegauf R., Ulm G., Pepponi G., Wobrauschek P., Fabry L., and Pahlke S. *Spectrochim. Acta part B*, 56:2073, 2001.

[120] Beatrix Pollakowski. Monitoring X–ray fluorescence signal from nitrobenzene–modified Si(111) surface at the plane–grating monochromator (PGM) beamline for undulator radiation at the Physikalisch-Technische Bundesanstalt (PTB) at BESSY II. Private communication, 2007.

[121] Gensch M. *Infrared ellipsometry for the investigation of interfacial layers and thin organic films on silicon*. Mensch und Buch Verlag, 2005. PhD thesis.

[122] Roodenko K., Gensch M., Rappich J., Hinrichs K., Esser N., and Hunger R. *J. Phys. Chem. B*, 111:7541, 2007.

[123] Henderson M. A. *Surf. Sci. Rep.*, 46:5, 2002.

[124] Skinner W. M., Prestige C. A., and Smart R. St. C. *Surf. Interface Anal.*, 24:620, 1996.

[125] Grellner F., Klingenberg B., Borgmann D., and Wedler G. J. *Electron. Spectrosc. Relat. Phenom.*, 71:107, 1995.

[126] Rappich J., Hartig P., Nickel N.H., Sieber I., Schulze S., and Dittrich Th. *Microelec. Engineer.*, 80:62, 2005.

[127] Smith B. *Infrared Spectral Interpretation. A Systematic Approach*. CRC press, New York, 1999.

[128] Eisenhardt C. G., Gemeschu A. S., Baumgrtel H., Chelli R., Cardini G., and Califano S. *Phys. Chem. Chem. Phys.*, 3:5358, 2001.

[129] Hinrichs K., Gensch M., Röseler A., and Esser N. *J. Phys.: Cond. Mat.*, 16:s4335, 2004.

[130] Plumb R. C. and Hornig D. F. *J. Chem. Phys.*, 23:947, 1955.

[131] Tan Y. P., Khatua S., Jenkins S. J., Yu J. Q., Spencer J. B., and King D. A. *Surf. Sci.*, 589:173, 2005.

[132] Syomin D., Kim J., Koel B. E., and Ellison G. B. *J. Phys. Chem. B*, 105:8387, 2001.

[133] Friderichsen A. V., Radziszewski J. G., Nimlos M. R. Winter P. R., Dayton D. C., David D. E., and Ellison G. B. *J. Am. Chem. Soc.*, 123:1977, 2001.

[134] Koval'chuk E.P., Stratan N.V., Reshetnyak O.V., Blazejowski J., and Whittingham M.S. *Solid State Ionics*, 141:217, 2001.

[135] Ogata Y.H., Tsuboi T., Sakka T., and Naito S. *J. Porous Mater.*, 7:63, 2000.

[136] Borghesi A., Sassella A., Pivac B., and Pavesi L. *Solid State Communications*, 87:1, 1993.

[137] Maruyama T. and Ohtani S. *Appl. Phys. Lett.*, 65:1346, 1994.

[138] Miura T., Niwano M., Shoji D., and Miyamoto N. *Appl. Surf. Sci.*, 101:454, 1996.

[139] Yang F. *PhD thesis, work in preparation.*

[140] Teyssot A., Fidelis A., Fellah S., Ozanam F., and Chazalviel J. N. *Electrochimica Acta*, 47:2565, 2002.

[141] Yamada T., Shirasaka K., Noto M., Kato H. S., and Kawai M. *J. Phys. Chem. B*, 110:7357, 2006.

[142] Canaria C.A., Lees I.N., Wun A.W., Miskelly G.M., and Sailor M.J. *Inorg. Chem. Commun.*, 5:560, 2002.

[143] Webb L. J., Rivillon S., Michalak D. J., Chabal Y. J., and Lewis N. S. *J. Phys. Chem. B*, 110:7349, 2006.

[144] Torres J. and Arkin I. T. *Biophys. J.*, 82:1068, 2002.

[145] Young T. F., Chen C. P., Liou J. F., Yang Y. L., and Chang T.C. *J. Porous Mater.*, 7:339, 2000.

[146] Yamada T., Kawai M., Wawro A., Suto S., and Kasuya A. *J. Chem. Phys*, 21:10660, 2004.

[147] Ferguson G. A. and Raghavachari K. *J. Chem. Phys*, 125:154708, 2006.

[148] Taguchi Y., Fujisawa M., Takaoka T., Okada T., and Nishijima M. *J. Chem. Phys*, 95:6870, 1991.

[149] Bateman J. E., Horrocks B.R., and Houlton A. *J. Chem. Soc. Faraday Trans.*, 93:2427, 1997.

[150] Michalak D. J., Rivillon S., Chabal Y. J., Esteve A., and Lewis N. S. *J. Phys. Chem. B*, 110:20426, 2006.

[151] Gurtner Ch., Wun A. W., and Sailor M. J. *Angew. Chem. Int. Ed.*, 38:1966, 1999.

[152] Yablonovitch E., Allara D. L., Chang C. C., and Gmitter T.and Bright T. B. *Phys. Rev. Lett.*, 57:249, 1986.

[153] Miura T., Niwano M., Shoji D., and Miyamoto N. *J. Appl. Phys.*, 79:4373, 1996.

[154] Ogawa H., Ishikawa K., Inomata C., and Fujimura S. *J. Appl. Phys.*, 79:472, 1996.

[155] Cheng C.L., Lin J.C., and Chang H.C. *J. Chem. Phys.*, 106:7411, 1997.

[156] Wang J. K., Tsai C. S., Lin C. E, and Lin J. C. *J. Chem. Phys.*, 113:5041, 2000.

[157] Disselkamp R., Chang H. C., and Ewing G. *Surf. Sci.*, 240:193, 1990.

[158] Newton T. A., Boiani J.A., and Hines M. A. *Surf. Sci.*, 430:67, 1999.

[159] MacLaren D. A., Curson N. J., Atkinson P., and Allison W. *Surf. Sci.*, 490:285, 2001.

[160] Khan A. and Hess P. *Appl. Phys. Lett.*, 85:4157, 2004.

[161] Lambers J. and Hess P. *Thin Solid Films*, 400:111, 2001.

[162] Hsiao G. S., Virtanen J. A., and Penner R. M. *Appl. Phys. Lett.*, 63:1119, 1993.

[163] Güell A. G., Roodenko K., Yang F., Hinrichs K., Gensch M., Sanz F., and Rappich J. *Mater. Sci. and Eng. B.*, 134:273, 2006.

[164] Kanashima T., Maida O., Kohma N., Agata M., Yudate S., Ueno M., Okuyama M., and Ohashi H. *Jap. J. Appl. Phys. part 1*, 40:4195, 2001.

[165] Allongue P., de Villeneuve C. H., Pinson J., Ozanam F., Chazalviel J. N., and Wallart X. *Electrochim. Acta*, 43:2791, 1998.

[166] Hoshino T. and Nishioka Y. *J. Chem. Phys.*, 111:2109, 1999.

[167] Smith W. H. and Bard A. J. *J. Am. Chem. Soc.*, 97:5203, 1975.

[168] Oliveria M. C. F. *Electrochim. Acta*, 48:1829, 2003.

[169] La Y. H., Kim H. J., I. S. Maeng, Jung Y. J., and Park J. W. *Langmuir*, 18:2430, 2002.

[170] Moon J. M., Kim K. J., Kang T. H., Kim B., Kang H., and Park J. W. *Langmuir*, 14:5673, 1998.

[171] Eck W., Stadler V., Geyer W., Zharnikov M., Gölzhäuser A., and Grunze M. *Adv. Mater.*, 12:805, 2000.

[172] Han S. W., Lee I., and Kim K. *Langmuir*, 18:182, 2002.

[173] Mendes P., Belloni P., Ashworth M., Hardy C., Nikitin K., Fitzmaurice D., Critchley K., Evens S., and Preece J. *Chem. Phys. Chem.*, 4:884, 2003.

[174] Klöpffer W. *Introduction to Polymer Spectroscopy.* Springer-Verlag, Berlin, 1984.

[175] Dittrich T., Schwartzkopff M., Hartmann E., and Rappich J. *Surf. Sci.*, 437:154, 1999.

[176] Dittrich T., Burke T., Koch T., and J. Rappich. *J. Appl. Phys.*, 89:4636, 2001.

[177] Distefano G., Guerra M., Jones D., Modelli A., and Colonna F. P. *Chem. Phys.*, 52:389, 1980.

[178] Keane M. P., de Brito A. N., Correia N., and Svensson S. *Chem. Phys.*, 155:379, 1991.

[179] Kumar S. N., Bouyssoux G., and Gaillard F. *Surf. Interface Anal.*, 15:531, 1990.

[180] Kohut-Svelko N., Reynaud S., Dedryevre R., Martinez H., Gonbeau D., and Francois J. *Langmuir*, 21:1575, 2005.

[181] Liu Y. C. and McCreery R. L. *Anal. Chem.*, 69:2091, 1997.

[182] Kishi K., Takata H., and Kohnushi S. *J. Electron Spectrosc. Relat. Phenom.*, 61:83, 1992.

[183] Huang S. H., Fischer D. A., and Gland J. L. *J. Phys. Chem.*, 100:10223, 1996.

[184] Ma Y., Chen C. T., Meigs G., Randall K., and Sette F. *Phys. Rev. A*, 44:1848, 1991.

[185] Klausen J., Tröber S. P., Haderlein S. B., and Schwarzenbach R. P. *Environ. Sci. Technol.*, 29:2396, 1995.

[186] Hunger R., Jaegermann R. R., Merson A., Y. Shapira, Pettenkofer C., and J. Rappich. *J. Phys. Chem. B*, 110:15432, 2006.

[187] Laforgue A., Addou T., and Belanger D. *Langmuir*, 21:6855, 2005.

[188] Stewart M. P., Maya F., Kosynkin D. V., Dirk S. M., Stapleton J. J., McGuiness C. L., Allara D. L., and Tour J. M. *J. Am. Chem. Soc.*, 126:370, 2004.

[189] Adenier A., Cabet-Deliry E., Chausse A., Griveau S., Mercier F., Pinson J., and Vautrin-Ul C. *Chem. Mater.*, 17:491, 2005.

[190] Allongue P., Delamar M., Desbat B., Fagebaume O., Hitmi R., Pinson J., and Saveant J.-M. *J. Am. Chem. Soc.*, 119:201, 1997.

[191] Riga J., Pireaux J. J., and Verbist J. *J. Mol. Phys.*, 34:131, 1977.

[192] Takahata Y. and Chong D. P. *Bull. Chem. Soc. Jpn.*, 73:2453, 2000.

[193] Salavagione H. J., Acevedo D. F., Miras M. C., Motheo A. J., and Barbero C. A. *J. Polym. Sci., Part A: Polym. Chem.*, 42:5587, 2004.

[194] Ohta T., Fujikawa T., and Kuroda H. *Chem. Phys. Lett.*, 32:369, 1975.

[195] Rennie E. E., Kempgens B., Koeppe H. M., Hergenhahn U., Feldhaus J., Itchkawitz B. S., Kilcoyne A. L. D., Kivimaeki A., Maier K., Piancastelli M., Polcik N., Ruedel M., and Bradshaw A. A. M. *J. Chem. Phys.*, 113:7362, 2000.

[196] Solomon J. L., Madix R. J., and J. Stoehr. *Surf. Sci.*, 255:12, 1991.

[197] Yamada K., Teshima K., Kobayashi N., and Hirohashi R. *J.Electroanal. Chem.*, 394:71, 1995.

[198] Gospodinova N. and Terlemezyan L. *Prog. Polym. Sci.*, 23:1443, 1998.

[199] Zuman P. and Shah B. *Chem. Rev.*, 94:1621, 1994.

[200] Prabhakaran K., Kobayashi K., and Ogino T. *Surf. Sci.*, 290:239, 1993.

[201] Hollinger G., Morar J. F., Himpsel F. J., Hughes G., and Jordan J. L. *Surf. Sci.*, 168:609, 1986.

[202] Namiki A., Tanimoto K., Nakamura T., Ohtake N., and Suzaki T. *Surf. Sci.*, 222:530, 1989.

[203] Batich C. D. and Donald D. S. *J. Am. Chem. Soc.*, 106:2758, 1984.

[204] Sakamoto K., Zhang H. M., and Uhrberg R. I. G. *Phys. Rev. B*, 70:35301–1, 2004.

[205] Teraoka Y. and Yoshigoe A. *Jpn. J. Appl. Phys.*, 41:4253, 2002.

[206] Hollinger G. and Himpsel F. J. *Appl. Phys. Lett.*, 44:93, 1984.

[207] Oh J. H., Yeom H. W., Hagimoto Y., One K., Oshima M., Harita N., Nywa M., Toriumi A., and Kakizaki A. *Phys. Rev. B*, 63:205310–1, 2001.

[208] Niwano M., Katakura H., Takeda Y., Takakuwa Y., Miyamoto N., Hiraiwa A., and Yagi K. *J. Vac. Sci. Technol., A*, 9:195, 1991.

[209] Palik E. D. *Handbook of optical constants of solids.* Academic Press, Inc., London, 1985.

[210] Tsankov D., Hinrichs K., Korte E. H., Dietel R., and Röseler A. *Langmuir*, 18:6559, 2002.

[211] Powell M. J. D. *Numerical Methods for Nonlinear Algebraic Equations*, chapter 7. Editor: Rabiniwitz P., (Routledge), 1970.

Acknowledgments

This work would not be possible without the input and support from many of my friends and colleagues. Especially I would like to express my gratitude to the following people:

Prof. Dr. N. Esser for the supervision of this work and for helpful discussions, and for the opportunity to work in the ISAS team.

Dr. K. Hinrichs for his guidance, support and for sharing his deep insight into the field of IR ellipsometry, for his humor and friendship.

Dr. J. Rappich for his introduction to electrochemistry, preparation of the samples, interesting discussions and collaborative work.

Dr. R. Hunger for XPS measurements and for enlightening conversations.

Dr. Th. Dittrich for helpful comments.

Dr. U. Schade for a collaborative work at the infrared beamline at BESSY II.

Dr. A. Röseler for useful discussions.

Prof. Dr. W. Richter for his useful comments in the course of this work.

Prof. Dr. A. Katzir for his support during my relocation to Germany and for his hospitality during my visits at Tel Aviv university.

Prof. Dr. Y. Shapira for his kind hospitality in the Tel Aviv University.

Dr. A. Merson for sample preparation.

Dr. M. Ortolani for his help with the bolometer cooling.

Dr. M. Gensch for his collaborative work, encouragement and friendship.

Mr. F. Yang for a collaborative work, many useful discussions and for the

corrections of this thesis.

Ms. B. Pollakowski for X–ray fluorescence measurements and for helpful discussions.

Ms. I. Fischer for her dedicated assistance in the laboratory and for her help with many set-ups.

Mr. C. Roland, for his help with the UHV system and with the cryostatic equipment.

Mr. G. Hinte, Mr. R. Sorge, Mr. R. Herzlieb and Mr. D. Kutz for their constructions in the workshop.

Mr. R. Tischendorf for his electronics and computer support.

Ms. S. Reichardt for her guidance and her support concerning the Minerva fellowship.

All other members of ISAS and the former group of Prof. Richter for the motivating atmosphere.

I am thankful to many of my colleagues and my friends - Dr. S. Chandola, Dr. Y. Mikhailova, Dr. S.D. Silaghi, Dr. J. Lee, Dr. Th. Deniozou, Dr. C. Cobet, Mr. C. Werner, Ms. M. Rakel, Ms. S. John Louis, Ms. D. M. Rosu, Mr. D. Aulich, Ms. R. Passmann and Ms. S. Wenmackers for their support.

I am also thankful to all my friends abroad, who kept in touch despite the distance.

My warmest thanks are to Udi Fuchs, for his comfort during hard days, for a supply of cake and cups of hot chocolate, for discussions of the simulations and for reminding me about all those forgotten π's in the integrals when my programs did not work as expected. I am also grateful to Udi's parents, for their care and support.

And of cause, I would like to say a huge Spasiba to my family - my parents and my sister Helena, for their phone calls, their understanding and encouragement.

This work was supported by Minerva fellowship.